ABSTRACT

AY, YASAR. Theoretical Study of a Spherical Plasma Focus. (Under the direction of Dr. John Gilligan and Dr. Mohamed Bourham.)

A theoretical model is developed for two concentric electrodes spherical plasma focus device in order to investigate the plasma sheath dynamics, radiative emission, and the ion properties. The work focuses on the model development of the plasma sheath dynamics and its validation, followed by studying of the radiation effects and the beam-ion properties in such unique geometry as a pulsed source for neutrons, soft and hard x-rays, and electron and ion beams.

Chapter 1 is an introduction on fusion systems including plasma focus. Chapter 2 is an extensive literature survey on plasma focus modeling and experiments including the various radiations and their mechanism. Chapter 3 details modeling and validation of the plasma sheath dynamics model with comparison between hydrogen, deuterium, tritium and deuterium-tritium mixture for the production of pulsed neutrons. Chapter 4 is a study of the radiative phase, in which neutron yield is investigated, as well as the predicted beam-ion properties. Chapter 5 summarizes and discusses the results. Chapter 6 provides concluding remarks and proposed future works.

The phases of the developed model are the rundown phase I, rundown phase II, the reflected phase and a radiative phase. The rundown phase I starts immediately after the completion of the gas breakdown and ends when the current sheath reaches the equator point of the spherical shape. Then immediately followed by rundown phase II to start and it ends when the shock front hits the axis, which is the beginning of the reflected shock phase. Reflected shock front moves towards the incoming current sheath and meets it which is both the end of the reflected shock phase and the begin-

ning of the radiative phase. After the reflected shock front and the current sheath meet, the current sheath continues to move radially inward by compressing the produced plasma column until it reaches the axis. Since the discharge current contains important information about the plasma dynamic, electrodynamics, thermodynamics, and radiations emitted from the plasma focus, the discharge current wave form has been used to validate the model. A good agreement has been achieved between theoretical calculation and the experimental measurement of a similar spherical plasma focus device. The snowplow model with the help of the shock wave equations coupled to the circuit equations is used to predict the plasma and shock wave parameters by using the momentum and magnetic force equations. While these equations are used in the phases of the rundown phase I and II, the reflected shock phase with the necessary modification of the magnetic field calculation, and the constant reflected shock front velocity; the radiative phase additionally includes the effect of the radiations emitted from the plasma column (Bremsstrahlung, line and radiative recombination), and the joule heating with the plasma resistance. Neutron yield and the ion properties are calculated in the radiative phase.

The parameters for the spherical plasma focus are 8.0 and 14.5 cm inner and outer electrode radii, respectively, 432 μF capacitor bank, 25 kV charging voltage, and 14.5 Torr DT gas pressure. A high discharge current of about 1.5 MA, a high neutron yield of 1.13 $\times 10^{13}$ neutrons, and a high plasma column-ion density of 1.61 $\times 10^{24}$ m^{-3} are achieved with the given parameters. The developed model is also used to investigate the effect of the gas pressure, discharge voltage, and the molecular mass of the gas on the maximum plasma temperature and pinch start time. It is found that the maximum plasma temperature can be obtained with a relatively shorter pinch start time using a relatively heavier gas with lower gas pressure and higher discharge voltage.

© Copyright 2015 by Yasar Ay

All Rights Reserved

Theoretical Study of a Spherical Plasma Focus

by
Yasar Ay

A dissertation submitted to the Graduate Faculty of
North Carolina State University
in partial fulfillment of the
requirements for the Degree of
Doctor of Philosophy

Nuclear Engineering

Raleigh, North Carolina

2015

APPROVED BY:

Dr. Alexei Saveliev	Dr. Igor Bolotnov
Dr. John Gilligan Co-chair of Advisory Committee	Dr. Mohamed Bourham Co-chair of Advisory Committee

DEDICATION

TO MY BEST FRIEND

TO MY LOVING GORGEOUS WIFE

TO MY EVERYTHING

TO ILHAM YILMAZ AY

ACKNOWLEDGEMENTS

I am so grateful to have unconditional support, help, understanding, and especially love of my family. Even if they live in Turkey, I always feel their love and support with me. I want to thank my father Mehmet, my mother Fatma, my sisters Hanime and Dilan, and my brothers Ferit, Yusuf, and Yunus. They have been my only heroes all the time and they will be. I cannot live without their love. Thank you very much my amazing family. I am so glad that I have you in my life.

I would like to thank the best person I have ever met, my advisor Dr. Mohamed Bourham, for his all help, guidance and support during my PhD career. He not only shared his experience with me for better academic career but also treated me as a family member. Having a family member for a foreign student is priceless. I am so lucky to have Dr. Bourham as both my advisor and my big brother. Whenever I have a problem or question, he was there. The things that I learned from Dr. Bourham are invaluable. Thank you very much Dr. Bourham for your patience, understanding, support, guidance, and all the help and effort.

I want to thank Dr. Abd Al-Halim as well. Even though he lives in Egypt, he helped me all the time for finishing my work. He answered all my questions patiently and spent a lot of time with me for help. I wish his family and him all the best.

I also would like to thank my committee members, Dr. John Gilligan, Dr. Igor Bolotnov, and Dr. Alexei Saveliev for their helpful and informative feedback, questions and comments. Thank you very much for being in my committee.

TABLE OF CONTENTS

LIST OF FIGURES

CHAPTER

1

INTRODUCTION

Large energy production and consumption are the main part of modern life. Many energy sources have been investigated so far. Coal, petroleum and natural gas as fossil fuels, solar energy, hydroelectric power and wind power as renewable energy sources, and nuclear fission fuels are some examples of the energy sources from which fossil fuels, which have limited supply and carbon dioxide emission to atmosphere, and nuclear fission fuels, which have associated radioactive waste disposal, safety and proliferation issues, are today's two major energy sources.

Even though renewable energy sources are growing quickly, they are low energy density sources. They are not suitable for modern life urban industrial complexes. Therefore, energy production with fusion reactions would be necessary for a long-term clean energy sources.

Fusion researches aim to fuse light atomic nuclei to generate energy from this reaction. In order to produce fusion energy, two fusionable nuclei should be enough energetic to overcome their electrostatic repulsion so that the nuclei come close enough to each other, and short-range attractive nuclear forces fuse the nuclei to form a compound nucleus which eventually breaks up into lighter and more energetic reaction products [Rot86].

For fusion reactor fuels, hydrogen (H), deuterium (D), tritium (T), helium (^{3}He), lithium (^{6}Li), and boron (^{11}B) are the possible nuclei from which DT reaction has more potential as fusion fuel due to its large cross section and higher reaction rates even if it has some disadvantages such as the shortage of tritium and 14.1 MeV neutrons from fusion reaction which can cause radiation damage and radioactivity of materials. The nuclear reactions of interest for fusion reactions are as follows [Dol82] :

$$D \quad + \quad T \quad \rightarrow \quad {}^{4}_{2}He \ (3.52\text{MeV}) \quad + \quad {}^{1}_{0}n \ (14.1\text{MeV}) \tag{1.1}$$

$$D \quad + \quad D \quad \rightarrow \quad {}^{3}_{2}He \ (0.82\text{MeV}) \quad + \quad {}^{1}_{0}n \ (2.45\text{MeV}) \tag{1.2}$$

$$D \quad + \quad D \quad \rightarrow \quad T \ (1.01\text{MeV}) \quad + \quad p \ (3.02\text{MeV}) \tag{1.3}$$

$$D \quad + \quad {}^{3}_{2}He \quad \rightarrow \quad {}^{4}_{2}He \ (3.66\text{MeV}) \quad + \quad p \ (14.6\text{MeV}) \tag{1.4}$$

$$T \quad + \quad T \quad \rightarrow \quad {}^{1}_{0}n \quad + \quad {}^{1}_{0}n \quad + \quad {}^{4}_{2}He \tag{1.5}$$

$$p \quad + \quad {}^{6}_{3}Li \quad \rightarrow \quad {}^{4}_{2}He \quad + \quad {}^{3}_{2}He \tag{1.6}$$

$$p \quad + \quad {}^{11}_{5}B \quad \rightarrow \quad 3({}^{4}_{2}He) \tag{1.7}$$

In order to produce energy from fusion reactions, it is needed to heat the fusion fuel to ignition temperature so that positively charged particles approach sufficiently to each other over the Coulomb field and with a high relative velocities for a nuclear reaction to occur, and we also need to confine it while the fuel burns to maintain the plasma pressure and to provide a long energy confinement time so that we can have a high energy-gain ratio.

For hot fusion, inertial and magnetic confinement are the two ways to overcome the Coulomb barrier from the physical point of view. Hot fusion will be the main interest of discussion here. While the mostly investigated confinement categories are magnetic confinement, which provides thermal isolation between the plasma and the chamber wall by using a strong magnetic field; and inertial confinement, which depends on an extremely high density plasma, other confinement schemes such as the tandem mirrors, the field reversed pinch, ohmically-heated toroidal experiment, stellarators, and compact torus are also studied for fusion energy investigations [Dol82].

Plasma cannot be confined with a container due to its high temperature which causes any structural material to melt. Therefore, magnetic confinement and inertial confinement are considered as two main approaches for confining plasma.

1.1 Magnetic Confinement

Magnetic confinement uses the magnetic field effect on charged particles to confine the plasma. Since the plasma consists of charged particles which can only gyrate around the field lines of the magnetic field due to the Lorentz force, if neglecting small transverse motion, magnetic confinement uses this natural features to confine the plasma particles by forcing orbital motion as well as imposing a magnetic field pressure on the plasma, which is configuring the magnetic field in devices such as tokamaks and stellarators [AV04].

In a uniform magnetic field while positive particles gyrate in one direction of the field lines, the negative particles gyrate in the opposite direction of the field lines but none of them crosses the field lines if there are no collisions so that the hot plasma can be confined in a strong magnetic field [GL60].

Plasma amplification factor Q is an important design parameter that should be taken into account for the fusion reactor design.

$$Q = \frac{P_{thermo}}{P_{input}} \tag{1.8}$$

where P_{thermo} is the generated thermonuclear power, and P_{input} is the power input to produce and heat the plasma to thermonuclear fusion temperatures [Rag06].

On one hand, when the energy of the ions which are released from the fusion reactions exceed the radiative and other energy losses, plasma ignition occurs, and large Q values are possible in a closed configuration system where magnetic field lines

stay in the plasma region and do not intersect the wall such as a toroidal device. On the other hand, it is unlikely to have plasma ignition in an open configuration system where magnetic field lines leave the plasma region such as a mirror fusion reactor due to the end losses.

In an ignited plasma, while a considerable amount of particles collide with each other frequently, the magnetic field must confine them so that the energy transfer from the particles with thermal energy to the plasma container is not too fast. Therefore, there are some necessary conditions on the density, temperature, and thermal insulation of the plasma to be met to ignite the fusion reactions. For example, an absolute plasma temperature and energy confinement time should be at least $10^8 K$ and with the plasma density of about 10^{14} particles per $c\,m^3$.

There should be an energy input which should both ignite the plasma and compensate for the radiation losses from the plasma. The energy produced from the plasma should be greater than both the energy input and radiation losses so that energy breakeven condition is met which is expressed by the Lawson parameter as follows [Rag06] :

$$n\tau_\epsilon \geq 2.0 \times 10^{14} \quad [\frac{\text{particles} \times \text{sec}}{\text{cm}^3}] \tag{1.9}$$

where n is the plasma density, and τ_ϵ is the energy confinement time.

1.2 Inertial Confinement

In contrast to magnetic confinement, inertial confinement does not use external confinement means. Mass inertia is the key point for inertial confinement. Assume that there is an assembled spherical fusion plasma volume which is kept together with mass inertia for a short period of time which is the confinement time for fusion to occur for inertial confinement [AV04]. The general principle for inertial confinement is the same, with much smaller quantity of frozen fuel in the form of a capsule, to be compressed and heated so quickly to achieve fusion conditions while the inertia of the fuel keeps it from escaping [MS12].

Since the confinement time is very short, it is necessary to have a high density plasma, which can be achieved by compressing the fuel, to burn considerable amount of the fusion fuel with high reaction rates [AV04]. Inertial confinement fusion occurs in nature. Stars are made of hydrogen which is compressed by their gravitational forces to increase the density and temperature to start thermonuclear reactions but on earth gravitational attraction forces are too low for the same purpose [Bob14]. Therefore, short energetic laser or ion beam pulses are considered as methods to satisfy inertial confinement conditions to heat and compress small fuel capsules.

The small target pellet with the size of several millimeter in diameter is launched into the inertial confinement fusion reactor chamber, and it is compressed and ignited using laser beams or ion beams while it is going through the center of the chamber, which results in a small thermonuclear explosion producing heat which is deposited in the chamber walls.

The idea of inertial confinement fusion reactor has some important features such as "energy focusing" in that a considerable amount of energy (1-10 MJ) must be focused onto a small target pellet in a short period of time ($\sim$ 10 ns), "target compression" in that order to produce high energy gains, final fuel density should be 1000 $g/c\,m^3$, and "burn wave" which are explained below.

When the laser or ion beams hit the target surface, a plasma is formed around the target by ionizing the surface atoms. This plasma both reflects some of this beam energy and absorbs the other part of the beam energy. This causes heat conduction to the target surface resulting in continuing ablation (erosion) from the surface which produce a reactive force to compress the pellet shell inwards, compressing the target to high density. This compression may result in an ignition of fuel at the pellet center by spherical shock waves which produce an outwards propagating thermonuclear burn wave provided that there is a high enough plasma density [Dol82].

In order to study fusion with both inertial confinement and magnetic confinement, the setup of the experiments are quite expensive, and there are many technical and mechanical challenges. The space needed to build the experiment is another point that should be taken into account when building fusion experiment by using inertial or magnetic confinement. Compared to inertial and magnetic confinements, the plasma focus devices are cheaper to build, simple to operate, and have compact design to study the fusion energy. They also require less space for experimental setup.

1.3 Plasma Focus Device

The plasma Focus (PF) devices are high-voltage high-current pulsed electrical discharges in gases that were independently developed by Filippov [Fil62] in the Soviet Union and Mather [Mat64; Mat65] in the United States with the different electrode configurations in the cylindrical geometry.

The PF devices are used to produce hot and dense plasma sources through an electric discharge occurring across the surface of the insulator when the pulse power system discharges, followed by an axially symmetric umbrella-like current sheath (CS) formation, then followed by reaching the symmetry axis of the chamber at the maximum current by choosing the appropriate dimensions of the electrodes and the filling gas pressure. The device with the filling of specific gas/gases provides various applications such as x-ray production [Zak96; Zak97], neutron production [Zak96; LS08a; LS08b; Lee08; SL98; SL99; Koh05a], nuclear fusion reactions with neutrons and protons when the fill gas is deuterium [PM03; Zae10; Kne06; Ber98]. It can also be used for the production of powerful beams of electrons and ions due to microinstabilities and turbulence, which occur near the anode in a small volume on the axis where the energy stored around the current sheath (CS) as kinetic and magnetic energy during the motion of the sheath is converted into beams energy with a large power increase [Ber98].

In general, the plasma focus dynamics for pinch (hot and dense plasma) formation consists of 3 different phases. These are breakdown phase (inverse pinch phase), acceleration phase (run down phase), and radial phase which are illustrated in figure

1.1 for axial and radial phases. While figure 1.1a shows the axial phase, the step by step development of the radial phase can be seen in figures 1.1b, 1.1c, and 1.1d.

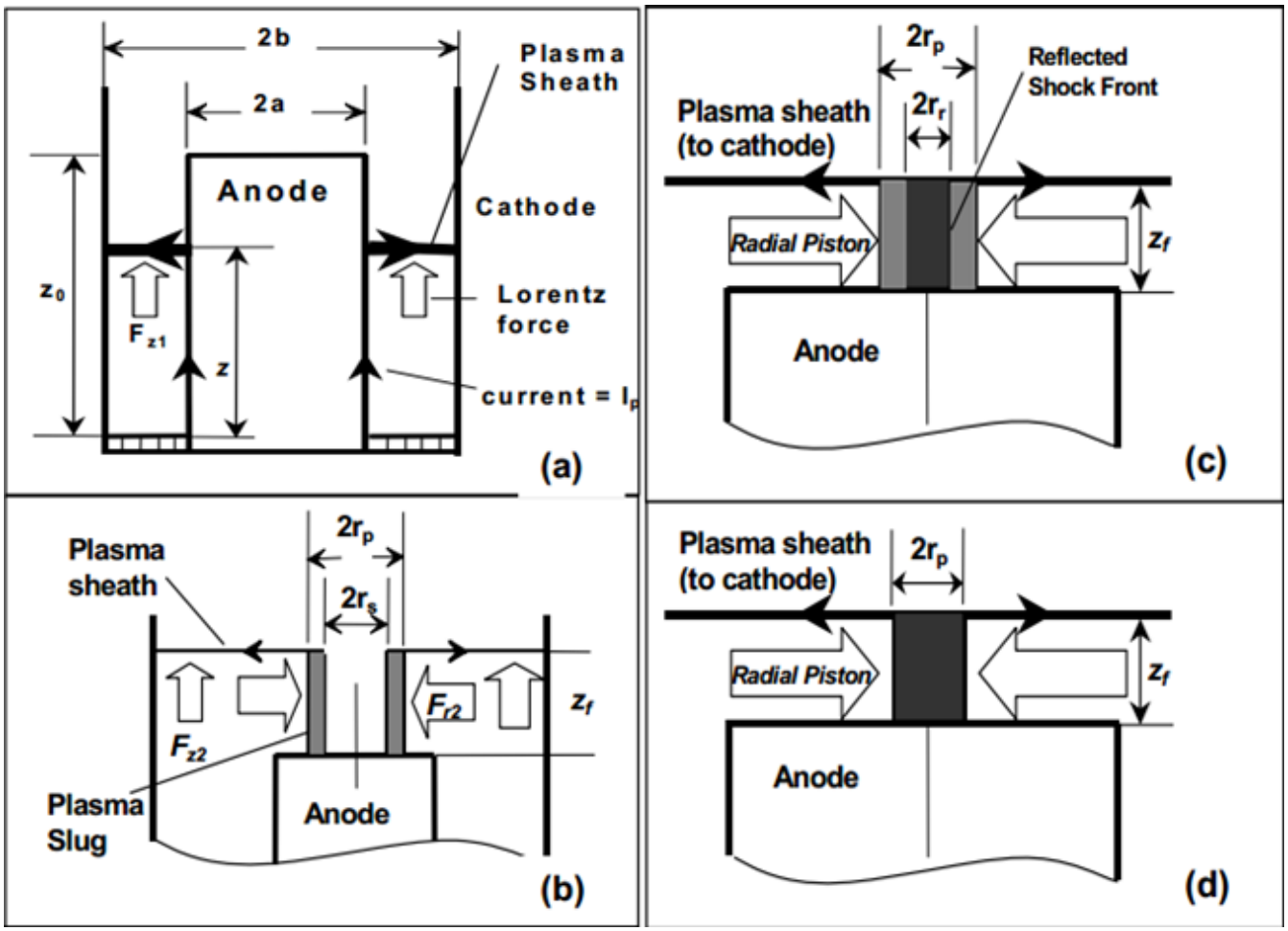

Figure 1.1 Dynamics of the plasma focus for pinch formation for axial and radial phases [Raf00]

1.3.1 Breakdown phase

In a plasma focus vacuum chamber filled with a working gas at an adequate pressure, there will be free electrons between the inner electrode (anode) and the outer electrode (cathode) upon discharging the voltage from the power system. The high voltage discharge results in generation of azimuthal electric field between the electrodes that accelerates these free electrons. These accelerated electrons start ionization processes including multiple avalanches and eventually increases the charged particle population leading to electrical gas breakdown. The ionized gas in the plasma focus device turns into a plasma sheath near the insulator surface. Plasma sheath with low resistance in this phase provides a path for the discharge current to flow from anode to cathode across the insulator surface when breakdown is completed. Both sliding discharge along the insulator and filamentary radial discharge are generated in this phase depending on the gas pressure. In addition to the gas pressure, insulator dimension and material with electrodes configuration also have effect on the formation of the uniform current sheath in breakdown phase [Ver10a].

1.3.2 Axial Phase

Axial phase begins when the current sheath in the breakdown phase reaches the inner surface of the outer electrode (figure 1.1a). It is then accelerated by the $J \times B$ Lorentz force along the Z-axis towards the open end of the electrodes.

The Lorentz force accelerating the current sheath axially has $1/r$ dependency where r is the distance from the inner electrode (anode). Therefore, the force accel-

erating the current sheath is not the same across the whole current sheath. While it is stronger near the inner electrode, which leads to a higher velocity of the current sheath in this region, it is weaker close to the outer electrode which gives rise to a lower current sheath velocity near the outer electrode. Therefore, as the current sheath moves towards the open end of the electrode, it gets more curved until the current sheath reaches the open end of the inner electrode.

The current sheath collects all the gases in front of it with some mass efficiency factor and leaves a vacuum region behind it, which is called magnetic piston. Since the current sheath has supersonic speed, this fast moving sheath generates a shock wave (called shock front) which is driven by the magnetic piston. The shock wave and magnetic piston contain a plasma layer in between. The shock wave ionizes, heats, and compresses the neutral gas in front of it.

This phase ends when the current sheath reaches the open end of the inner electrode and then sweeps around the end of the inner electrode, which is the starting point for the radial phase.

1.3.3 Radial Phase

As mentioned above, radial phase starts when the current sheath sweeps around the inner electrode and moves radially inward towards the axis. Figures 1.1b, 1.1c, and 1.1d illustrate the development of the pinch step by step in the radial phase.

This phase is important not only for a rapid inductance change which give rise to an induced electric field in the plasma column but also for high energy density, multiple radiation emissions, high energy particles, and nuclear fusion products when

deuterium or deuterium-tritium gas mixture is used as a working gas [Ver10a].

In this phase, while the current sheath moves towards the axis, the shock front hits the axis and reflects back towards the current sheath with the shock heating as the main heating mechanism in the plasma until the reflected shock front meets the current sheath. After this point, the plasma column is formed, and the current sheath continues to move towards the axis until the current sheaths hit each other on the axis with the joule heating as the main heating mechanism in the plasma, which can be seen in figures 1.1b, 1.1c, and 1.1d sequentially as well.

The fast penetration of the magnetic field into the plasma column, which is compressed further adiabatically, gives rise to an anomalous high plasma resistance (anomalous resistivity effect) and an increase in the rate of change of the plasma inductance which eventually lead to a sharp voltage spike and a dip in the discharge current. The sharp voltage spike and the dip in the discharge current as in the figure 1.2 are general features of the plasma focus devices.

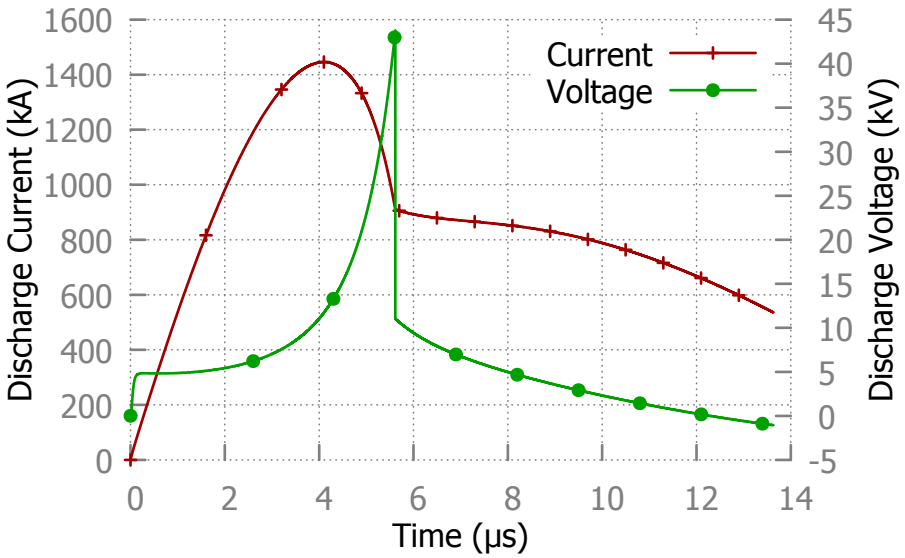

Figure 1.2 Plasma Discharge Current and Voltage

The increase in the plasma inductance generates an electric field in the plasma column which accelerates the electrons towards the anode and ions in the opposite direction. The interaction of electrons and ions with the anode and the plasma column results in nuclear fusion products, fast energetic ions and electrons, soft and hard x-ray emissions from the plasma focus device in the radial phase [Raf00].

There is an increase in investigation of the plasma focus devices due to high efficiency x-ray production, emission of high energy electrons and ions in addition to the copious neutron production in the plasma focus devices. Even though the plasma focus devices have attracted many researchers, the physics behind the most of the phenomena occurring in the dense plasma focus devices are not well understood yet.

CHAPTER

2

PLASMA FOCUS MODELING AND RADIATION EMISSIONS

Since plasma focus devices are compact, cost-effective, and efficient source of radiations with high $n\tau_\epsilon$ value, they are explored for different purposes and applications. Various theoretical and computational models have been developed to understand the phenomena occurring in the device, and many experiments have been conducted to investigate the radiation emissions from the plasma focus devices with their possible

applications.

While the experiments conducted with the plasma focus devices have a wide range of stored energy from sub-kilo joule to mega joule devices, the considered models tried to explain the phenomena occurring in the plasma focus devices and have also a wide range of model varieties such as snow plow model, quasi steady-state model, slug model, gas dynamic model, ion beam acceleration and neutron production models, moving boiler model, beam target models including gyrating particle model and cross field acceleration model, plasma diode model, double-layer pulse current model, surfing model, and collective focusing model [Tal12].

Even though neutron production from the fusion reactions with the working gas of deuterium or deuterium-tritium mixture is the main study area of the plasma focus devices in the beginning of its researches, soft and hard x-ray emissions, high energy electrons and ions have been attracting the attention of the scientific community for the possible applications of plasma focus devices.

2.1 Plasma Focus Modeling

Since the generally used Plasma Focus (PF) geometries are Mather type and Filippov type plasma focus devices, the developed models simulate these two types of plasma focus devices. In order to validate the developed model, experimentally measured discharge current is generally fitted with the calculated discharge current from the model. After fitting the currents, the plasma focus models can predict the plasma and shock parameters.

Several models were developed for both Mather type [Lee83; S. 85; Lee85a; Lee85c; Lee85b; M. 07; Gon04; Gon09; Mat97] and Flippov type [MT07; Sia05; Gou08] plasma focus devices. The most used and known model for the Mather type PF is Lee's snowplow in the axial phase and the Potter's slug model [Pot71; Pot78] in the radial phases due to the zero final radius of the snowplow model in the radial phases and coupled them with the plasma circuit equations.

In addition to the plasma focus dynamics, Lee's model successfully simulates various important parameters such as the energy transfer process in the PF [Sha00], and dimension and lifetime of the pinch [LS96; Lee83]. In Lee's model, the electric current that passes through the plasma sheath is considered as a fraction of the total discharge current, which is represented as the current fraction factor in Lee's model.

A model was also developed for PF with hemispherical electrodes [M. 10]. In this model, snowplow model, the momentum, plasma circuit and shock wave equations were used.

In this hemispherical model, the motion starts at the equator and ends at the

antipodal point of the hemisphere. The governing equations of this model is equation of motion, which consists of the momentum and magnetic pressure equation to calculate the plasma sheath velocity and position. It also includes the circuit equation, which is used to calculate the plasma inductance and discharge voltage. In order to calculate the plasma temperature and shock wave velocity with its position, the shock wave equation is used.

In this study, the comparison between hemispherical electrodes and cylindrical electrodes were investigated. A good match of discharge current between hemispherical and cylindrical electrodes were obtained for validation.

The deep dip current and sharp spike voltage represent the evidence of better focusing formations [AH10; Mur11; Ver10b]. Hemispherical electrodes has a dipper discharge current dip with the higher discharge voltage spike, which shows better focus action for hemispherical electrodes plasma focus device compared to cylindrical electrodes one. Better focus represents optimum conditions for the radiation emissions in the case of the plasma focus devices, such as x-ray production [Kha10; Hab10] or neutron production [Nir11; Kri12].

For the Mather type PF, the Masoud model [M. 07] has introduced an angle into the snow plow model, slug model, and plasma circuit equations in order to improve the continuity between the axial and radial phases for the calculation of the plasma parameters.

The open-cathode PF model, which is the PF without surrounding cathode, was developed to predict the neutron production and pinch voltage of the PF [Gon04; Gon09]. This model was based on the snowplow model with the radial expansion of

the current sheath in addition to the included pinch model. Fogliatto et all expanded this model by introducing runaway electron model and hard x-ray production. The correlation of the radiation intensity with the charging voltage was also predicted by using the open-cathode plasma focus model [Fog14].

The three-phase theory model has allowed the CS to have both radial and axial variation during the rundown phase [Mat97]. This model also accounts the breakdown of the gas. Three-phase theory model was used to predict the design parameters, such as the inner and outer electrode radii, and the inner electrode length in addition to the gas pressure and charging voltage for optimum focus action in the plasma focus device.

For the Filippov type PF, while Siahpoush et al. has adapted the Lee model with the slug model for Filippov type PF [Sia05], Goudarzi et al. has used the lumped parameter model with the mass and momentum equations coupled with the equivalent circuit equations [Gou08].

The kinetic particle-in-cell simulations are capable of modeling the mega joule plasma focus devices. The kinetic instabilities from the ion beam formation and neutron production [Lin14] were predicted in addition to the current sheath instabilities [Cas14] by using the developed simulations. The effect of the anode shapes on neutron yield, neutron anisotropy, and ion beam production were also studied with the developed kinetic particle-in-cell simulation [Lin14].

Schmidt et al. developed a fully kinetic simulation of dense plasma focus to simulate the pinch process at the particle scale for kilo-joule-scale [Sch12a; Sch14a] and mega-joule-scale [Sch14b] dense plasma focus devices. They compared their kinetic

model with fluid and hybrid (kinetic ions and fluid electrons) models [Sch12a] as well as the experimental results [Sch14a].

In this comparison, as far as the experimentally observed high energy ion beams and neutron yields are concerned, the fully kinetic simulation predicted high energy ions and experimental neutron yields but fluid simulation, which did not give neutron yields and did not allow for non-thermal ions, and hybrid simulation, which underestimated neutron yield, were not as successful as fully kinetic simulation. For the mega-joule-scale dense plasma focus device, the model predicted ion and neutron spectra, neutron anisotropy, and the total neutron yield in agreement with experimental results.

The fully kinetic particle-in-cell model was developed by Welch et al. This model can simulate the complete time evolution of a Z-pinch [Wel09] and provide information for neutron production mechanisms with multidimensional (1D-3D) simulations [Wel11]. This model also showed that higher neutron yields could be achievable with higher pinch current.

Sears et al. used particle-in-cell simulation, which had fluid model for the rundown phase and fully kinetic model for the pinch phase, in order to explore the driver impedance effect on the neutron yield. The particle in cell simulation was also used to investigate the kinetic instabilities, anomalous resistivity, and beam formation during the pinch phase [Sea14].

Another particle-in-cell code includes the magnetic effect to simulate the breakdown and initial lift off phase of the plasma focus device in order to study the optimum conditions and breakdown process in the plasma focus device. The electromagnetic

particle-in-cell code coupled with the external circuit indicated that the electron energy density function was non-Maxwellian [Sen15; Sen14].

A full dissipative set of non-ideal MHD equation and Braginski transport with the assumption of partially ionized plasma were used for a model in a computational study. This model is based on the modified free points methods, and it accounts for ionization kinetics as well in addition to the anomalous resistivity in the low density region due to the plasma turbulence [Ste04].

The MHD model developed by Garanin and Mamyshev took into account the vacuum region behind the plasma current sheath so that the focusing process and the acceleration mechanisms could be described appropriately in order to simulate the fast ions and fusion neutron productions from the plasma focus device [GM08].

The combination of MHD and kinetic model can be useful to understand the neutron production mechanism and to investigate the effect of the anode shapes on the structure of the imploding plasma and instabilities in the deuterium dense plasma focus device [AC14].

Pestehe et al. studied the signals from a dynamic Faraday cup by developing a model which was used to simulate the output signal of the Faraday cup with the help of the calculated induced surface charge for both single-pulse and the multi-pulse modes [Pes14].

A computational study was conducted in order to study the radiation emission spectrum from a neon plasma focus device by assuming a non-local thermodynamic equilibrium model for the plasma. The electron temperature ranges for both neon plasma soft x-ray emission and extreme ultraviolet emission were also explored in

this computational study [Ake13b].

Monte Carlo method is a useful tool for plasma focus studies. Roomi et al. used Monte Carlo method so that they could reconstruct the time dependent energy spectra of neutrons from D-D reactions in a plasma focus device by using deuterium filling gas. They also used it to find the position of the necessary detectors (distance between the neutron source and detectors) for reconstruction of signal in the experiment [Roo11a].

The computational study developed by Miklaszewski was based on Gyrating Particle Model in order to describe the neutron emission from the plasma focus device. It was found that while trapping of the high energy deuterons in the pinch region was responsible for the neutron yield increase with increasing pinch current, the deuteron drift towards the anode was the cause of the decrease in the neutron yield above a certain pinch current level [Mik04].

2.2 X-rays

The energy loss through electromagnetic radiation, which is the source of the radiation, has significant effect on the energy balance of the plasma. The main interest of source of the electromagnetic radiation emitted from the plasma are due to the transitions of bound or free states of atoms or ions [Gri64].

There are two main type of processes that result in x-ray production. The first type is the charged particle acceleration/deceleration (usually electrons). Bremsstrahlung radiation, which is the deceleration of electrons by collisions with heavy nuclei, is an example of the first type which gives a continuous spectra. The change of an atomic or ionic energy level of electron to a lower level is the second type which gives a discrete line spectra. In order to have the second type of process, either electrons should bombard a low atomic number target or a plasma should be produced from a low atomic number material [MB93].

When the plasma is not fully ionized, an ion in the plasma can absorb energy and be raised to an excited state by colliding with a free electron, and the energy emission will be in the form of excitation radiation when the electron returns to a lower state.

Hydrogen isotopes contain only a single electron that can be completely stripped at a temperature of about 0.05 keV above which the excitation radiation will not occur unless there is impurities from higher atomic number species which cause significant energy losses in the form of excitation radiation. Without considering impurities, a fully ionized plasma contains equal amount of completely stripped nuclei of hydrogen isotopes and electrons. The main energy loss mechanism in such a plasma is in the

form of continuous radiation of bremsstrahlung which is emitted by charged particles (usually electrons) as a result of deflection in the Coulomb fields of other charged particles (free-free transitions) [GL60].

When an electron collides with the solid target (an anode) or a positively charged particle (an ion), there are two possible forms of radiations from this collision depending on the final state of the electron. It causes either a continuous spectrum or a line spectrum. The final state of the electron can be either free, which results in free-free transition (bremsstrahlung radiation), or bound, which gives free-bound transition (recombination radiation) in which the electron is captured by the ion into a bound final state [Hut87].

Bremsstrahlung radiation, which occurs when the incident electrons decelerate due to the coulomb interaction with the electrons and the nuclei of the target material or ions, and recombination radiation, which results from the recombination of an initially free electron with an ion while electron loses energy, are the two mechanisms that give continuum emission. A bound electron can lose energy by falling to a lower ionic energy state which gives the line radiation [MB93].

As the line spectrum, an inner-level atomic electron is removed, and then the relaxation of the atom results in x-ray emission which is characterized mostly by the target material [MB93]. When a vacancy in an inner atomic energy level is created by the electron impact, this vacancy is filled from a higher energy level electron loosing energy by radiation of a photon, which results in x-ray line spectra [MB93]. The continuum radiation for a plasma formed from a high-Z material or the line radiation for a plasma formed from a low-Z material can be stronger which depends

on how the plasma is formed [MB93].

As mentioned above, there are 3 mechanisms that give either continuous radiation or line radiations. These are free-free transition (Bremsstrahlung radiation), free-bound transition (recombination radiation), and bound-bound transition (line radiation).

2.2.1 Free-Free Transition (Bremsstrahlung Radiation)

An electron can make a transition from a higher energy free state to a lower energy free state by colliding with another particle (usually ions) which causes electron to decelerate and loose energy from which some is used to excite the ion, and the excess energy is emitted as free-free radiation (Bremsstrahlung) with a continuum spectrum [MB93].

Even if the plasma is fully ionized and containing only stripped ions, there will be transitions of free states of electrons moving in the Coulomb fields of the ions which generate radiation. Due to this transition, the electron looses the kinetic energy which is the energy of the emitted photon [Gri64].

2.2.2 Free-Bound Transition (Recombination Radiation)

An ion can capture a free electron to a bound state and reduce the ionic charge of the ion by one, which gives an emission of photon originated from the excess energy of the electron, which also gives a continuum emission spectrum for each bound state (free-bound or recombination radiation) [MB93].

2.2.3 Bound-Bound Transition (Line Radiation)

A bound electron, which is excited to a higher energy state by collisions with other particles (primarily electrons), makes a transition from a higher bound state energy to a lower bound state energy of the ion which results in the emission of well-defined energy photon (line spectrum) which depends on the electron temperature and density.

Increasing the electron temperature will result in more energetic state of ions which gives the emission of shorter wavelength radiation. The plasma will be completely ionized at temperature greater than 100 eV for low-Z materials and several keV for high-Z materials, that is the bound-bound radiations no longer occur for a completely ionized plasma [MB93].

In general, if there are atomic species which have the excitation energies of the order of kT_e, the total amount of line radiation, which is related to Z_i^6, will be higher than the free-free radiation, which is proportional to Z_i^2 and free-bound radiation, which is approximately proportional to Z_i^4 [HL65].

Plasma focus device are a good, efficient, and inexpensive source of x-rays. Therefore, x-ray production from the plasma focus devices and its applications are attractive research areas for the scientific community. Experiments aimed to explore the plasma focus x-ray production with its aspects as mentioned in the rest of this section.

The effect of the pre-ionization due to an α source from depleted uranium ($_{92}U^{238}$) on x-ray emission of the plasma focus device was investigated [Kha10; Ahm14]. Pre-ionization leads to a significant increase in $Cu-K_\alpha$ emission (about 30%) as well as the total x-ray yield compared to the results obtained without pre-ionization. It also increases the estimated average efficiency of the system for $Cu-K_\alpha$ emission from

0.08% without pre-ionization to 0.12% with pre-ionization [Ahm14]. In addition to the increase in soft x-ray emission (about 60%) and the total x-ray yield (about 44%), pre-ionization also increases the focus duration and shot-to-shot reproducibility of the plasma focus [Kha10].

The effect of pre-ionization due to β source from ${}_{28}N^{63}$ around the insulator sleeve on the x-ray emission was also investigated in a (2.3-3.9 kJ) plasma focus device for argon and hydrogen filling gases at different charging voltages and gas pressures. Pre-ionization enhances the x-ray emission around 25% for argon and around 17% for hydrogen as well as the shot-to-shot reproducibility. It was also found that the major x-ray emission was from the anode due to the electrons hitting the anode tip. The emission of x-ray with Pb insert at the anode tip showed that the charging voltage more than optimum value gave rise to degradation of x-ray yield from the plasma focus device [Ahm06a].

The type of the metal insert has a strong effect on x-ray emission from the plasma focus device. This effect was observed for copper anode with molybdenum, tungsten, and lead inserts at the anode tip from a low energy (1.4-5.3 kJ) plasma focus device. In this experiment, copper showed the highest x-ray yield (67.6 J) and highest x-ray efficiency (1.5%) for x-ray production at the optimum gas pressure [Hus06]. The scaling law for x-ray emission was also obtained [Sha06].

The multi-radiation of x-rays due to the anomalous resistivity was investigated in a low energy (up to 4.9 kJ) plasma focus device with argon filling gas. The observed energy of x-rays of $Cu-K_\alpha$ and $Cu-K_\beta$ were around (0.14 ± 0.02) and (0.04 ± 0.01) J/Sr, respectively, in addition to hard x-ray energy of (0.12 ± 0.02) J/Sr [AB14].

Two neon soft x-ray peaks were observed from a 3.3 kJ plasma focus [Moh07a]. Two x-ray emission periods corresponding to two successive compressions in the pinched plasma were also detected from a 3 kJ plasma focus device with hydrogen filling gas and argon admixture. These x-ray emissions were due to the electron beam hitting the anode and dense plasma column [Fav92]. It was found that there was an inverse correlation between the time difference of the peaks and the soft x-ray yield, i.e. small time difference between two peaks gives rise to high soft x-ray yield [Moh07a].

The effect of doping on soft x-ray (900-1600 eV) and hard x-ray (>1600 eV) was investigated from a 235 J plasma focus device with neon filling gas. Krypton was used as doping gas. it was found that while the 1% krypton doping resulted in better soft x-ray emission efficiency (about 30%) at optimum gas pressure, it did not effect the hard x-ray emission [Kal14a]. It was also found that krypton seeding enhanced the x-ray yield from 10-fold to 17-fold at low pressures ($\leq$ 0.4 mbar) for a miniature plasma focus device (200 J) with deuterium filling gas [Ver08].

It was also found that insulator length, insulator material, and filling gas pressure had a strong correlation with the soft and hard x-ray production [Kal14b; Hab13; Koo13]. Habibi investigated the correlation of insulator thickness and length with hard x-ray intensity in a 4.5 kJ plasma focus device with neon filling gas [Hab12b].

For studying the insulator material, Pyrex and quartz insulators were investigated resulting in higher hard x-ray intensity in Pyrex insulator at the optimum insulator length which was an important factor to obtain the maximum intensity of hard x-ray. While the insulator length smaller than the optimum length leads to a faster electrical breakdown of the gas which causes the current sheath to arrive the end of

the anode earlier than the rise time of the discharge current, the insulator length larger than optimum length leads to contamination of the current sheath from the ablated insulator material due to the heating of the insulator surface before the current sheath lifts off [Hab12a].

The shape and material of the anode tip have also considerable effect on x-ray emission from a plasma focus device [Hab10; Sha03]. Different shapes of anode tips such as flat and conic anode tips, and different anode materials such as copper, aluminum, and tungsten were considered. It was found that while conic tungsten tip gave rise to the highest hard x-ray intensity, flat aluminum tip resulted in the lowest hard x-ray intensity. It was also found that appropriate shape of the anode tip would lead to more isotropic hard x-ray emission from the plasma focus device [Hab10]. Another finding is that soft x-ray emission could be increased by 505% by using conical anode compared to the cylindrical anode [Hay13].

Baharani et al. studied the effect of the different anode shapes on angular distribution of x-rays in a 4 kJ plasma focus device with nitrogen filling gas [Bah14]. The anode shapes were cylindrical flat-end anode, cylindrical hollow-end anode, tapered flat-end anode, and tapered hollow-end anode from which the tapered flat-end anode shape gave high intensity x-ray compared to other anode shapes, which indicated that x-ray yield could be enhanced by using appropriate anode shape with optimum gas pressure and discharge voltage in a plasma focus device [Bah14; Kal13; Tal13; Bag11a].

Mohammadi et al. considered different anode shapes to study their effect on neon soft x-ray emission from the plasma focus device as well. Flat, tapered and hemispherical anode shapes were studied. While the flat anode resulted in the highest

neon soft x-ray yield, the hemispherical anode had the maximum hard x-ray yield. The hemispherical anode had multiple hard x-ray burst due to the multiple-pinch phenomena which gave rise to the maximum hard x-ray yield. The decrease in the focus plasma column length due to small radii of the tapered and hemispherical anodes caused a decrease in soft x-ray yield for these anodes [Moh09].

Bhuyan et al. studied soft x-ray emission from a 2.2 kJ plasma focus device with various anode shapes with hydrogen and nitrogen filling gas. The considered anode shapes were hollow, solid, and hemispherical anodes from which the hemispherical anode gave maximum x-ray yield with hydrogen filling gas. While the hemispherical anode shape showed spot-like pinched structure, the hollow and the solid anode shapes gave columnar pinched structure. The experiment also indicated that x-ray yield had a strong correlation with anode shape and the filling gas pressure in that x-ray yield could be enhanced by more than tenfold with appropriate anode shape and optimum gas pressure in the plasma focus device [Bhu04].

Mahtab and Habibi also studied the effect of the anode shapes on the intensity of soft and hard x-rays from a 4 kJ plasma focus device with nitrogen filling gas. The studied shapes were cylindrical-flat, cylindrical-hollow, spherical-convex, cone-flat, and cone-hollow. It was found that while the cone-flat, the spherical-convex, and the cone-hollow anode shapes enhanced the x-ray intensity, the cylindrical-hollow anode shape decreased the x-ray intensity compared to the mostly used cylindrical-flat anode shape [MH13]. It was also found that high Z anode material would give higher intensity of hard x-ray as well as the higher hard x-ray emission isotropy [Hab12a; HA10].

A table top plasma focus device (2 kJ) was investigated with different filling gases such as deuterium, nitrogen, neon, argon, and xenon with different filling gas pressures and anode lengths as intense x-ray source. It was found that neon filling gas gave rise to the maximum x-ray emission. It was also observed that atomic number of the gas had effect on the structure of the pinched plasma in that while atomic number smaller than 18 showed a uniform cylindrical column, hot spots were observed for atomic number greater than 18 [Beg00].

Neog et al. investigated optimal anode length for higher x-ray yield from a 2.2 kJ plasma focus device with nitrogen filling gas and concluded that appropriate anode length could result in optimal x-ray yield from the plasma focus devices. The highest x-ray yield was found to be 0.2% of the input energy. It was also observed that x-ray emitting zones for the optimum anode length was more intense than other anode lengths [Neo06].

Gas pressure and voltage has a strong correlation with x-ray emission. An experiment conducted with neon filing gas to observe this correlation in the plasma focus device indicated that high emission of soft x-ray and hard x-ray had different optimum conditions for both gas pressure and applied voltage. Therefore, gas pressure and applied voltages need to be arrange separately in order to achieve high emission of soft x-ray or hard x-ray from the plasma focus device [Roo11b].

Farahani et al. also studied the gas pressure and voltage effect to achieve the maximum soft x-ray and hard x-ray emission. They also investigated the way to enhance x-ray production from the plasma focus device with argon filling gas. It was found that high atomic number metal disk (such as lead) placed in copper anode tip resulted in

higher hard x-ray emission (about 23%) and higher soft x-ray emission (about 33%) [Far11].

In a study of x-ray emission from a 2.8 kJ plasma focus device with argon filling gas, two x-ray burst were observed. These were x-rays due to the focus of argon plasma and x-rays due to the fast electrons hitting the copper anode. The study also explored the effect of the device energy on x-ray intensity which indicated that the increase in device energy resulted in the increase in x-ray intensity [AH15].

Scaling laws for soft x-ray yield from the plasma focus devices have been studied for various filling gases such oxygen, nitrogen, krypton, and xenon. Akel developed scaling laws for oxygen soft x-ray yield (Y_{sxr}) [Ake13a]. Storage energy E_0, peak discharge current I_{peak}, and focus pinch current I_{pinch} were used for x-ray yield scaling laws from 1 kJ to 1 MJ plasma focus devices. The scaling laws of oxygen soft x-ray yield with pinch current, peak discharge current, and storage energy of the plasma focus devices are as follows:

$$Y_{sxr,O} = 2 \times 10^{-7} I_{pinch}^{3.45} \tag{2.1}$$

$$Y_{sxr,O} = 6 \times 10^{-7} I_{peak}^{2.92} \tag{2.2}$$

$$Y_{sxr,O} = 5.354 \times E_0^{1.12} \tag{2.3}$$

where the yields, currents, and the storage energy were in J, kA, and kJ. It was also

found that I_{pinch} was the key for high soft x-ray yield from the plasma focus device.

Scaling laws of nitrogen soft x-ray yield for storage energy from 1 to 200 kJ were determined as follows [AL13]:

$$Y_{sxr,N} = 8 \times 10^{-8} I_{pinch}^{3.38} \tag{2.4}$$

$$Y_{sxr,N} = 2 \times 10^{-7} I_{peak}^{2.97} \tag{2.5}$$

$$Y_{sxr,N} = 1.93 \times E_0^{1.21} \tag{2.6}$$

Scaling laws of krypton (Kr) and xenon (Xe) soft x-ray yield for storage energy from 2.8 to 900 kJ were determined as follows [Ake13c]:

For krypton

$$Y_{sxr,Kr} = 6 \times 10^{-11} I_{pinch}^{3.99} \tag{2.7}$$

$$Y_{sxr,Kr} = 3 \times 10^{-11} I_{peak}^{3.83} \tag{2.8}$$

$$Y_{sxr,Kr} = 0.0003 \times E_0^{1.43} \tag{2.9}$$

For xenon

$$Y_{sxr,Xe} = 7 \times 10^{-10} I_{pinch}^{4.036} \tag{2.10}$$

$$Y_{sxr,Xe} = 1 \times 10^{-10} I_{peak}^{4.04} \tag{2.11}$$

$$Y_{sxr,Xe} = 0.0064 \times E_0^{1.41} \tag{2.12}$$

Plasma focus devices can be used as a pulsed soft and hard x-ray sources for radiography applications. It can be used for biological objects [Pav14; Hus10; TS06], non-biological objects [Kan14; Ras10; Kno08; HZ07], and the radiation therapy [Cec12]. It can also be used for table-top soft x-ray microscopy of thin biological samples including insects [Raw04] as well as the imaging of moving metallic objects [Ras04] and lithography [Kat88]. Portable and compact tabletop plasma focus devices were also developed for the same purposes [Ver10b; Ras07; DL07]. The optimum values of the plasma focus devices such as the optimum pressure, voltage, anode length, and insulator length result in high contrast of images with high quality [Kan14; CM01].

Some examples of radiography applications of the plasma focus device are added here for illustration purposes. Figure 2.1 shows the radiographic images of biological objects [Pav14]. These figures are tiny lizard with 5 shots (figure 2.1a), a seed and an insect with 10 shots (figure 2.1b), a tooth with 15 shots (figure 2.1c), and human hand with 16 shots (figure 2.1d).

Figure 2.2 shows the radiographic images of non-biological objects with three shots

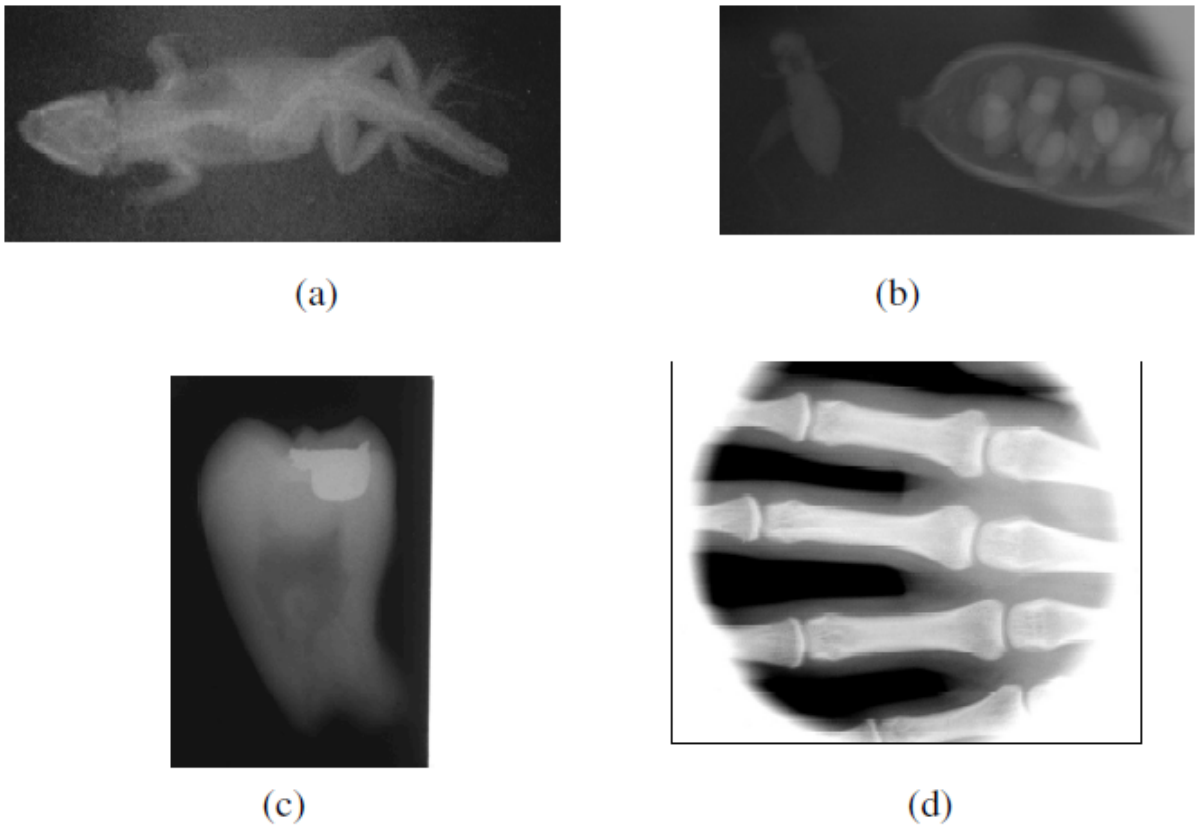

Figure 2.1 Radiographic images of biological objects [Pav14]

[Kan14]. These figures are internal circuit of an USB memory (figure 2.2a), integrated circuit (figure 2.2b), paper clip made of stainless steel (figure 2.2c), bold made of steel (figure 2.2d), and brass key (figure 2.2e).

Figure 2.3 shows the radiographic images of an aluminum turbine as a moving metallic object [Ras04]. These figures were obtained with the object at rest (static) and in fast rotation (rotating).

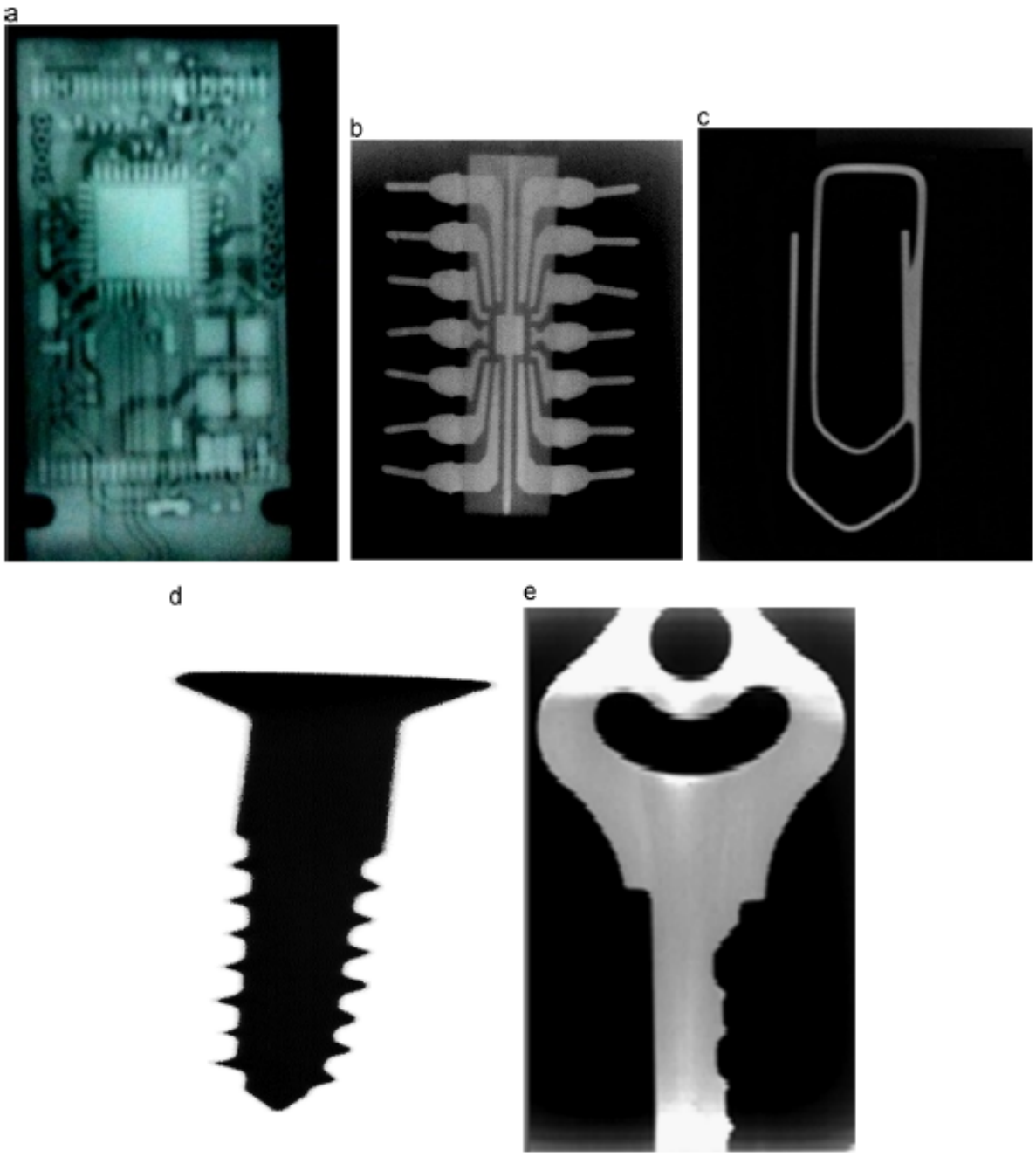

Figure 2.2 Radiographic images of non-biological objects [Kan14]

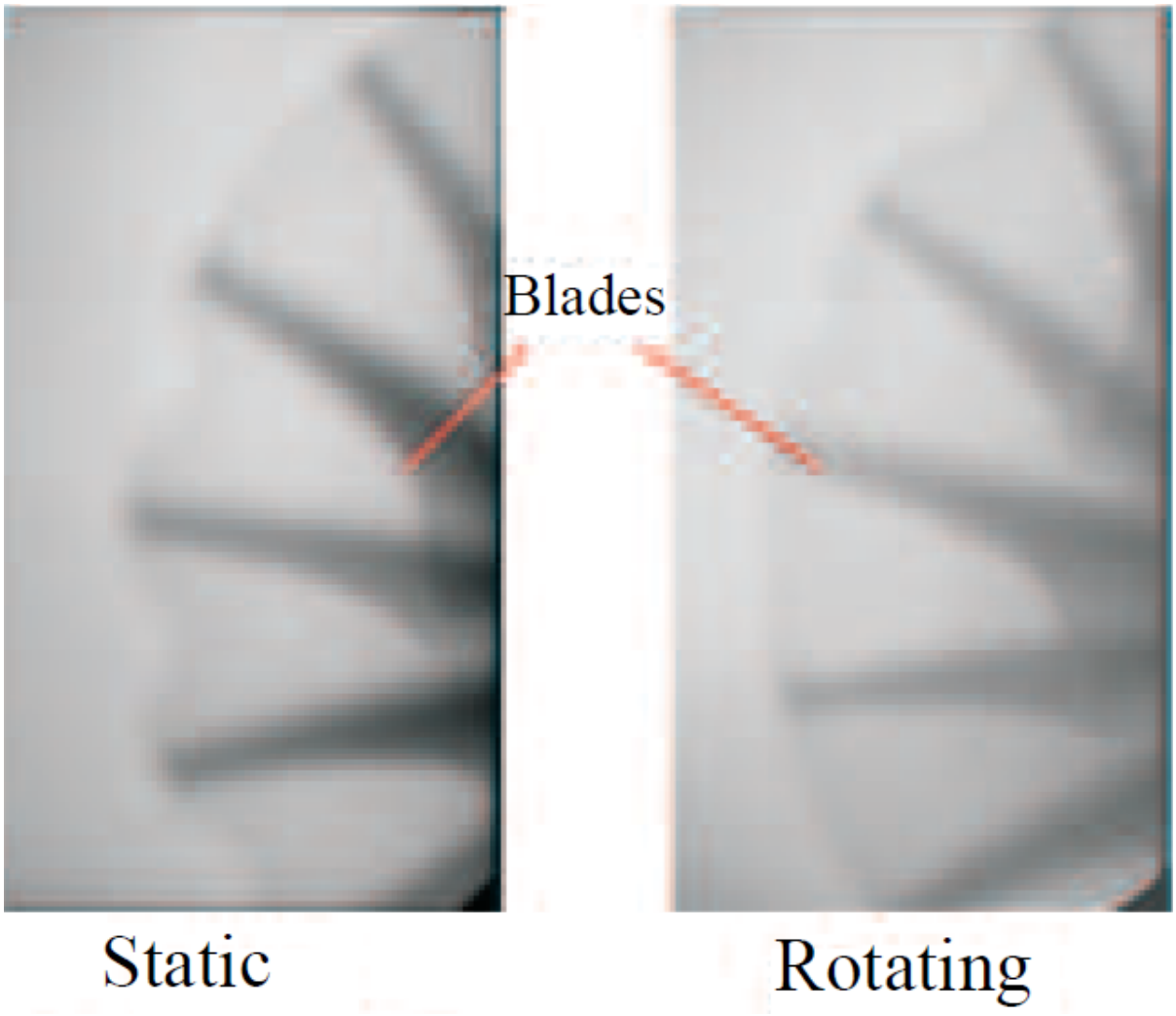

Figure 2.3 Radiographic images of moving metallic object [Ras04]

2.3 Neutrons

Plasma focus devices are efficient pulsed neutron sources resulting from fusion reactions when deuterium or deuterium-tritium mixture is used as a working gas. Neutron emission of plasma focus devices is one of the most important applications in this devices due to the fusion and hybrid fusion-fission applications [Cla15]. Even though there are many studies focusing on the plasma focus devices throughout the world, the physics behind the processes of the neutron production in the plasma focus device is still not well understood while it is an expanding area of research.

Maximum neutron yield with an optimum filling gas pressure is one of these processes in which it is believed that there is an optimum gas pressure for any plasma focus device to produce the maximum neutron yield.

Neutron yield from shot-to-shot of the same plasma focus device has fluctuations for the same operating conditions such as the same electrode geometry, voltage or pressure. This neutron yield fluctuation is another process for which the reasons are not completely clear even though the problems in the discharge initiation and the presence of contaminants inside the gas chamber may be considered as reasons of this fluctuations [TSS14].

Design and operating parameters such as the pinch current, capacitor bank energy, filling gas pressure, electrodes dimensions and material, insulator dimensions and material, added gas, and pre-ionization are some factors which have considerable effect on neutron yield from plasma focus devices.

The effect of the gas chamber volume, the gas-flow rate, and the gas flow path

on the neutron production were studied in a small plasma focus device to improve the neutron production. It was found that the effect of the gas flow-rate on neutron production were higher than that of the chamber volume and the gas flow path. It was also observed that the effect of the single modification of the gas chamber volume, the gas-flow rate, and the gas flow path was independent from each other. Therefore, it was concluded that the neutron production from the plasma focus device could be improved by combining several modifications of these factors [TSS14].

Neutron production mechanism is another unclear process in the plasma focus devices. Mostly accepted neutron production mechanisms in the plasma focus devices are thermonuclear neutron production mechanism [Kli12; AK10] where neutrons are produced in the thermal equilibrium because of the interaction of the thermal deuterons at the maximum compression of the pinch. Another is the beam-target neutron production mechanisms [Bag11b; Moh11; Ver09b; You06b; Koh05b] where neutrons are produced by accelerated deuterons colliding with the thermal deuterons in the plasma or the ambient deuterium molecules outside the plasma after the maximum compression of the pinch.

Regardless of the neutron production mechanisms, the neutron yield (Y) is proportional to the stored energy E_0 of the device as $Y \sim E_0^{2-2.4}$, which is a scaling law for neutron yield [Mor15]. The increase in the stored energy of the plasma focus device to a very large values gives rise to the current saturation which leads to the neutron yield saturation due to the dynamic resistance [Lee09].

An experiment with a small plasma focus device (4.7 kJ) with deuterium filling gas was conducted to study the emission of deuterium fusion neutrons (2.45 MeV). The

obtained neutron yield in this study was $(5.3 \pm 0.5) \times 10^8$ neutrons/shot with 2.75 Torr deuterium pressure. Both isotropic and anisotropic neutron emissions were observed with higher isotropic neutron emission contribution to total neutron yield. Even though neutron energies from this experiment peaked at 2.45 MeV, which showed a strong thermonuclear neutron production mechanism from the D-D reaction, the energies of neutrons were spread from 1.7 MeV up to 4 MeV which indicated the existence of a strong beam-target neutron production mechanism contributing to the process [CM14].

The neutron emission with 2.2 kJ plasma focus device was also investigated by using deuterium filling gas. In this experiment, two pulses of neutron emission were observed with highly anisotropic neutron yield and neutron energy which indicated that the beam-target neutron production mechanism was the main neutron production mechanism in this device. It was also concluded in this experiment that two consecutive disruptions in this small plasma focus device might be responsible for two neutron pulses [Tal14].

Another unclear process of the dense plasma focus devices is if neutrons are produced as a single phase or multiple phases in the discharge. Even though mostly observed neutron production from the dense plasma focus is a single phase event which occurs at the same time of the hard x-ray emission [Mor15], two phase of neutron production were also observed from medium energy (tens of kJ) plasma focus devices [Yap05; ARC98] and mega-joule plasma focus devices with the first neutron pulse corresponding to soft x-ray and the second neutron pulse corresponding to the ion beam emission. Therefore, it can be concluded that the first neutron pulse

is mainly due to the thermal neutrons, and the second neutron pulse is due to the beam-target mechanism [Sch04].

Moreno et al observed neutron emission on the radial direction as well as the axial direction with different neutron energies and different neutron yields from a 320 J plasma focus device using deuterium as a working gas. This directional difference was concluded as both a clear anisotropy and the existence of two temporally separated neutron pulses, but the reasons for the multiple pulses in the plasma focus devices are not clear [Mor15].

It has been reported that while the time for the first neutron pulse, which carries about 10-20% of the total neutron yield, is corresponding to the time of maximum compression of pinch with the highest plasma density, the time for the second neutron pulse, which occurs during the expansion phase with broad plasma column and carries 80-90% of the total neutron yield, is about 100 ns after the first pulse is emitted [ARC98].

Another experiment with a 28 kJ plasma focus was conducted to study the spatial anisotropy of the neutron emission with deuterium as a working gas [ARC98]. Two periods of neutron emission were observed in this medium energy plasma focus device. The beginning of the first period of the neutron emission in this experiment occurred between the final phase of the radial compression of the plasma column and the formation of the hot plasma pinch column. The first period of the neutron emission lasted less than 50 ns. Therefore, it was concluded that neutron production in the first period was because of the radial acceleration of the ions, which can gain energy up to 100 keV by bouncing off the incoming sheath four times with the sheath

velocity of 30 cm/μs.

While the neutron production of the first period peaked at the time when these ions interact with the dense plasma column, it peaked well after the first compression for the second period of neutron emission, which was due to an axially directed ion beam-hot plasma interaction. The second period of the neutron emission lasted between 150 and 200 ns with the dense, hot plasma column moving away from the anode. The observed anisotropy from the neutron emissions in this experiment is also agreement with the hypothesis that there were two different neutron production mechanisms in this medium energy plasma focus device [ARC98].

A compact pulsed plasma focus device as a neutron source was developed and optimized to investigate the physical processes of a sub-kilojoule (600 J), repetitive plasma focus device, in which a neutron flux of $\sim 10^8$ neutrons/s was produced with repetition rate of up to 10 Hz, burst duration of up to 3 s, and discharge current of 80-90 kA [Vin14].

The effect of pre-ionization around the insulator sleeve of the plasma focus device caused by an α source and a β source on the neutron yield were investigated [Ahm14; Ahm06b; Zak03]. Pre-ionization increased the neutron yield by 20 % and 25% for the α and β sources, respectively, as well as the shot-to-shot reproducibility of the plasma focus device for neutron yield.

Zavyalov et al. obtained neutron yield of of $\sim 1.3 \times 10^{13}$ neutrons by using DT mixture with $\sim$ 1.5 MA discharge current from a spherical plasma focus chamber [Zav13].

Kubes et al. replaced the copper circuit plate with tungsten in the axial center of

the anode face in a 350 kJ plasma focus device with deuterium filling gas and 2 MA discharge current to investigate the effect of the evaporated tungsten from the anode into the plasma column, by the impact of the plasma during the pinch phase, on the neutron yield; the obtained neutron yield was more than 10^{10}. It was observed that the evaporated tungsten caused a decrease of about 60% from 1.7×10^{11} to 0.7×10^{11} and a 20% decrease in the neutron mean energy as compared to the copper anode face [Kub13].

A fast miniature 200 J plasma focus device produced the time averaged neutron yield of $(1.4 \pm 0.2) \times 10^7$ neutrons/s at 10 Hz discharge repetition rate with deuterium filling gas. It was predicted that if the filling gas was deuterium-tritium mixture at the same repetition rate, the neutron yield of about $7.0 \times 10^8 - 1.4 \times 10^9$ could be achieved due to the higher reaction cross sections of D-T gas mixture compared to the D-D reactions. It was found that the optimum gas pressure of the repetitive mode was higher with better reproducibility in neutron emission than that of the single shot mode. Therefore, it was necessary to optimize the gas pressure of these two modes separately [Ver13].

A low energy (2 kJ) plasma focus was developed as a clean, cheap, and portable pulsed neutron source to determine the chemical composition of substances by nuclear activation technique. The characteristic emission line of manganese, gold, lead, and silver were shown using this source [Mil13].

A correlation between the neutron yield, the neutron yield anisotropy from the plasma focus devices, and the jump in the discharge currents was experimentally observed in that there was a linear dependency between them at the time of neutron

production. The neutron yield of 20 kJ and 130 kJ plasma focus devices were (0.5-1.5)$\times 10^9$ and (3-5)$\times 10^{10}$ neutrons per shot, respectively [Abl12; Abl10].

Various phases of neutron emission were observed from a plasma focus experiment with the stored energy from 280 kJ to 500 kJ. The observed phases were 1) a compression of the plasma structure to a minimum diameter, 2) a slight expansion of the plasma structure, 3) an instability phase, and 4) the dense plasma structure decay phase. Double neutron pulses were also observed which were coincident with the time of the compression of the plasma structure to a minimum diameter and the instabilities [Kub12b]. In these two pulses, while the main neutron production mechanism was the beam-target mechanism, the estimated thermonuclear neutron production was less than 5% for both pulses [Sch12b].

Velose et al. studied the discharge characteristics in terms of the neutron yield from a 400 J plasma focus device by using deuterium filling gas. It was found that while higher plasma inductance, mechanical energy, and plasma voltage at the pinch time resulted in high neutron yield, the filling gas pressure had a strong effect on the geometry of the current sheath in that lower gas pressure lead to larger curvature of the current sheath [Vel12].

An experiment was carried out to enhance the neutron yield from a 90 kJ plasma focus device with krypton seeded deuterium filling gas. While the best average neutron yield with pure deuterium gas for the same conditions was 3.18×10^8, it was 2.2×10^9 neutrons per shot at 1 Torr gas pressure of deuterium with 3% krypton at the charging voltage of 18 kV [Moh11].

The effect of changing the anode geometry and mixing the admixture gases (Argon

and Krypton) with deuterium filling gas were investigated to enhance the neutron yield in the plasma focus device [TK10]. Plasma focus anode geometry was changed from the cylindrical shape to the conical shape which increased the neutron yield by a factor of 5 in pure deuterium but did not increase the neutron yield for deuterium mixed with 2%, 4%, and 8% argon and krypton. Deuterium mixed with argon and krypton resulted in a factor of 3.6 higher fold neutron yield increase for the cylindrical anode compared to pure deuterium cylindrical case [Bur10].

Kubes et al. determined the energy distribution function of neutrons from which the axial and radial components of the neutron producing deuterons (from fusion reactions) as well as the total energy distribution of fast deuterons in the pinch were obtained in a 500 kJ plasma focus device. Neutron producing fast deuterons had a wide range of energy changing from the lower energy limit of 10 keV, which is due to the small D-D fusion cross section, to the upper energy limit of 300 keV, which is due to the low number of the most energetic deuterons [Kub09].

Hussain et al. studied the correlation of neutron yield and the pinch energy with the anode shape in a 2.7 kJ plasma focus device. They investigated the cylindrical anode which produced the neutron yield of 1.3×10^8 neutrons per shot and converted 24% of the input energy to pinch energy at the optimum gas pressure. They also studied tapered anode (the anode with a reduced radius towards the end) which increased the neutron yield to 1.6×10^8 neutrons per shot, enhanced the neutron flux of both axial and radial directions about 25% and increased the converted pinch energy to 36% of the input energy at the optimum gas pressure. It was found that the anode shape had a considerable effect on the neutron yield and optimum gas pressure [Hus09].

Verma et al. reported the effect of two different shapes of plasma focus cathodes, tubular cathode and squirrel cage cathode, on neutron yield in a miniature plasma focus device with 230 J stored energy. While the neutron yield of the squirrel cage cathode was 1.15×10^6 neutrons per shot at 6 mbar filling gas pressure, it was decreased to 1.82×10^5 neutrons per shot at 4 mbar by using the tubular cathode due to the reduced pinch current and the additional impurities from the cathode wall during the axial flow [Ver09a].

The right amount of krypton in deuterium can considerably increase the neutron yield [Gou07]. While the maximum average neutron yield was 1×10^4 neutrons per shot for deuterium filling gas at 3 mbar in a miniature 200 J plasma focus device, it was increased to 3.14×10^5 neutrons per shot for the mixture of deuterium with 2% krypton [Ver08].

Yousefi et al. observed both multiple and single compression mechanisms from a middle energy plasma focus device (20 kJ). The multiple and single compression occur depending on the gas pressure, while low gas pressure leads to the multiple compressions due to the $m=0$ instability which is a necessary condition for fusion. The single compression occurs at higher gas pressures, which has higher neutron intensity than multiple compression regimes. They also observed multiple deuteron and neutron pulses which show that ions are accelerated with a different mechanism in addition to the $m=0$ instabilities [You06a].

2.4 Ion Beams

Plasma focus devices produce energetic ion beams with energy ranging from a few keV to MeV [GS78; Bos93; Sot05], and their energy can be much larger than the charging voltage of the capacitor bank. These energetic ions are considered as one of the main factors which produce the intense neutrons from the plasma focus device when deuterium is used as a working gas. The ion beams are investigated for a wide range of plasma focus devices ranging from 1 kJ to 1 MJ [Gri15]. Since the ion beam leaves the focus pinch along its axis, and it is a narrow beam with little divergence, this exit beam can be characterized by the ion number density per shot, which was termed as fluence per shot [LS13].

Lee and Saw investigated the scaling of deuteron beams in terms of the fluence and flux with the stored energy by using Lee Model code [LS12]. The variation of the stored energy of the plasma focus device was from 0.4 kJ to 486 kJ for which the ion number fluence (ions/m^2) and energy fluence (Joule/m^2) were not dependent on the stored energy. The computed ion number fluence and energy fluence were ranging from 2.4×10^{20} to 7.8×10^{20} ions per m^2 for the fluence and from 2.2×10^6 to 33×10^6 J per m^2 for the energy fluence. They also studied the plasma focus devices with various inductance values. While the plasma focus devices with the inductance ranging from 33 nH to 55 nH generated $1.2-2 \times 10^{15}$ ions per kJ with 1.3% - 4% of the stored energy and with 50 - 205 keV range of the mean ion energy, the plasma focus devices with higher inductance (110 nH) produced 0.6×10^{15} ions per kJ with 0.7% of the stored energy [LS12].

Akel et al. modified the Lee's model for characterization of the oxygen ion beams emitted from the low energy plasma focus device (1 kJ). The obtained results from this numerical experiment were ion fluence of 3×10^{18} ions m^{-2}, ion flux of 24×10^{26} ions m^{-2} s^{-1}, ion energy of 261 keV, ion number of 3.5×10^{13}, and ion current of 3.5 kA. They also run the same numerical experiment for different energy plasma focus devices (from 0.4 kJ PF400 to 500 kJ PF1000) to suggest a scaling trends for oxygen ion beam characteristics.

For the number of beam ions leaving the focus pinch area, they found that it was ranging from 2×10^{17} ions for the 500 kJ PF1000 to 5×10^{13} ions for the 0.4 kJ PF400. They also found a strong correlation between the number of ions exiting the pinch and the bank energy of the plasma focus devices. Increasing the bank energy of the device increases the number of beam ions exiting the pinch.

The ion number fluence (ions per unit beam area) was another ion beam characteristic from this numerical experiment. It was ranging from 3.4×10^{19} ions/m^2 for the 0.4 kJ PF400 to 2.7×10^{20} ions/m^2 for the 500 kJ PF1000. Even though there is a huge stored energy variation of the plasma focus devices in this numerical experiments, there was only a factor of 8 through the huge range of bank energy from 0.4 kJ to 500 kJ plasma focus devices. Therefore, they concluded that there is no clear correlation between the ion fluence, the ion flux (fluence per unit time) and the bank energy [Ake14b].

Another numerical study was carried out for various plasma focus devices with nitrogen filling gas. The main objective of this numerical experiment was to determine the ion properties such as ion beam energy, ion beam flux, ion beam fluence, beam

ion number, and ion beam current versus the filling gas pressure for each plasma focus devices. It was found that while increasing the gas pressure increased the beam ion number but decreased the mean ion energies, the optimum gas pressure led to the maximum value for ion beam fluence, ion beam flux, and ion current. It was calculated from the numerical experiments of nitrogen plasma focus devices that while the ion beam energy range was from 20 keV for ICTP PFF at 2.2 Torr to 1700 keV for PF1000 at 0.1 Torr, the peak values of the ion beam fluence range was from 10^{18} to 10^{20} ions/m^2, and the beam ion number/kJ ranges from 10^{13} to 10^{14}. Beam ion currents and the beam energy were also calculated ranging from 3.5 kA to 490 kA for the beam ion currents and from 0.03 to 5.3 % of the bank energy for the beam energy [Ake14a].

A numerical experiment for various gases such as $H_2, D_2, He, N_2, Ne, Ar, Kr, Xe$ was carried out to compute the ion beam properties of the plasma focus device. It was shown that increasing the mass number of the gas decreased the fluence, flux, ion number, and ion current except that argon had the higher values of the fluence and flux. Even though the energy fluence and energy flux from H_2 to N_2 were not changing much, they were increasing for Ne, Ar, Kr, and Xe because of the radiative cooling and collapse effects. While the ion fluence was decreasing from 7×10^{20} for the lightest gas H_2 to 0.8×10^{20} for N_2, the fluence for Ne and Ar increased to 4.3×10^{20} because of the radiative collapse which constricts the pinch to a smaller radius. While the ion number per kJ is 86×10^{14} for H_2, 4×10^{14} for Ne, and 0.06×10^{14} for Xe, the ion current was 26% of the discharge current for H_2, 11% for Ar, and 1% for Xe. The beam energy was 7.5% of the bank energy for H_2, 4.7% for N_2, and it increased a little bit for Ne,

Ar, Kr, and Xe. It was concluded from this numerical experiment that argon could be a good candidate for many purposes in plasma focus devices because it has large ion fluence and ion flux, and it also has a good beam energy and current for a large operational gas pressure [LS13].

It is important to characterize and diagnose the ion beams for not only understanding the production of high-energy ion/neutron mechanisms but also for investigating their acceleration mechanism and recent/possible applications such as ion implantation, thin film deposition, and the production of the short-lived radioisotopes [Ang05; GS04; Raw01; Kan97].

An experimental study with a 3 kJ plasma focus device was conducted with deuterium filling gas at low pressure regime to diagnose the ion beam emission. The optimum gas pressure was determined as 0.2 mbar for this experiment. In order to find the energy spectrum and total number of the ions in this experiment, biased ion collectors, Faraday cup, and solid state nuclear track detector CR-39 were used as diagnostic techniques. While the average total number of deuterons was determined from the Faraday cup signal as $(4.0 \pm 0.1) \times 10^{11}$ per shot, average ion beam energy was found from the biased ion collector as (57 ± 16) keV. The ion angular distribution from this experiment was determined by the solid state nuclear track detectors from 30° to 90° angle [Lim14].

The angular distribution and the energy spectrum of the argon ions, which was corrected for the ion energy loss and charge exchange in the background gas, were measured in a 90 kJ plasma focus device by using a Faraday cup which was also optimized to minimize the effect of the secondary electron emission on the ion signals

by optimizing the aspect ratio of the Faraday cup. It was found that the emitted number of ions per energy was increased with both increasing the capacitor bank voltage and decreasing the filling gas pressure. It was also found that the angular distribution of the emitted argon ions was highly anisotropic [Moh13; PM15].

The current drop in the plasma focus devices has a strong correlation with the ion beam emission intensity and lifetime during the radial phase for both the low range of 0.2-0.8 mbar and the high range of 0.8-1.5 mbar filling gas pressure. In an experiment with a low energy (up to 4.9 kJ) and high inductance (148 nH) plasma focus device, it was found that the increase in anomalous resistance leads to a long drop in the current signal and high intensity ion beam emission, which also results in increasing the energy transferred into and consumed by the plasma in the low pressure range. The anomalous resistance and both transferred and consumed energies decrease in the high range pressure of the plasma focus device, which causes short current dips in addition to the low intensity ion beam emission. The filling gas pressure has also effect on instabilities in that decreasing the gas pressure from high range pressure to low range pressure increases the effect of instabilities in the dense plasma focus device [BA12].

Lerner et al. observed deuterium ions with energies of greater than 150 keV in the fusion reactions from a 50 kJ capacitor charge plasma focus device. The observed confinement time of the deuterium ions were 7-30 ns in the cores of the plasmoids which is dense magnetically confined hot plasma (or pinched plasma). They also concluded that the confined high-energy ions (not an unconfined beam) were responsible for at least 70% of the neutron production per pulse (up to 1.5×10^{11} neutrons) [Ler12].

Faraday cup in a time of flight method was used to measure the nitrogen ion properties in a plasma focus device with the optimum working conditions (14 kV, 0.25 Torr). While the ion energy range was from 8.5 keV to 76 keV, the variation of the ion current density was from 3.2×10^{15} to 4.5×10^{6} A/m^2 [GM12].

It was found that there was a strong correlation between the argon ion beam emission and gas pressure in the plasma focus device with charging voltage of 12 kV and the pressure range from 0.8 to 3 Torr. The gas pressure of 1 Torr was found as an optimum pressure for ion beam emission, which lead to the maximum ion density of 9.24×10^{24} ions/steradian. It was also seen that increasing the gas pressure decreased the ion flux [Eta11].

Multiple ion beam emissions were observed in a low energy plasma focus device (up to 4.9 kJ) with more than 100 nH inductance. It was concluded that anomalous resistance and the effects of the instability were responsible for the multiple ion beam emission in this experiment [BA11].

Energetic and intense ion beams with good reproducibility in a 3 kJ plasma focus device with the deuterium gas pressure varying from 0.05 to 0.5 mbar were obtained and studied by using ion collectors for determining the deuteron beams and time-of-flight method for the average energies of the deuteron beams. The optimum pressure was found to be 0.1 mbar which led to the highest flux of deuteron beams with about 75 keV energy [Lim11].

Bhuyan et al. investigated the temporal and spatial characteristics of the neon ion beam emission with various gas pressure from a low energy (2.2 kJ) plasma focus device by using a Faraday cup and the CR-39 track detectors which were placed at

various angular and axial positions. While ion flux (highest at 25° angular position with 0.3 Torr gas pressure) has a strong correlation with the gas pressure and angular positions, the energy variation of poly-energetic ions, which were produced by the plasma focus device, were from a few keV to hundreds of keV, regardless of the gas pressure and the angular positions. The majority of the ion population were below 180 keV with the maximum ion density of $5 \times 10^{19}/\mathrm{m}^3$ at optimum gas pressure of 0.3 Torr. Neon ion flux and energy distribution were predicted inside the plasma focus chamber, which will be helpful to test the considered materials for the next generation fusion reactors [Bhu11].

Mohanty et al. studied different designs of the cylindrical anode effect (hollow, solid, and hemispherical anode tip) on the ion beam emission in a 2.2 kJ plasma focus device with nitrogen filling gas as well as the gas pressure and angular position effect on the ion beam characteristics such as ion flux and energy. They found that even though the ion flux did not strongly depend on the anode design but the gas pressure, the maximum ion flux was found in case of the hemispherical anode with the emission of the highest energetic ions (830 keV), and it was lowest in case of the hollow anode. The gas pressure of 0.3 to 0.5 Torr was found to be the optimum gas pressure for all the anode designs [Moh07b].

The purity of ion beams can be improved by the shape of the anode in a plasma focus device. In an experiment with 19.4 kJ plasma focus device with nitrogen filling gas, two types of anodes were investigated to improve the purity of ion beams. These were rod type and hollow type anodes from which both types had 550 kA peak discharge currents. While there was a strong electron irradiation on top of the rod type anode

which resulted in vaporization of the electrode material which was then mixed with the pinch plasma and accelerated with the nitrogen ions, electron irradiation was not strong, and the irradiation area was not close to the pinch plasma for the hollow type anode. Therefore, it was found that while rod type anode had 25% nitrogen ions (25% purity), hollow type anode extremely increased the purity to 91% of nitrogen ions [Tak03].

Yousefi and Masugata extended this experiment by including the long hollow anode, short hollow anode, and rod type anode to observe more of the effect of the anode impurity on the neutron production in the plasma focus device. They found that the neutron intensity and neutron yield were the lowest in the rod type anode and the highest in the long hollow anode. They concluded that neutron production had a strong correlation with anode shape and high purity ion plasma in the plasma focus devices [YM11].

Sohrabi et al. developed an efficient method based on the electrochemical etching of the ion tracks to detect and observe the helium and nitrogen ion track densities with their angular distribution (by unaided eyes) in a 4 kJ plasma focus device by applying a 50 Hz-high voltage generator [Soh12; Soh14].

2.5 Electron Beams

Since there is a need of the electron beam sources for many applications such as biophysics, biohazard prevention, and sterilization, a plasma focus device can be a good candidate for various technological applications [NM07]. Plasma focus devices with its self-generated magnetic field produce a transient high density and high temperature plasma column (pinch). After the disruption of the pinch column, the energetic electrons and ions are emitted. While electrons are emitted towards the anode, ions are emitted towards the cathode.

The emission of the energetic electron beams is observed from the plasma focus devices, and the energy of this electron beams are much higher than that of the charging voltage of the capacitor bank.

Electron beam current and density are strongly dependent on the filling gas pressure. At the optimum gas pressure of 0.3 Torr of nitrogen gas, the average electron beam current was about 13.5 kA from a 2.2 kJ plasma focus devices, and the electron beam emission has its maximum value at this optimum gas pressure which were measured by using a Faraday cup and Rogowski coil assembly. The approximate electron energy distribution in the beam from the same plasma focus device was measured from 10 keV to more than 200 keV by applying self-bias technique but the range of energetic electrons from 80 to 110 keV was the most probable distribution from this experiment [NM07].

Study of two medium-size plasma focus devices with the energy range from 37 kJ to 170 kJ showed that plasma focus devices were efficient source of pulsed electron

beams and pulsed x-rays. The x-ray emission from this experiment had a wide range of energy from soft x-rays to hard x-rays which had a well correlation with peaks of the electron beam emission [NM07].

Hard x-ray is one of the radiations emitted from the plasma focus devices. The main reason of hard x-ray emission is the electrons formed in the pinch, which are hitting the anode of the plasma focus device or a special target placed near the anode. Therefore, while the electron beam parameters such as duration, current, and the energy of the accelerated electrons are useful to determine the hard x-ray characteristics in the plasma focus device, temporal characteristics of the measured hard x-ray can also provide information on the electron beam parameters and the mechanisms for the electron beam production in the device. There are some mechanisms to produce the electron beams in the plasma focus devices such as anomalous resistance effect, accelerating electromotive force as well as the process occurring in the hot spots of the pinch. A fast electron production mechanisms that takes into account both the effect of the anomalous pinch resistance and the current redistribution in the near-pinch region was proposed by Dulatov et al [Dul14].

The instabilities developed in the pinch cause a region of anomalous resistance which is higher than that of the heated pinch plasma resistance. Sharp decrease of the current in this region due to the anomalous resistance gives rise to the production of a strong longitudinal electric field, which accelerates the electrons in this region with the anomalous resistance because of the electromotive force which prevents the sudden drop of the current flowing through the pinch even if there is a sharp current decrease in this region in the pinch. During the process of the pinch decay, there is a

re-distribution of the current, which is mainly determined by their resistance, between the dense hot pinch and the surrounding plasma. While the anomalous resistance has the highest resistance value, the plasma surrounding the pinch has higher resistance value than that of hot pinch plasma. Therefore, a considerable amount of discharge current is flowing through the plasma surrounding the pinch which results in less current flowing through the pinch with the anomalous resistance [Dul14].

There are mainly 3 proposed mechanisms to explain the acceleration of electrons up to the energies of about MeV in the plasma focus devices. While the inductive method as the most common mechanism explains the accelerating of the electrons with the rapid local changes in the magnetic flux (inductive generation), which is responsible for the high electric field in the plasma, from the onset of the radial phase and $m = 0$ instability mode in the plasma focus devices, the anomalous resistivity effect results in the generation of a strong electric field along the pinch filaments to accelerate the electrons even if there is almost no change in the plasma current. The rupture of conductivity current because of the neck development and the current displacement is another mechanism proposed for understanding the mechanism of energetic electrons [BA13].

Both single and multi time-period emission of the electron beam were observed when studying the effect of anomalous resistance on the electron beam emission in a low energy plasma focus by using a fast-calibrated Rogowski coil. While single time-period emission was observed in the high pressure range (0.8-2 mbar), single and multi-emission of electron beam were observed in the low pressure range (0.2-0.8 mbar) [BA13].

Electron beam intensity and energy was simultaneously measured in a low-energy plasma focus device (2.2 kJ, 12 kV) with an optimum argon gas pressure of 1.7 mbar by using a combination of Faraday cup and photodiode. While the measurement with the self-biased Faraday cup was 500 keV for the average electron beam energy, the maximum density of the electron beam was found to be 13.5 $\times 10^{16}$ per m^3 [Kha14]

An experiment with a 3 kJ plasma focus device by using neon as filling gas with the charging voltage of 14 kV was carried out for the gas pressure ranging from 1.5 mbar to 5.5 mbar to investigate the electron beam emission and to find the correlation of the electron beam with operating conditions and x-ray emissions in the different energy ranges by using both a magnetic electron energy analyzer (in the 30 - 660 keV range) and a Rogowski coil. The electron beam from the plasma focus device showed a very strong correlation with the main discharge current signal (i.e., with the general plasma dynamics), operating conditions, and the x-ray emissions. The optimum neon gas pressure for this experiment was 4 mbar which maximizes the total electron current and the peak energy of the electron distribution as well as the good shot-to-shot reproducibility of the plasma focus device. It was observed from the energy spectra of the electrons that while the most of the electrons had energy below 200 keV, there were some negligible emission of the electrons with energy above 350 keV [Pat05].

The pulsed electron beams from the plasma focus device operated up to 45 kJ was observed both along and perpendicular to the z-axis. While the electron beams along the z-axis were emitted from the plasma regions (hot-spots) inside the plasma focus pinch column, the electron beams perpendicular to the z-axis were emitted due

to the strong instabilities in the current sheath. This perpendicular electron beams were observed about 100 ns before the dip in the discharge current which coincided with the emission of the x-ray spectral lines. It was also found that there is a good correlation between x-ray emission and the electron beams emitted perpendicular to the discharge axis in the plasma focus device [Jak04].

The electron density and current profile were determined by using laser interferometry and polarimetry. The electron density in the pinch plasma was measured as around 3×10^{19} cm^{-3} [Qi98].

Electron energy greater than 350 keV (around 10 % of population) were observed from 70 kV (380 kJ) plasma focus device. It was also observed from time resolved electron induced signals that there were 2 pulses in 90% of the discharges with usually 120-150 ns apart. While first pulse can be related to the maximum compression, the second pulse was attributed to the $m = 0$ instability [Jak91].

Two periods of the electron beam emission were observed from a 60 kV, 28 kJ plasma focus as well. While the first electron beam emission period, which has high-energy electron beams, starts with the formation of the plasma and ends with the disruption of the plasma column, the time of occurrence for the second electron beam emission period, which has lower energy electron beams with higher current, is after the breaking up of the focus plasma [Cho90].

The energy distribution of the electron and ion beams from the plasma focus device are measured using Rogowski coils for time-resolved measurement and solid-state nuclear track detectors for time-integrated measurement of the beams with the bank voltage of 15 kV and 4 Torr deuterium gas pressure. Electron beam emission was

observed in the upstream direction (towards the anode), and ion beam emission were observed in the downstream direction (away from the anode).

For the electrons emitted in the upstream direction which was approximately 1 % of the discharge current, while the energy range of the electrons in the beam were from 0.1 MeV to 1 MeV, the maximum population of the electrons were confined to the energy range from 150 keV to 200 keV. On the other hand, for the ions emitted in the downstream direction of the plasma focus device, two successive ion emissions were observed in that while high energy ions (a few MeV) with a low beam current (less than 10 A) were observed in the first emission which also coincides with the generation of the electron beam, the second ion beam emission, which is the main part of the ion beam, was observed about several tens of nanosecond after the first emission was observed. While the energy range of the second ion beam emission were varying from 100 keV to 800 keV from shot to shot, the most frequent ion energy range was from 300 to 400 keV [Yam82].

Vaporization of metals in the electrodes by runaway electrons produces impurities which cause the fusion yield reduction in high-current dense plasma focus devices. It is not an issue for low current dense plasma focus devices. This process occurs during the breakdown at the beginning of the current pulse, and it is responsible for the erosion of the anode close to the insulator. Low gas pressure and large electrode radii can make erosion worse which causes the plateau of fusion yield even if the peak current is increased to a higher value. Therefore, the runaway electron vaporization effect should be eliminated to achieve higher fusion yield. In order to eliminate the runaway electron vaporization, electrode material should be chosen correctly, sufficiently

small-radius electrodes should be used for high current so that filling gas pressure is increased. Generated electric field during the breakdown process also produce runaway electrons which can be prevented by using pre-ionization for higher fusion yield [LY14].

CHAPTER

3

PLASMA SHEATH DYNAMICS IN THE SPHERICAL PLASMA FOCUS

In order to study plasma sheath dynamics in the spherical plasma focus device, a plasma focus model, which consists of rundown phase I, rundown phase II, and reflected shock phase for a spherical plasma focus device, has been developed. The developed model was validated versus experimental results. The snow plow model with the help of the shock wave equations coupled to the circuit equations is used

to predict the plasma and shock wave parameters in the spherical plasma focus device. The set of equations describing the developed model are solved with the linear approximation method as follows [M. 10]:

$$\frac{d\theta}{dt} = \frac{d\theta}{dt} + \frac{d^2\theta}{d^2t}D \tag{3.1}$$

$$\theta = \theta + \frac{d\theta}{dt}D \tag{3.2}$$

$$I = I + \frac{dI}{dt}D \tag{3.3}$$

$$\int I\,dt = \int I\,dt + ID \tag{3.4}$$

where θ is the angle corresponding to the position of the current sheath, D is the incremental time for each next step values, I is the discharge current.

This model is able to predict the temporal evolution of the current, inter-electrode voltage, and temperature and velocity of the current sheet. The model was also run to gain insight on the effect of the gas pressure and discharge voltage on plasma temperature and pinch start time for hydrogen, deuterium, and tritium. Plasma parameters were also calculated and compared for the working gases of hydrogen, deuterium, and tritium.

3.1 Spherical Plasma Focus Model

A model for the Spherical Plasma Focus (SPF) device has been developed, which consists of three phases: a rundown phase I, a rundown phase II, and a reflected shock phase. Figure 3.1 illustrates the configuration of the spherical plasma focus showing the inner and outer electrodes, the insulator, the current sheath (CS), and the equivalent circuit model which consists of the circuit inductance L_0, resistance r_0, the capacitor bank C_0, and the closing switch. The equivalent circuit has V_0 charging voltage which is applied across the insulator after closing the switch and discharging circuit capacitance C_0 through L_0 and r_0.

A model was also developed for the plasma focus device with hemispherical electrodes [M. 10]. In this model, snowplow model, the momentum equation, plasma circuit equation, and shock wave equations were used to simulate the hemispherical plasma focus device. In this hemispherical model, the motion starts at the equator and ends at the antipodal point of the hemisphere.

While the angle of the motion varies first from one antipodal point to the equator point then to the other antipodal point resulting in 3 phases which are a rundown phase I with sheath expansion, a rundown phase II with sheath compression, and the reflected shock phase in the spherical case, the hemispherical case has one phase due to the different electrode shape which has angle varying from equator point to the antipodal point.

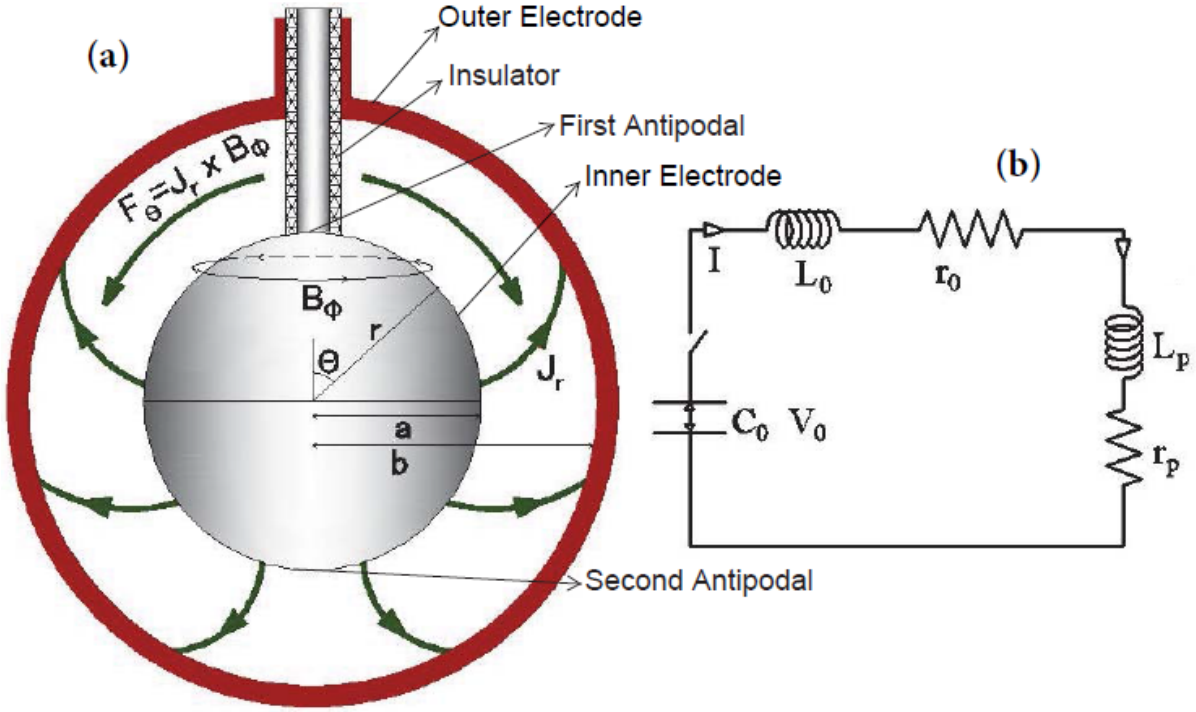

Figure 3.1 (a) Spherical plasma focus configuration. (b) Equivalent circuit model of the SPF

Since the shape of the plasma focus device is spherical, the angle of the plasma sheath and the angle variation are important factors for the motion of the plasma sheath and related parameters such as magnetic field and the plasma inductance which can be seen, for example, in equations 3.16 and 3.45 for the plasma sheath motion, equations 3.14 and 3.40 for the magnetic field, and equations 3.21 and 3.48 for the plasma inductance. A clear plateau is observed in the results of the velocity and temperature while the current increases. Such behavior was not observed in the results of the hemisphere model.

In order to produce a pinched high density - high temperature plasma which is a source of high energy beams of electrons and ions, soft and hard X-rays, and fusion neutrons (if deuterium or deuterium - tritium gas mixture is used as working gas) [Ste04], the first step is to form the current sheath (CS) across the insulator surface and to accelerate the CS down the discharge tube followed by radial compression to produce the pinch.

Filippov and Mather type plasma focus devices are generally used plasma focus geometries as design concepts with some differences. For example, while the radial compression phase starts after the axial (run-down) phase in Mather's type, it starts with the formation of the CS in Filippov's type PF. The spherical plasma focus (SPF) has different features compared with Mather and Filippov type PF devices due to geometrical configuration. In the spherical plasma focus device while the CS is accelerated with the CS expansion in the rundown phase I (phase I), it is compressed in both radial and axial directions in the rundown phase II (phase II) and the reflected shock phase (phase III).

The symmetric umbrella-like shape of the CS is produced by the gas discharge between the electrodes across the insulator surface. The increasing current density J, which is flowing through the electrodes (from inner electrode to outer electrode) and the CS, creates an azimuthal magnetic field B which results in the CS lift off from the insulator. Radially flowing current J_r and induced azimuthal magnetic field B_ϕ produces a $J \times B$ force. The $J \times B$ force accelerates the CS in the direction shown in Fig. 3.1 with an angle θ towards the first equator point and then the other antipodal point [M. 10].

Since magnetic field is changing during the CS motion and the CS is supersonic, an ionizing shock wave (shock front) ionizes the undisturbed gas ahead of the shock wave. This produced shock front collects the ionized gas particles like a solid magnetic piston with some mass efficiency factor f_m.

A plasma layer is assumed to exist between the current sheath and the shock front, which is called the slug, and the gas inside the slug is assumed to be homogeneous and ionized. Plasma slug temperature is calculated with the help of the shock front velocity by considering uniform pressure between the magnetic piston and the shock front.

After the CS reaches the equator point which has the lowest magnetic field and the lowest magnetic pressure, the magnetic field and magnetic pressure start to increase which results in accelerating the CS towards the axis. Since the shock front is formed in front of the CS and has higher speed, the shock front reaches the axis and reflects back towards the CS. When the reflected shock front hits the CS, the CS continues to move towards the axis. Thereafter, the current sheath collapses on the axis and

forms the pinch (small dense plasma) which has a high temperature and high energy density.

3.1.1 Rundown Phase I

The rundown phase I will start immediately after the gas breakdown. The snowplow model with the shock wave equations is used to calculate the plasma and shock parameters in this phase. It is assumed that the CS moves perpendicular to the direction of the acceleration. The equations used for plasma sheath motion in the rundown phase I are the momentum, magnetic force, and the circuit equations.

3.1.1.1 Insulator Volume Calculation

Since the insulator has considerable effect on plasma parameters, its volume should be taken into account.

$$V_{ins} = \int_0^{2\pi} d\phi \int_a^b r^2 dr \int_0^{\theta_0} sin\theta_0 d\theta = \frac{2\pi}{3}(b^3 - a^3)(1 - cos\theta_0) \tag{3.5}$$

where V_{ins} is the insulator volume corresponding to the angle θ_0, ϕ is the azimuthal angle, r is the radial distance at which the plasma parameters are calculated. θ is the polar angle, which is a function of the discharge time t, b and a are the outer and inner electrode radii, respectively.

3.1.1.2 Effective Volume Calculation

Since the CS sweeps all the gas in front of it, the volume at which point the plasma sheath reaches should be considered for mass calculation in order to get the correct plasma sheath parameters. Therefore, the volume at which plasma sheath parameters are calculated is:

$$V_{eff} = \int_0^{2\pi} d\phi \int_a^b r^2 dr \int_0^{\theta} sin\theta d\theta - V_{ins} \tag{3.6}$$

$$V_{eff} = \frac{2\pi}{3}(b^3 - a^3)(1 - cos\theta) - V_{ins} \tag{3.7}$$

Then

$$V_{eff} = \frac{2\pi}{3}(b^3 - a^3)(cos\theta_0 - cos\theta) \tag{3.8}$$

The present study assumes that there is no effect for the insulator since its dimension is too small as compared to the whole sphere, hence the motion is considered to start at angle theta which is very small and close to zero. The variation of θ in the rundown phase I is from the beginning of the current sheath motion until the CS reaches the equator point.

3.1.1.3 Momentum Equation

Since the flowing current J and induced magnetic field B produces the $J \times B$ force which acts on the current sheath as magnetic force P_B, then the rate of momentum change of the CS can be determined by the magnetic force. The force due to the rate of momentum change of the CS in the rundown phase I is:

$$F_1 = \frac{d(m v_\theta)}{d t} \tag{3.9}$$

where tangential velocity v_θ is

$$v_\theta = r \dot{\theta} \tag{3.10}$$

and the mass of the plasma sheath m is

$$m = \rho f_m \frac{2\pi}{3}(b^3 - a^3)(cos\theta_0 - cos\theta) \tag{3.11}$$

Therefore, the force due to the rate of momentum change of the CS in this phase is

$$F_1 = \rho f_m \frac{2\pi}{3}(b^3 - a^3) r[sin\theta \dot{\theta}^2 + (cos\theta_0 - cos\theta)\ddot{\theta}] \tag{3.12}$$

where ρ is the initial gas density, and f_m is the fraction of mass swept up by the sheath motion.

The magnetic force F_2 on the current sheath can be determined from the magnetic pressure P_B

$$F_2 = \int_a^b P_B dA = \int_a^b \frac{B^2}{2\mu_0} dA \tag{3.13}$$

where

$$B = \frac{\mu_0 I f_c}{2\pi r sin\theta} \tag{3.14}$$

is the magnetic field at distance r due to the current I flowing in the CS with the f_c current fraction that accounts for the current shedding effect, μ_0 is permeability of free space, and $dA = 2\pi r sin\theta dr$ is the small area of the sheath over which the magnetic field is calculated, then,

$$F_2 = \frac{\mu_0 I^2 f_c^2}{4\pi sin\theta} ln(\frac{b}{a}) \tag{3.15}$$

Since the rate of momentum change of the CS is equal to the magnetic force on the current sheath, F_1 is set equal to F_2, and it is solved for $\ddot{\theta}$ to find the equation of motion in the rundown phase I:

$$\ddot{\theta} = \frac{\alpha^2 I^2}{r sin\theta (cos\theta_0 - cos\theta)} - \frac{\dot{\theta}^2 sin\theta}{cos\theta_0 - cos\theta} \tag{3.16}$$

where α is the scaling parameter which is given by

$$\alpha^2 = \frac{3\mu_0 f_c^2 ln(b/a)}{8\pi^2 \rho f_m (b^3 - a^3)} \tag{3.17}$$

The sheath velocity is obtained by integrating the acceleration equation (eq. 3.16) then the sheath position is obtained by integration of the velocity.

3.1.1.4 Plasma Inductance

Since the inductance (or electric inductance) is defined as a measure of the amount of magnetic flux produced for a given electric current, the magnetic flux and the plasma inductance can be calculated as follows:

$$\phi_B = \int_a^b B\,dA = \int_a^b \frac{\mu_0 I f_c}{2\pi r\,sin\theta} r(\theta - \theta_0) dr \tag{3.18}$$

where ϕ_B is the magnetic flux, and $dA = \ell\,dr = r(\theta - \theta_0)dr$ is the area over which the inductance is calculated, ℓ is the arch length at which point the inductance is calculated. The plasma inductance is given by

$$L = \frac{\phi_B}{I f_c} = \int_a^b \frac{\mu_0}{2\pi r\,sin\theta} r(\theta - \theta_0) dr \tag{3.19}$$

$$L = \frac{\mu_0 (b-a)}{2\pi} \frac{(\theta - \theta_0)}{sin\theta} \tag{3.20}$$

The plasma inductance can be written in terms of the scaling parameter β as follows:

$$L = \frac{\beta(\theta - \theta_0)}{f_c \, sin\theta} \tag{3.21}$$

where

$$\beta = \frac{\mu_0 (b-a) f_c}{2\pi} \tag{3.22}$$

and the inductance derivative is

$$\frac{dL}{dt} = \frac{\beta \dot{\theta}}{f_c \, sin\theta}[1 - (\theta - \theta_0) cot\theta] \tag{3.23}$$

3.1.1.5 Discharge Current

General assumption is to ignore the plasma resistance $r(t)$ when calculating the circuit equation. The current can be calculated by using Kirchhoff's Law according to figure 3.1b:

$$\frac{d}{dt}[(L_0 + L f_c) I] + r_0 I = V_0 - \int \frac{I \, dt}{C_0} \tag{3.24}$$

$$(L_0 + L f_c)\frac{dI}{dt} + I f_c \frac{dL}{dt} + r_0 I = V_0 - \int \frac{I \, dt}{C_0} \tag{3.25}$$

Then,

$$\frac{dI}{dt} = \frac{V_0 - \int \frac{I\,dt}{C_0} - r_0 I - I f_c \frac{dL}{dt}}{L_0 + L f_c} \tag{3.26}$$

3.1.1.6 Discharge Voltage

The discharge voltage for spherical plasma focus (SPF) device can be obtained from the inductive equation:

$$V = \frac{d}{dt}[LIf_c] = f_c I \frac{dL}{dt} + f_c L \frac{dI}{dt} \tag{3.27}$$

3.1.1.7 Shock Velocity

While the CS and shock front (constituting plasma slug together) moves from the first antipodal point to the other antipodal point, the plasma slug collects all the gas encountered by the shock front which is assumed to be thin. Therefore, the planar shock-jump equations can be used across the shock front to calculate the shock velocity, which is used to calculate the plasma temperature. Assuming that the shock pressure P_s is uniform across the slug, the shock pressure can be set equal to the magnetic pressure P_B at the magnetic piston to calculate the shock velocity v_s.

Shock pressure P_s can be written as follows:

$$P_s = \frac{2}{\gamma+1}\rho f_m v_s^2 \tag{3.28}$$

where γ is the specific heat ratio, v_s is the shock velocity.

The magnetic pressure for the rundown phase I is given by

$$P_B = \frac{\mu_0 I^2 f_c^2}{8\pi^2 r^2 sin^2\theta} \tag{3.29}$$

Therefore, the shock velocity is given by

$$v_s = \frac{dr_s}{dt} = -\frac{I f_c}{4\pi r sin\theta}\sqrt{\frac{\mu_0(\gamma+1)}{\rho f_m}} \tag{3.30}$$

where the minus sign represents the motion in the opposite direction.

3.1.1.8 Plasma Temperature

The plasma temperature can be calculated using the shock velocity for the rundown phases I and II, and the reflected shock phase [M. 10; S. 85]:

$$T = \frac{M}{R_0}\frac{2(\gamma-1)}{(\gamma+1)^2}\frac{v_s^2}{(1+Z_{eff})D_N} \tag{3.31}$$

where M is the molecular weight of the filling gas, R_0 is the universal gas constant, γ is specific heat ratio, Z_{eff} is the effective charge of the plasma, and D_N is dissociation number.

3.1.1.9 Plasma Energy and Power Consideration

In the plasma focus system, all the energy comes from the capacitor energy bank E_{tot} which is distributed into the system. The total energy E_{tot} and total power P_{tot} can be calculated as follows:

$$E_{tot} = \frac{1}{2} C_0 V_0^2 \tag{3.32}$$

$$P_{tot} = I_0 V_0 \tag{3.33}$$

where

$$I_0 = V_0 \sqrt{C_0 / L_0} \tag{3.34}$$

The deposited energy into the plasma sheath E_p and the power deposited into tube P_{tube} are calculated as follows:

$$E_p = \int I f_c V \, dt \tag{3.35}$$

$$P_{tube} = I V \tag{3.36}$$

3.1.2 Rundown Phase II

The rundown phase II starts when the current sheath reaches the equator point, and it ends when the shock front hits the axis. As in the rundown phase I, the snowplow model with the shock wave equations are used together with necessary modifications for rundown phase II. The same assumptions and set of governing equations are used in this phase to calculate the plasma and shock parameters. Effective volume, discharge current, and discharge voltage calculations are the same as in the rundown phase I. The equations used for plasma sheath motion in the rundown phase II are the momentum, magnetic force and the circuit equations.

3.1.2.1 Effective Volume Calculation

The volume at which plasma sheath parameters are calculated is:

$$V_{eff} = \int_0^{2\pi} d\phi \int_a^b r^2 dr \int_0^{\theta} sin\theta d\theta - V_{ins} \tag{3.37}$$

$$V_{eff} = \frac{2\pi}{3}(b^3 - a^3)(1 - cos\theta) - V_{ins} \tag{3.38}$$

Then

$$V_{eff} = \frac{2\pi}{3}(b^3 - a^3)(Cos\theta_0 - Cos\theta) \tag{3.39}$$

The range of θ in the rundown phase II starts when the CS reaches the equator point until the shock front reaches the axis.

3.1.2.2 Momentum Equation

The rate of momentum change of the CS is equal to the magnetic force on the current sheath. Therefore, it can be determined by the magnetic force on the CS. In the rundown phase II, the magnetic field, which is used for the rundown phase II and the reflected shock phase, is calculated as follows:

$$B = \frac{\mu_0 I f_c}{2\pi r cos(\theta - \pi/2)} \tag{3.40}$$

The force due to the rate of momentum change of the CS in the rundown phase II is

$$F_1 = \frac{d(m v_\theta)}{d t} \tag{3.41}$$

$$F_1 = \rho f_m \frac{2\pi}{3}(b^3 - a^3) r [sin\theta \dot{\theta}^2 + (cos\theta_0 - cos\theta)\ddot{\theta}] \tag{3.42}$$

The magnetic force F_2 on the current sheath for the rundown phase II can be determined from the magnetic pressure P_B

$$F_2 = \int_a^b P_B dA = \int_a^b \frac{B^2}{2\mu_0} dA \tag{3.43}$$

where $dA = 2\pi r cos(\theta - \pi/2) dr$

Then,

$$F_2 = \frac{\mu_0 I^2 f_c^2}{4\pi cos(\theta - \pi/2)} ln(\frac{b}{a}) \tag{3.44}$$

Since the rate of momentum change of the CS is equal to the magnetic force on the current sheath, F_1 is set equal to F_2, and it is solved for $\ddot{\theta}$ to find the equation of motion in the rundown phase II:

$$\ddot{\theta} = \frac{\alpha^2 I^2}{r cos(\theta - \pi/2)(cos\theta_0 - cos\theta)} - \frac{sin\theta \dot{\theta}^2}{cos\theta_0 - cos\theta} \tag{3.45}$$

where the scaling parameter α in the rundown phase II is the same as the scaling parameter in the rundown phase I.

3.1.2.3 Plasma Inductance

Since the magnetic field equation in this phase is calculated as in eq. 3.40, the magnetic flux, plasma inductance, and the derivative of the plasma inductance are calculated as follows:

$$\phi_B = \int_a^b B\,dA = \int_a^b \frac{\mu_0 I f_c}{2\pi r\,cos(\theta-\pi/2)} r(\theta-\theta_0)\,dr \tag{3.46}$$

$$L = \frac{\phi_B}{I f_c} = \frac{\mu_0(b-a)}{2\pi}\frac{(\theta-\theta_0)}{cos(\theta-\pi/2)} \tag{3.47}$$

The plasma inductance can also be written in terms of the scaling parameter β as follows:

$$L = \frac{\beta(\theta-\theta_0)}{f_c\,cos(\theta-\pi/2)} \tag{3.48}$$

The inductance derivative is then

$$\frac{dL}{dt} = \frac{\beta\dot{\theta}}{f_c\,cos(\theta-\pi/2)}[1+(\theta-\theta_0)tan(\theta-\pi/2)] \tag{3.49}$$

3.1.2.4 Discharge Current

The current for the rundown phase II can also be calculated by using Kirchhoff's Law according to figure 3.1b:

$$\frac{d}{dt}[(L_0+Lf_c)I] + r_0 I = V_0 - \int \frac{I\,dt}{C_0} \tag{3.50}$$

$$(L_0+Lf_c)\frac{dI}{dt} + I f_c \frac{dL}{dt} + r_0 I = V_0 - \int \frac{I\,dt}{C_0} \tag{3.51}$$

Then,

$$\frac{dI}{dt} = \frac{V_0 - \int \frac{I\,dt}{C_0} - r_0 I - I f_c \frac{dL}{dt}}{L_0 + L f_c} \tag{3.52}$$

3.1.2.5 Discharge Voltage

The discharge voltage for the spherical plasma focus (SPF) device can also be obtained from the inductive equation for the rundown phase II:

$$V = \frac{d}{dt}[L I f_c] = f_c I \frac{dL}{dt} + f_c L \frac{dI}{dt} \tag{3.53}$$

3.1.2.6 Shock Velocity

The planar shock-jump equations can be used across the shock front with the assumption of the uniform shock pressure P_s to calculate the shock velocity v_s, which is used to calculate the plasma temperature. Since it is assumed that the shock pressure P_s is uniform across the slug, the shock pressure can be set equal to the magnetic pressure P_B at the magnetic piston to calculate the shock velocity in the rundown phase II as well.

Shock pressure for the rundown phase II is

$$P_s = \frac{2}{\gamma + 1} \rho f_m v_s^2 \tag{3.54}$$

Magnetic pressure for the rundown phase II is

$$P_B = \frac{B^2}{2\mu_0} = \frac{\mu_0 I^2 f_c^2}{8\pi^2 r^2 cos^2(\theta - \pi/2)} \tag{3.55}$$

The shock velocity v_s for the rundown phase II is then written as:

$$v_s = \frac{dr_s}{dt} = -\frac{I f_c}{4\pi r cos(\theta - \pi/2)} \sqrt{\frac{\mu_0(\gamma+1)}{\rho f_m}} \tag{3.56}$$

3.1.3 Reflected Shock Phase

The reflected shock phase starts after the shock front hits the axis, and reflects back towards the CS. It ends when the shock front hits the CS. In this phase the distance between the CS and the shock front starts decreasing as opposed to the rundown phases I and II until the shock front meets the CS. The constant shock front velocity is used in this phase, which is 0.3 times the shock front velocity on the axis when the shock front hits the axis [Lee14]. The same snowplow model and the shock wave equations with the constant shock front velocity are used in this phase. Therefore, the governing equations are the same as in the rundown phase II with the constant reflected shock front velocity, which is given by:

$$v_s = 0.3(v_s)_{on-axis} \tag{3.57}$$

where $(v_s)_{on-axis}$ represents the velocity of the shock front when the shock front hits the axis at the end of the rundown phase II [Sia05].

3.2 Results and Discussion

An experiment with the spherical plasma focus chamber was conducted to measure the neutron emission [Zav13]. The data of this experiment with the SPF chamber are used for comparison and validation in this study.

3.2.1 Model Validation

To validate the SPF model, it will be compared with the results of the experiment of a spherical plasma focus chamber [Zav13]. In this study, the plasma focus consists of 2 concentric electrodes, with inner and outer electrode radii of 8 and 14.5 cm, respectively. The capacitor bank, charging voltage, external inductance and the equal amount of DT mixture filling gas pressure are 432 μF, 25 kV, 36 nH, and 14.5 $Torr$, respectively. The resistance is used to control the value of the current peak, but it usually has small values and has lower effect as compared to the other parameters like the inductance and could be neglected in some cases. In this study, the best value of the resistance r_0 is 3.2 $m\Omega$.

These parameters are used for all the designed experiments except that the filling gas pressure and discharge voltage are arranged to observe their effects on the plasma temperature and the pinch start time with different gases.

Since the discharge current has significant effect on the plasma dynamic, electrodynamic, thermodynamic, and radiation processes in the plasma focus devices [SSH10], the current wave form and its derivative are used to validate the model as compared with published experimental results [Zav13].

Fig. 3.2 shows the calculated (SPF) and measured total discharge currents (Exp), and Fig. 3.3 shows the corresponding current derivatives for a DT mixture. The used mass fraction f_m is 0.11, and the current fraction f_c is 0.68. The current fraction f_c is calculated with the help of the published calculation method [Saw10] as 0.66 and adjusted to 0.68 for better match between experimentally measured discharge current and the calculated discharge current for model validation as follows:

$$I_{peak} = \frac{2\pi C_0 V_0}{\tau} \tag{3.58}$$

$$f_c = \frac{I_{exp}}{I_{peak}} \tag{3.59}$$

where I_{peak} and I_{exp} are the theoretical and experimental peak discharge current, and τ is the discharge time period [Saw10].

The theoretical calculations have good agreement with the experimental results for both the discharge currents and the current derivatives. The smaller sharp value in the model prediction of the current derivative is mainly due to the use of constant mass fraction f_m and current fraction f_c in the model for all the phases, while they could be variable in the experiment for each small time interval. Another possible

reason may be attributed to the gas breakdown before the CS starts moving, which has considerable effect on the discharge current. The current sheet motion in the experiment starts after the gas breakdown, while this time delay in the current sheet motion in the model is not taken into account, which results in a slight difference between the model and the experimental results [Sia05].

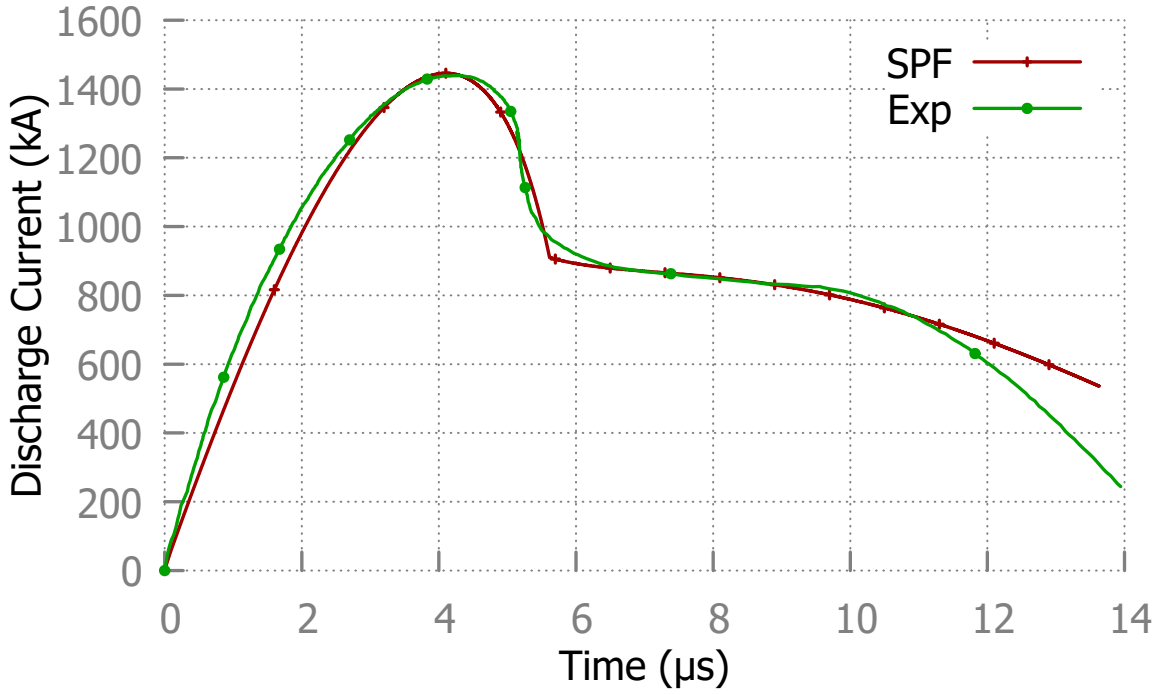

Figure 3.2 Calculated and measured total discharge current for DT mixture

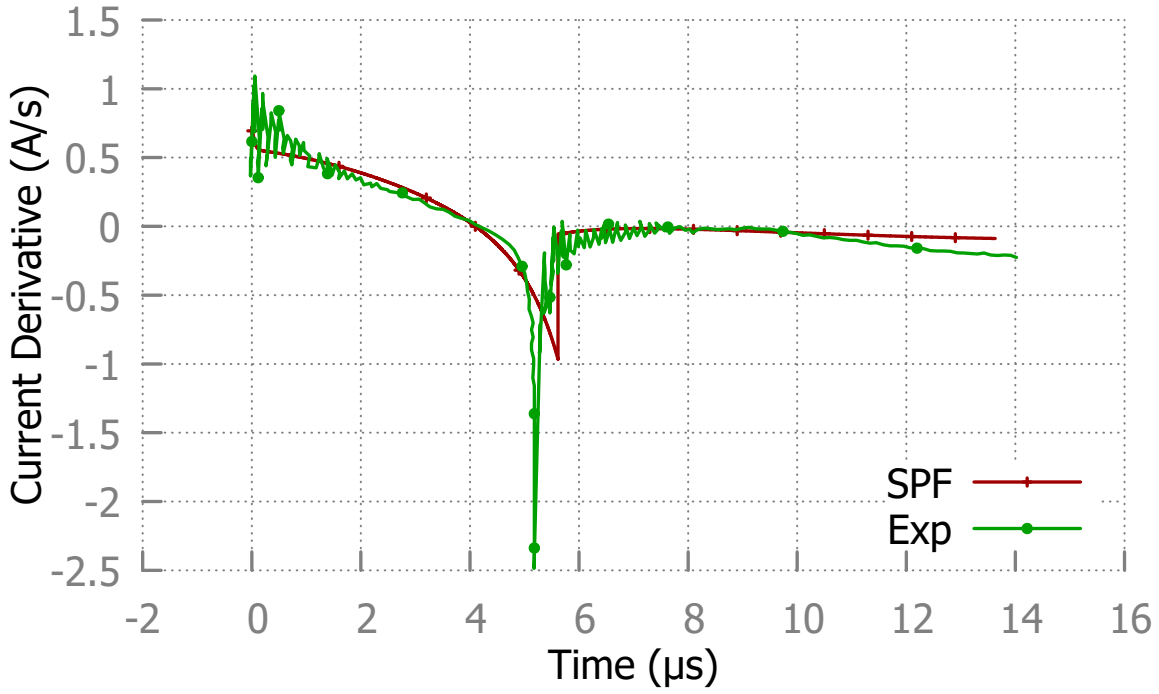

Figure 3.3 Current derivatives corresponding to the discharge currents in figure 3.2 for DT mixture

3.2.2 Plasma Parameters for DT Mixture

Fig. 3.4 shows the discharge voltage of the SPF. The sharper the voltage spike, the deeper the discharge current dip, the better the focus in the plasma focus devices [Hos11; FS12]. Therefore, the sharp voltage spike at 5.6 μs with the maximum discharge voltage of 43.7 kV in Fig. 3.4 and the discharge current dip of 910 kA from the maximum discharge current of 1446 kA in Fig. 3.2 are indications for a good focus in the SPF.

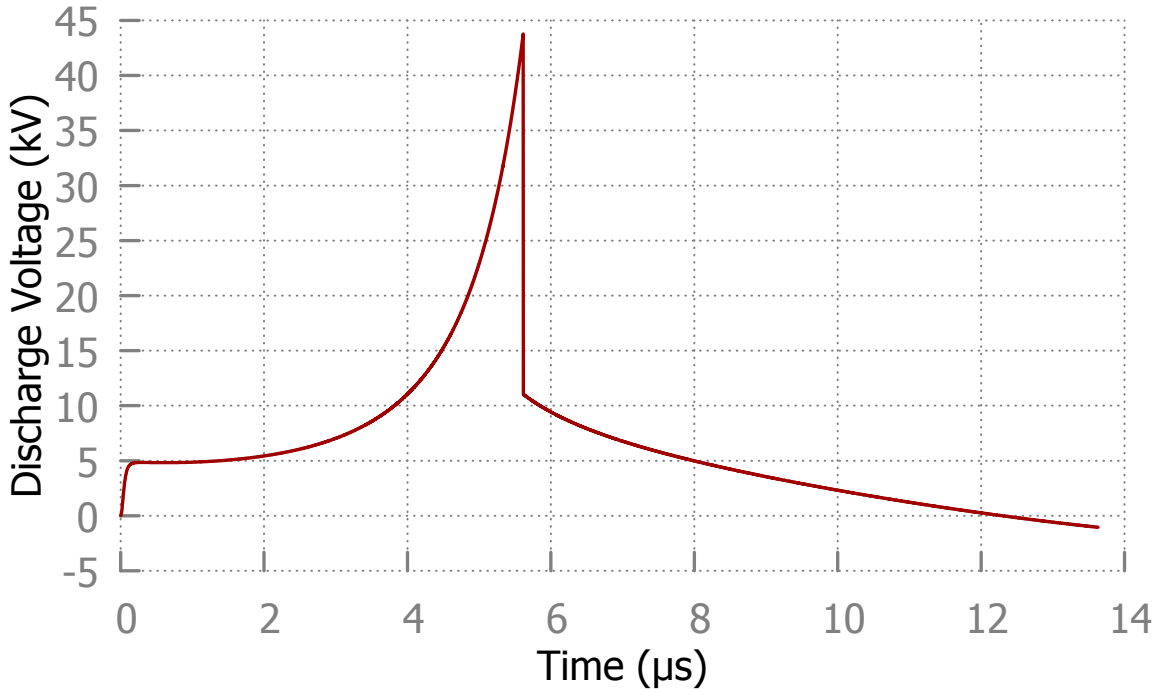

Figure 3.4 Discharge voltage for DT mixture

Fig. 3.5 shows the displacement of the plasma (the CS) and the shock front from the axis. Since the geometry is spherical, both the CS and shock front displacements are increasing from the first antipodal point until the equator point of the spherical shape. While the shock front reaches the maximum displacement at 1.84 μs, it takes 3.4 μs for the CS. Slug thickness also increases due to higher speed of the shock front. Since the distance from the axis are decreasing from the equator point to the other antipodal point, and both the CS and shock front moves along the axis, the displacements start decreasing with increasing slug thickness. The shock front moves with higher speed, and it reaches the axis at 3.5 μs then reflects back towards the CS by decreasing the slug thickness while the CS still moves towards the axis with decreasing displacement. The CS and reflected shock meets at 41.7 mm away from the axis at 5.3 μs.

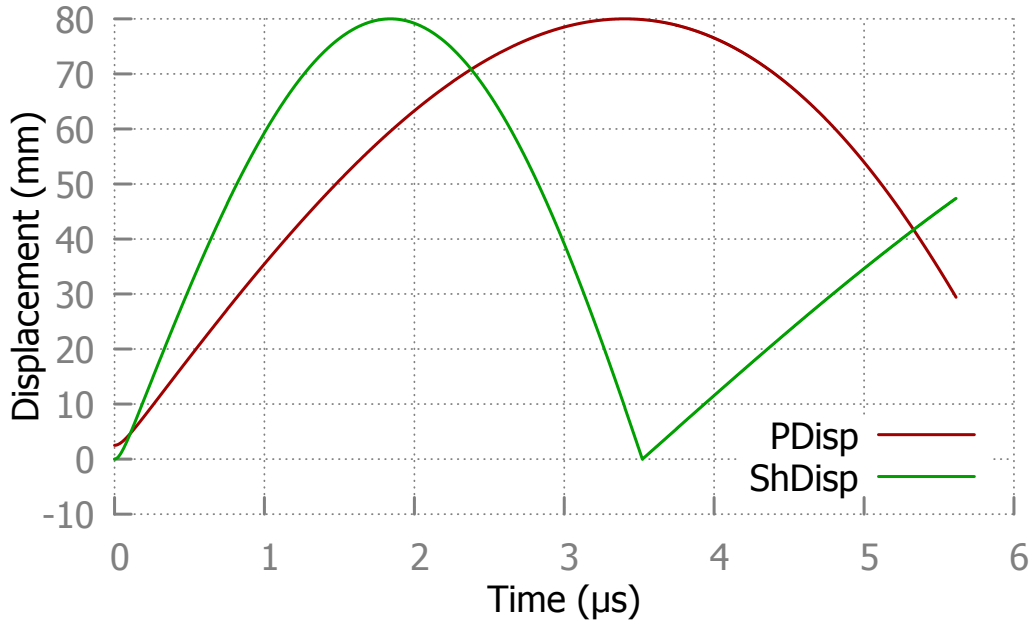

Figure 3.5 Plasma and shock front displacements for DT mixture

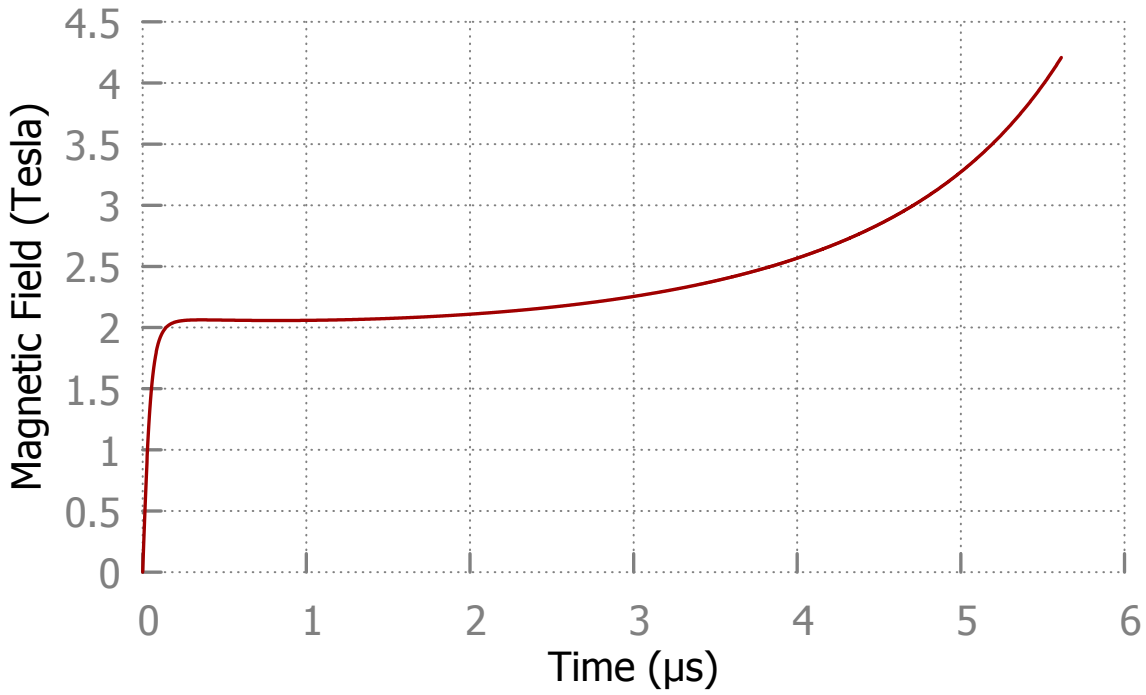

Figure 3.6 Magnetic field for DT mixture

Figure 3.6 shows the induced magnetic field due to the flowing current I, as previously expressed by the set of equations, in which the magnetic field depends on the current and the distance of the current sheath from the axis. It roughly depends on the ratio of I/r where r is the distance from the axis for the current sheath, and I is the discharge current.

Since both the discharge current and the distance from the axis are increasing, and the ratio of I/r stays almost the same, the magnetic field does not change much from the beginning to 3.5 μs of the motion which is the time when the shock front hits the axis and reflects back towards the current sheath. It also corresponds to both

the close-to-maximum discharge current value and the time when the current sheath just passes the equator point of the sphere which is the end of the rundown phase I. After the rundown phase I is completed, the magnetic field starts increasing until the point where the current sheath and the reflected shock front meets.

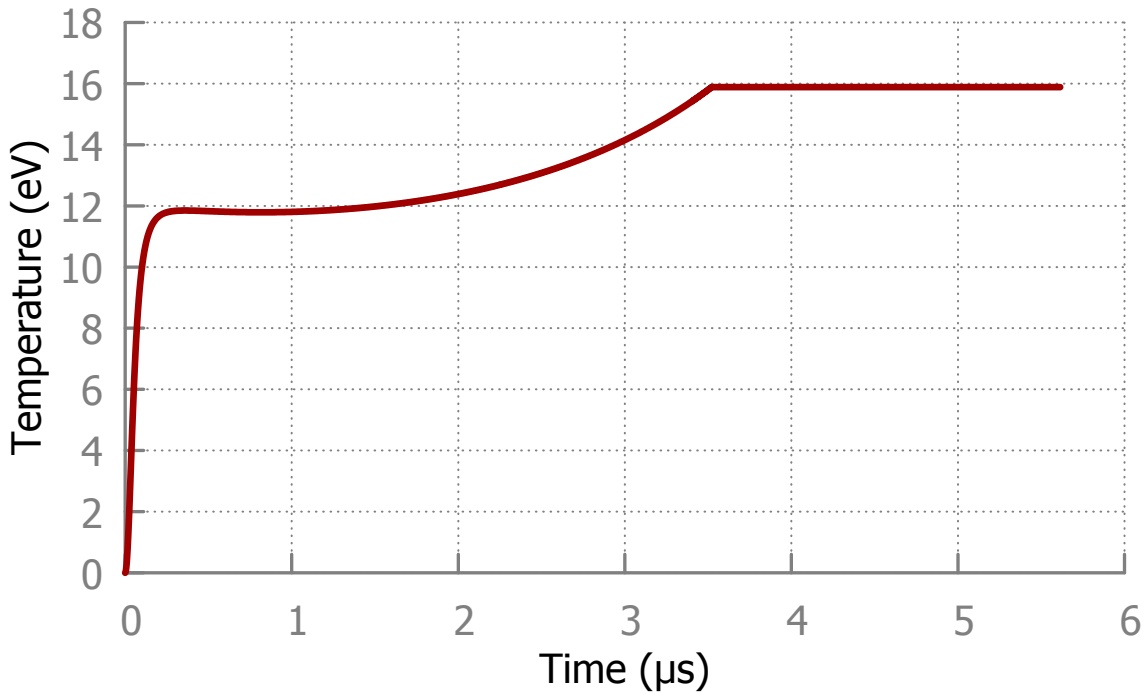

Figure 3.7 Plasma temperature for DT mixture

Figure 3.7 shows the plasma temperature during the motion, Fig. 3.8 shows the velocity of the CS, and Fig. 3.9 shows the velocity of the shock front and the reflected shock front (RShock).

The shock velocity starts increasing as shown in Figure 3.9 in the beginning of the

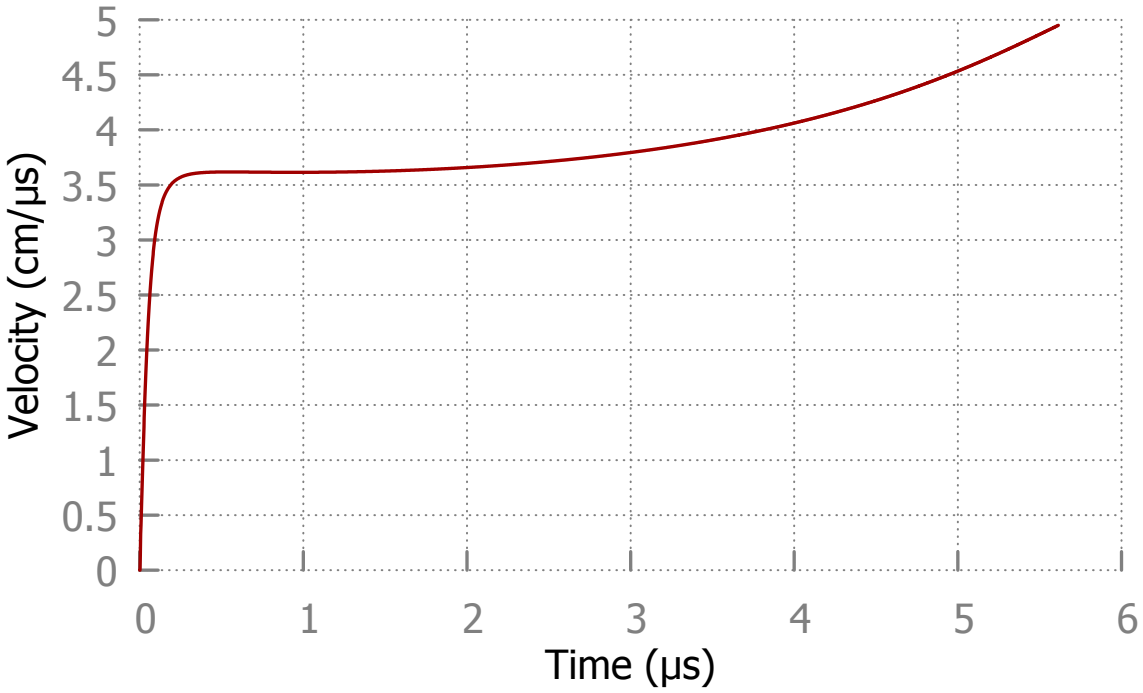

Figure 3.8 Plasma velocity for DT mixture

motion. Therefore, plasma temperature starts increasing until the shock front hits the axis and reflects back towards the current sheath. After this point, there is a plateau in the plasma temperature which is due to the assumed constant reflected shock front velocity as seen in the figure 3.9.

The current sheath velocity is increasing until the current sheath hits the reflected shock front, and a constant reflected shock front velocity is assumed after the shock front hits the axis. While the plasma velocity follows the same trajectory as magnetic field because magnetic field drives the plasma slug, the shock velocity follows the same trajectory as the plasma temperature because shock front increases the plasma temperature by ionizing the gases in front of the plasma slug.

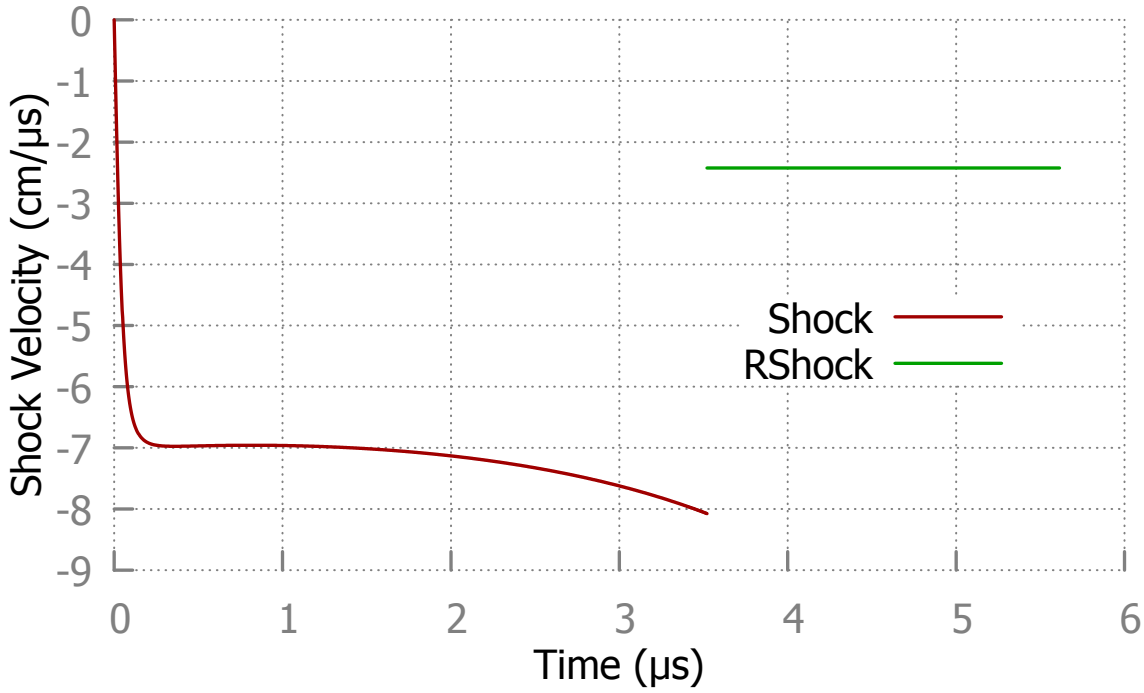

Figure 3.9 Shock front velocities for DT mixture

Figure 3.10 shows the energy deposited into the plasma sheath normalized to total energy (E_p/E_{tot}) and the power deposited into the tube normalized to total power (P_{tube}/P_{tot}).

The total energy E_{tot} from the equation 3.32 and the total power P_{tot} from the equation 3.33 are calculated as 135 kJ and 68.46 GW. While the maximum deposited energy into the plasma sheath at the end of the motion is about 54 kJ which is equal to approximately 40 % of the total energy, the maximum deposited power into the tube at 5.6 μs is 39.84 GW which is 58% of the total power as in figure 3.10.

Since 39.84 GW is 58 % of the total power deposited into tube, multiplying 0.58 by f_c factor of 0.68 results in 39.44% which is approximately the same as the deposited

energy into the plasma. Therefore, it can be deduced that 39.44% of the total power, which is 27 GW, can be deposited into the plasma. The point where E_p starts saturating and P_{tube} reaches the maximum value occur at 5.6 μs.

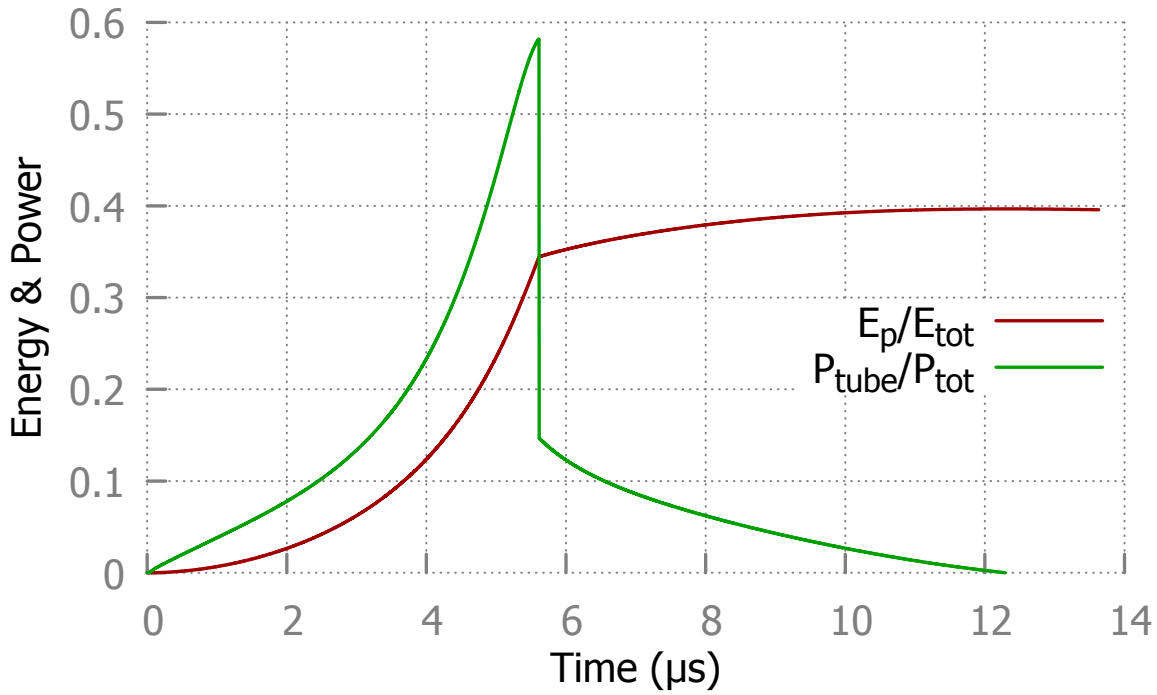

Figure 3.10 Tube Power and Plasma Sheath Energy

3.2.3 Pressure and Voltage Sweep

Fig. 3.11 shows the variation of the maximum temperature (HTemp, DTemp, TTemp) and the pinch start time (HTime, DTime, TTime) as a function of the gas pressure for hydrogen, deuterium and tritium, respectively. In addition to 0.5 $Torr$ of gas pressure, the gas pressure is incremented by 1 $Torr$ for each run from 1 $Torr$ until 25 $Torr$, and the corresponding maximum temperature and pinch start time are plotted in figure 3.11.

While maximum temperature is decreasing with increasing gas pressure, the pinch start time is increasing with increasing gas pressure. Tritium as the heaviest gas of these three gases has the highest temperature and the longest pinch start time, which shows that temperature and pinch start time are increasing with increasing gas molecular weight.

The discharge voltage range is between 10 and 100 kV as shown in Fig. 3.12 with the corresponding maximum temperature and pinch start time for hydrogen, deuterium and tritium. Increasing the discharge voltage results in increasing the maximum temperature, and decreasing the pinch start time for all three gases. Tritium as the heaviest gas of these 3 gases achieves the highest temperature with the longest pinch start time with respect to discharge voltage, thus indicating the effect of increasing gas molecular weight.

As seen from Figures 3.11 and 3.12, the maximum temperature can be obtained with a relatively shorter pinch start time by using a relatively heavier gas with lower gas pressure and higher discharge voltage.

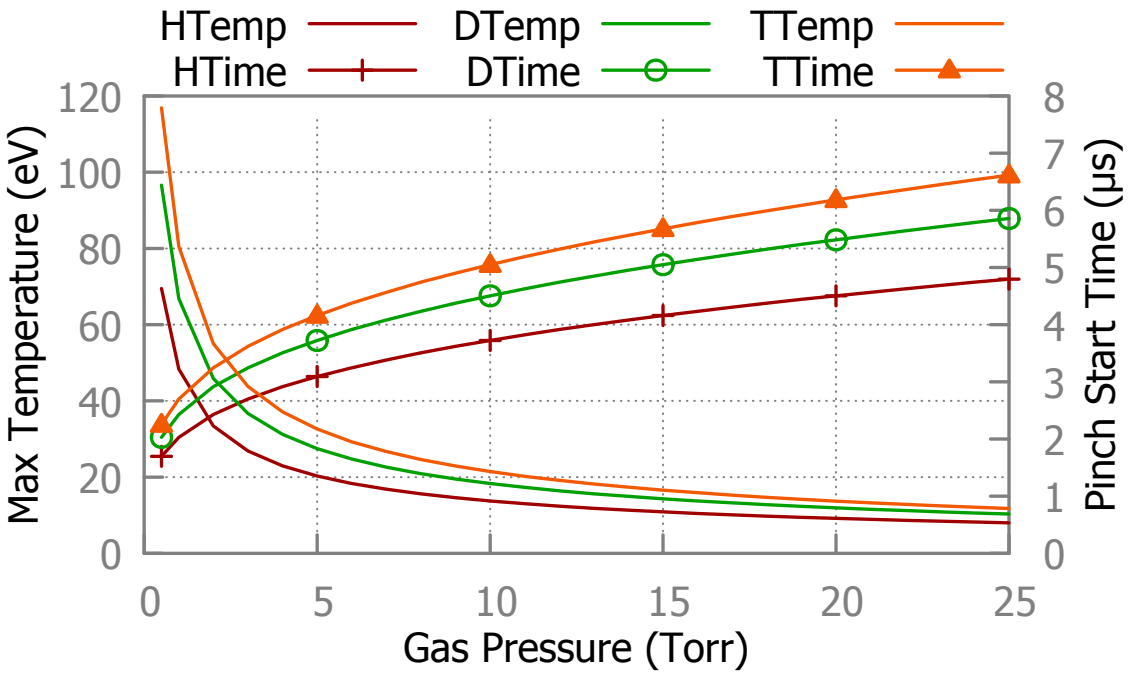

Figure 3.11 Max temperature and pinch start time for H,D and T with respect to filling gas pressure

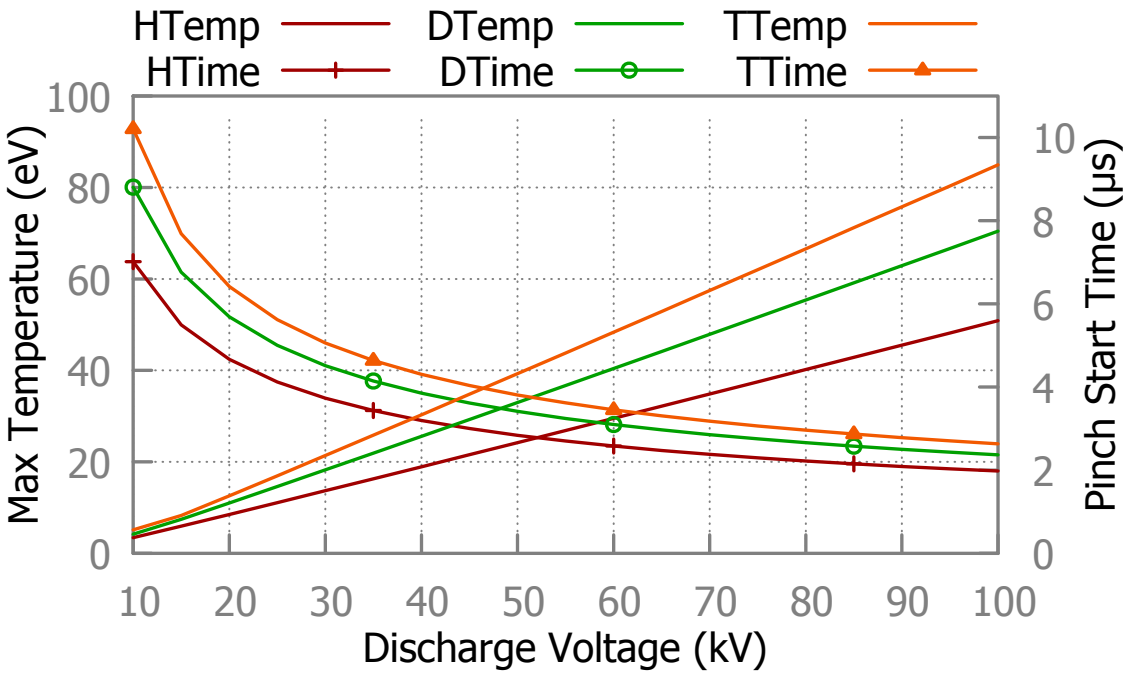

Figure 3.12 Max temperature and pinch start time for H,D and T with respect to discharge voltage

3.2.4 Plasma Parameters for Hydrogen, Deuterium and Tritium SPF

The variations of the discharge current and discharge voltage with respect to time for hydrogen, deuterium, and tritium are shown in figures 3.13 and 3.14, respectively for charging voltage of 25 kV.

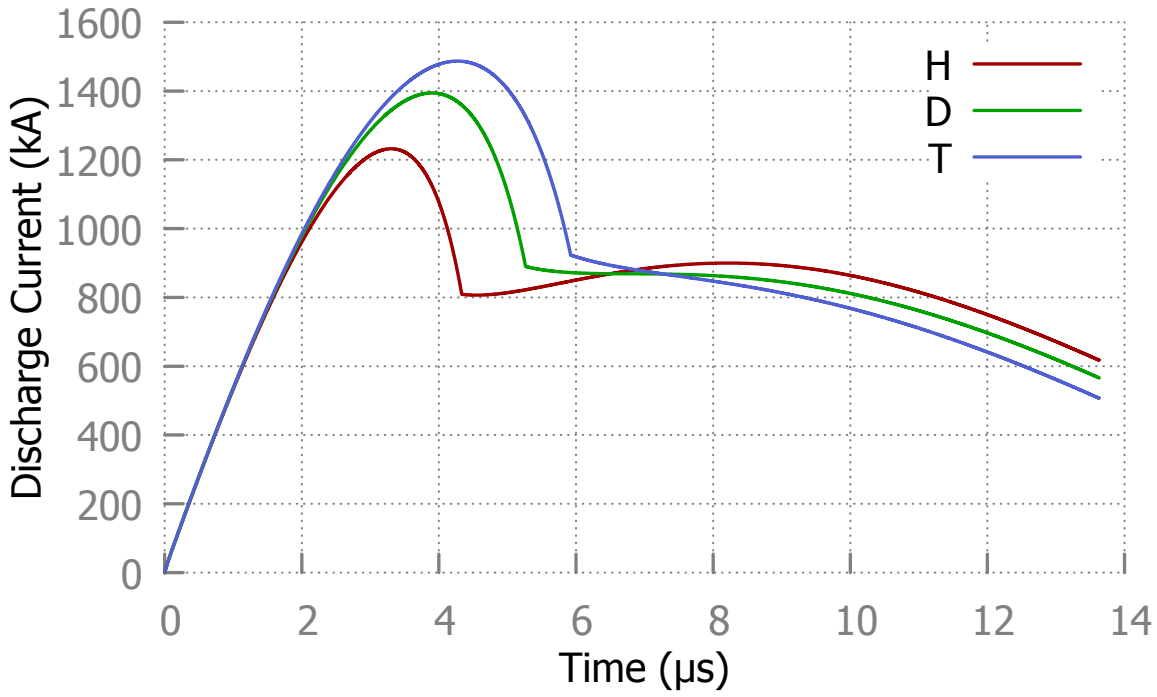

Figure 3.13 Discharge currents for H,D and T

Peak Discharge Current (MA)	1.232	1.394	1.487
Dip Discharge Current (kA)	809	890	923

Table 3.1 Peak and dip discharge currents

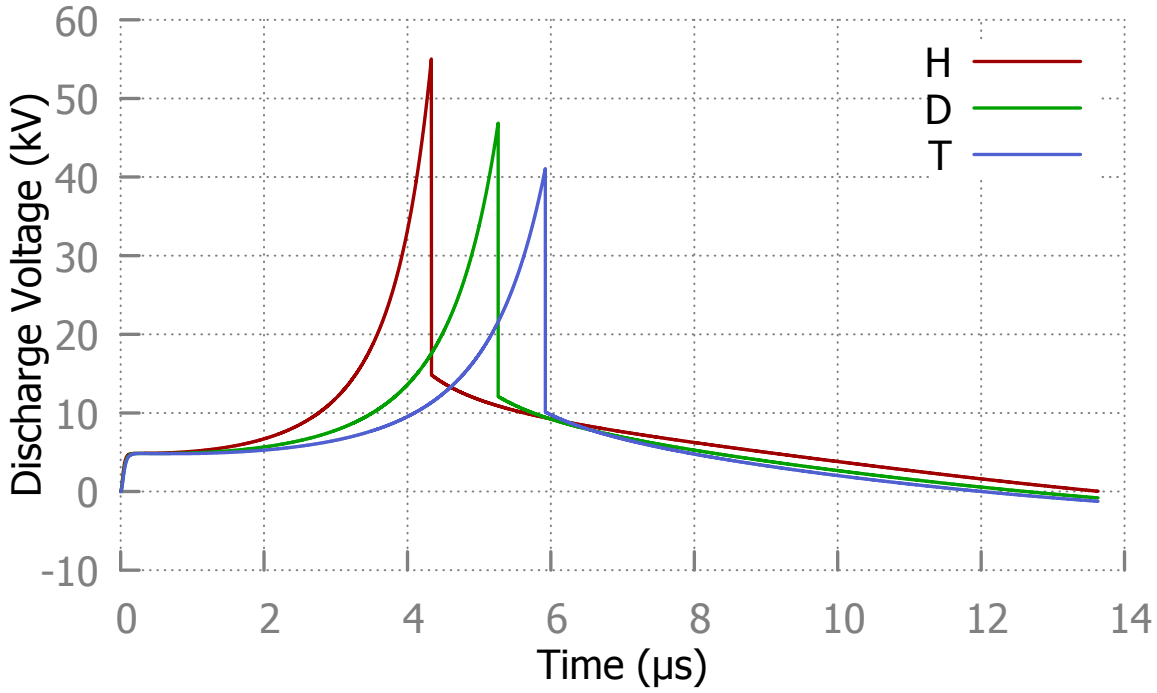

Figure 3.14 Discharge voltages for H,D and T

As can be seen from Fig. 3.13 and Table 3.1, the peak discharge currents are 1.232 MA at 3.304 μs for hydrogen, 1.394 MA at 3.897 μs for deuterium, and 1.487 MA at 4.271 μs for tritium. Dip discharge currents are 809 kA at 4.333 μs for hydrogen, 890 kA at 5.264 μs for deuterium, and 923 kA at 5.922 μs for tritium.

Dip discharge currents occur at the same time with the peak discharge voltage (figure 3.14). The peak discharge voltages are 55 kV at 4.333 μs for hydrogen, 46.85 kV at 5.264 μs for deuterium, and 41 kV at 5.922 μs for tritium.

As the molecular weight of the gas increases, the peak discharge current also increases, but peak discharge voltage decreases. Since deeper discharge current and sharper discharge voltage result in better focus in the dense plasma focus devices

[Hos11; FS12], then a better focus can be achieved by using hydrogen which is the lightest gas as compared to deuterium and tritium for the same conditions in the sense that hydrogen has the deepest discharge current dip and the highest discharge voltage spike.

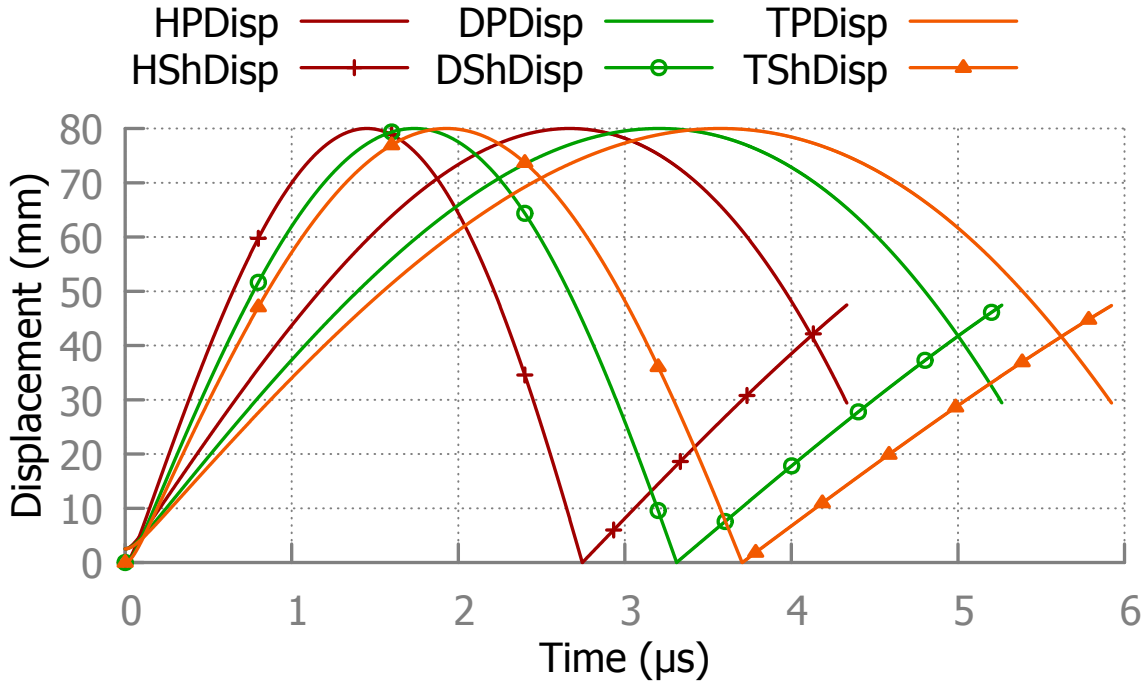

Figure 3.15 Plasma and shock front displacements for H,D and T

The displacement of the CS and shock front are shown in Fig. 3.15 for hydrogen, deuterium, and tritium. HPDisp, DPDisp, and TPDisp represent plasma displacement (or the CS displacement), for hydrogen, deuterium, and tritium, respectively. HShDisp, DShDisp, and TShDisp represent the shock front displacement for the corresponding

gases.

In case of hydrogen, while shock front reaches the equator point at 1.45 μs, it takes 2.67 μs for the CS. For deuterium, the time to reach the equator point is 1.73 μs for the shock front and 3.2 μs for the CS. For tritium, it takes 1.93 μs for the shock front to move from the beginning to the end of the half sphere as the CS reaches this point at 3.57 μs.

As the molecular weight of the gas is increased, the time from the beginning to the point where the current sheath and shock front meets is also increased as well as the time to reach the equator point for the current sheath and shock front, and the time to hit the axis for the shock front.

The effect of the molecular weight of the gas on the plasma velocity and temperature can be seen in figures 3.16 and 3.17 as well. While tritium as the heaviest gas achieves the highest temperature and the lowest velocity, hydrogen as the lightest gas achieves the lowest temperature and the highest velocity. Interesting point about the current sheath and the shock front displacement is the time it takes to reach the equator point for the current sheath and the shock front, and the time it takes to reach the axis for the shock front when molecular weight of the gas is increased.

The current sheath and the shock front hit each other approximately at the same distance from the axis for hydrogen, deuterium, and tritium as well as for DT mixture. The distances from the axis are 41.7 mm for hydrogen, deuterium, tritium, and DT mixture.

Fig. 3.18 shows the magnetic field due to the current flow. Since magnetic field follows the plasma velocity, and the rate of change in the plasma velocity is increasing

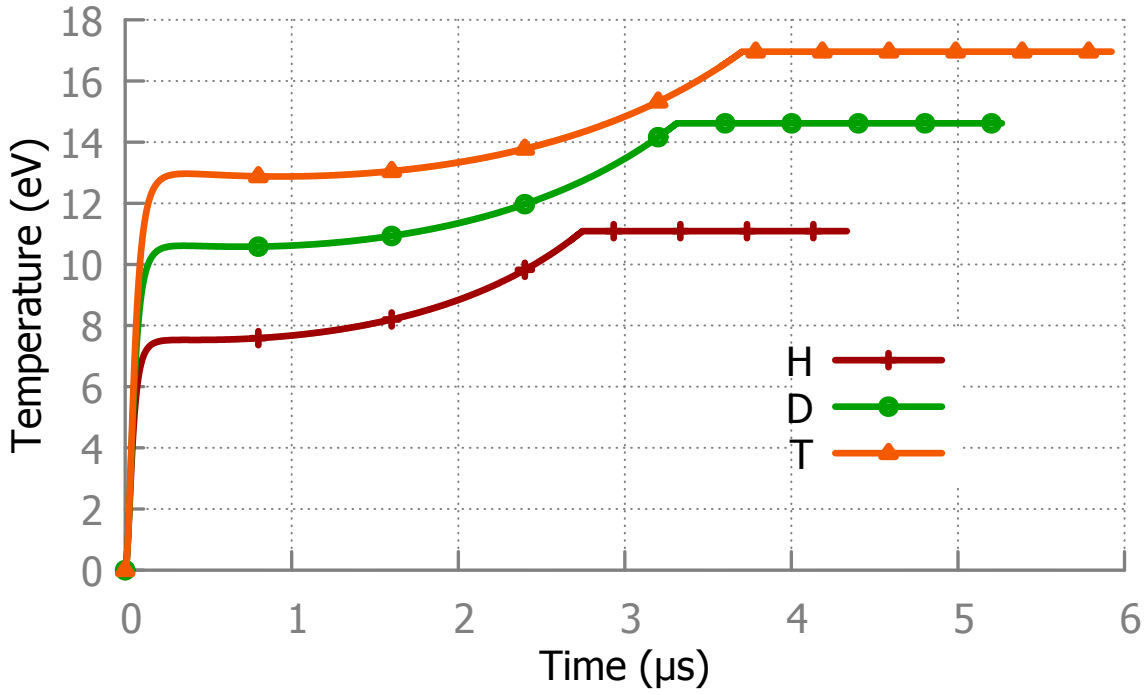

Figure 3.16 Plasma temperature for H,D and T

after the CS finishes the rundown phase I, the magnetic fields for each gases also increases after this point where the CS reaches the equator point of the spherical plasma focus.

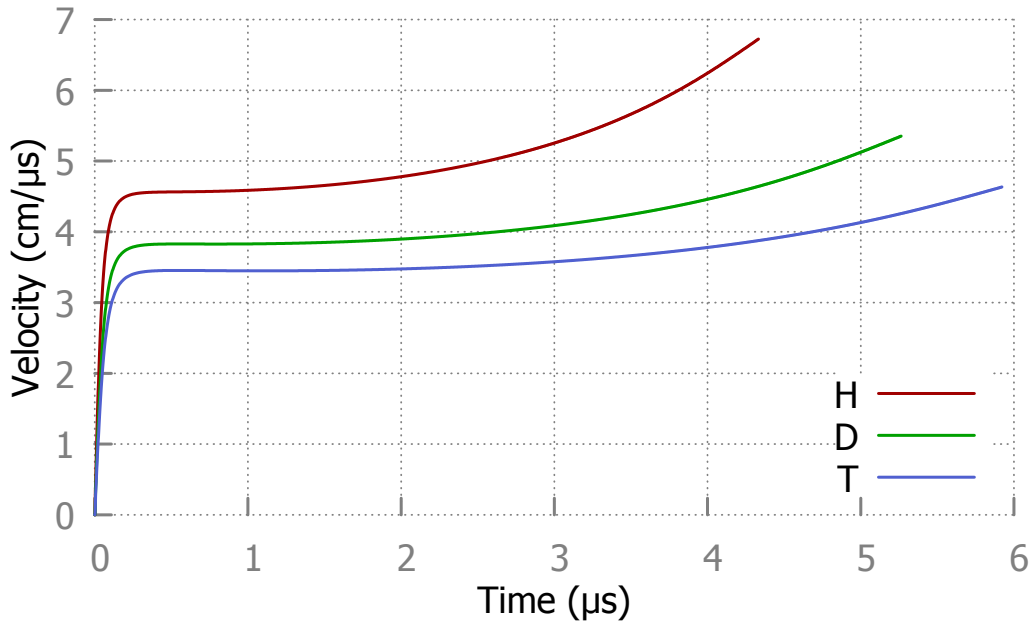

Figure 3.17 Plasma velocities for H,D and T

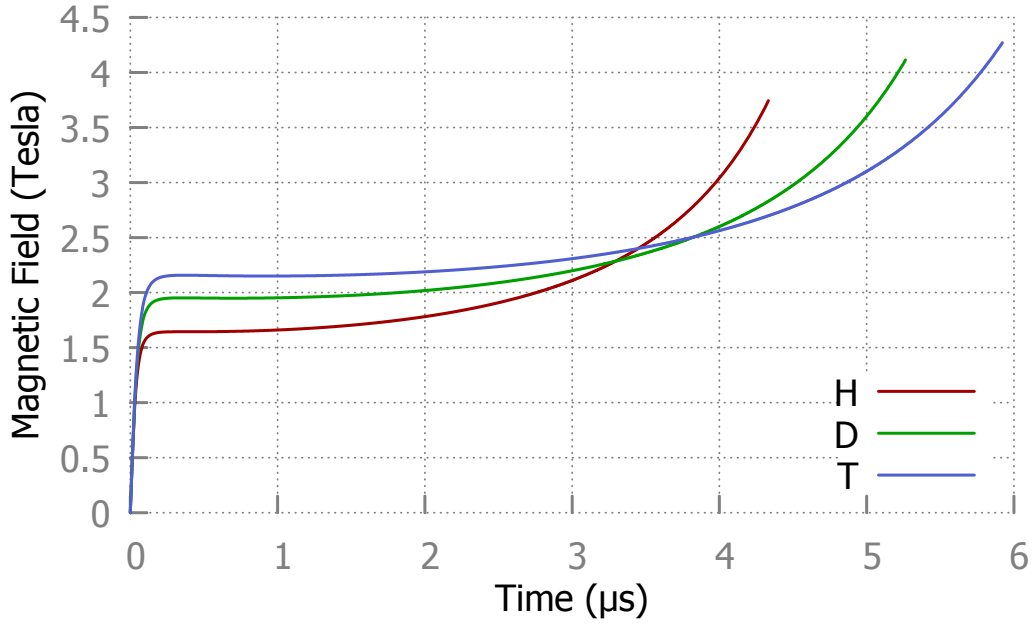

Figure 3.18 Magnetic fields for H,D and T

3.3 Conclusions

The snow plow model, shock wave equations, and equivalent circuit model for dense plasma focus device were used in this study to develop a simulation regime of a spherical plasma focus (SPF) device with two concentric spheres. The model provides results including plasma parameters for hydrogen, deuterium, and tritium comparable to published experimental data. The simulation determined the effect of the variation of the gas pressure, discharge voltage, and the gas molecular weight on the plasma temperature and pinch start time as well as the effect of the gas molecular weight on the plasma parameters.

The spherical plasma focus model results showed good agreement with the experimental data for the discharge current and its derivative, with good accuracy, which are the main indicators to show how well the plasma focus model compares well to the experiment.

In order to obtain the plasma and shock wave parameters with respect to the molecular mass of the gas, discharge voltage, and the gas pressure in the spherical plasma focus device, several computational runs were completed for hydrogen, deuterium, tritium, and deuterium-tritium gas mixture by varying the filling gas type, filling gas pressure, and discharge voltage.

While the maximum discharge current achieved is 1.487 MA with tritium, the maximum voltage peak and the deepest discharge current dip are 55 kV and 809 kA respectively with hydrogen which makes hydrogen a better candidate, compared to deuterium and tritium, to have a good focus in dense plasma focus devices. An

interesting finding is the point where the CS and reflected shock front meets as displacement in that the CS and reflected shock front meets at approximately the same distance from the axis for all the cases.

The obtained temperature variation in terms of the gas pressure and discharge voltage with different gas types suggests that the maximum plasma temperature can be achieved with a heavier gas by using low filling gas pressure and high discharge voltage.

After the reflected shock front hits the CS at the end of the reflected shock phase, the radiative phase starts. The effect of the radiation emission will be discussed in the next chapter. The radiation emission can result in energy gain with the joule heating and energy losses with the bremsstrahlung, radiative recombination, and line radiation, which also affects the plasma temperature. Maximum deposited energy into the plasma sheath E_p and the maximum deposited power into the tube are around 40 % of the total energy E_{tot} and 58 % of the total power, respectively.

CHAPTER

4

RADIATION EFFECT AND BEAM-ION PROPERTIES IN THE SPHERICAL PLASMA FOCUS

4.1 Introduction

Neutron production with deuterium or the mixture of deuterium-tritium filling gas via nuclear fusion reactions is one of the main reasons that the plasma focus (PF) devices are studied with its cost and energy efficiency. There are two widely accepted neutron production mechanisms in the plasma focus devices, which are the thermonuclear neutron production mechanism and the beam-target neutron production mechanism [Cas00].

While thermonuclear neutrons are produced in the thermal equilibrium in the pinch phase (or called radiative phase or slow compression phase) due to the interaction of the thermal deuterons at the maximum compression [TSK09], the beam-target neutrons are produced in the so-called virtual diode model by the accelerated energetic ions hitting the relatively stationary plasma target (thermal deuterons) or ambient gas outside the plasma under the diode voltage [Gri07a], which occurs after maximum compression of the pinch.

The dominant neutron production mechanisms for the plasma focus devices can be determined by the neutron anisotropy measurement, which is the neutron flux ratio in the axial direction to the radial direction with respect to the anode axis [TSK09], which also emphasizes that non-thermal beam-target neutron production mechanism has an important role in fusion reactions because while neutron anisotropy is an evidence of preferred direction for deuteron motion in the plasma focus devices, there is no preferred neutron emission direction in the thermal neutron production mechanism.

Two main reasons for neutron anistropy are 1) the velocity direction differences between the center of mass and the laboratory frame of references of the colliding deuterons, 2) the center of mass frame of reference differential cross section for the nuclear fusion reaction $D + D \rightarrow {}^{3}He + n$ which are discussed in detail in the work of F. Castillo et al [Cas00].

On the one hand neutron production, which strongly depends on the filling gas pressure, by taking into account the neutron anistropy and the effect of the pressure regime on the thermal neutron yield [TSK09] with respect to the bank energy of the plasma focus device was studied with the conclusion of stronger dependency between the plasma focus bank energy and thermonuclear neutrons [TK09], on the other hand the dominant non-thermal beam-target neutron yield [Kub06] and the ion beam-plasma interaction were also investigated [Gri07a] which was concluded that the target plasma was hot and the ion-ion collisions (head-on and coulomb collisions) were responsible for neutron production in the plasma focus device. Another important point of the plasma focus devices is the energy transformation which has strong relation with the neutron yield. The energy transformation was investigated considering the parameters which affect the energy transformation efficiency in the plasma column [Kub12a].

The relation between neutron angular distribution and the neutron yield with respect to filling gas pressure showed that the beam-target neutron yield mechanism is more dominant in higher pressure [Bag11b], which is also the case in this study with 14.5 $Torr$ filling gas pressure of deuterium-tritium mixture and 25 kV charging voltage.

Since the developed model for the spherical plasma focus (SPF), which consists of a rundown phase I, a rundown phase II, and a reflected shock phase, was explained in detail in chapter 3 until the reflected shock front hits the current sheath, which is the starting point for the radiative phase (pinch phase or slow compression phase), the neutron yield and radiation losses with the ion properties in the spherical plasma focus device are the main objectives in this chapter.

In the previous chapter shock wave equations and snowplow model coupled with the circuit equations were used to model the phases of the two concentric electrodes spherical plasma focus device. Plasma parameters were investigated as well as the effect of the variation in the gas pressure and discharge voltage for hydrogen and its isotopes.

The configuration of the spherical plasma focus device and the equivalent circuit model can be seen in figure 4.1 which shows the inner and outer electrodes, the insulator and the current sheath (CS) as the spherical plasma focus device configuration in figure 4.1a, and the circuit inductance L_0, the resistance r_0, the capacitor bank C_0, the insulator resistance r_{ins}, and the closing switch as the equivalent circuit model in figure 4.1b.

The initial conditions, model and machine parameters, assumptions, the calculations for the current sheath, shock front and circuit parameters, and the method to solve the equations are explained in the previous chapter. The neutron yield, radiation effect, and ion properties are investigated for the radiative phase of the spherical plasma focus in this chapter.

4.2 Theory of the SPF : Radiative Phase

In order to produce a pinched high density-high temperature plasma, the current sheath is formed as the first step by gas discharge between the electrodes across the insulator surface and is accelerated down the discharge tube (rundown phase I), followed by radial compression (rundown phase II), and after the shock front hits the axis, it reflects back towards the current sheath (reflected shock phase), to produce the pinch (radiative phase).

Rundown phase I starts with the creation of the CS and ends at the equator point which is the starting point for rundown phase II until the shock front hits the axis. Reflected shock phase starts after the shock front reflects from the axis and ends at the point where the CS and the reflected shock front meet which is the beginning of the radiative phase.

In the radiative phase, the change in the current sheath dynamics results in temporal changes of the plasma inductance of the pinch column, which stores the plasma energy, and discharge currents as well as the large induced electric fields which eventually lead to plasma disruption [LS13]. Plasma disruption results in the emission of electromagnetic radiation, electrons and ions from the focus region in addition to the generated high voltage in the pinch producing a beam of fast ions by diode action in a thin layer close to the anode [Gri07a].

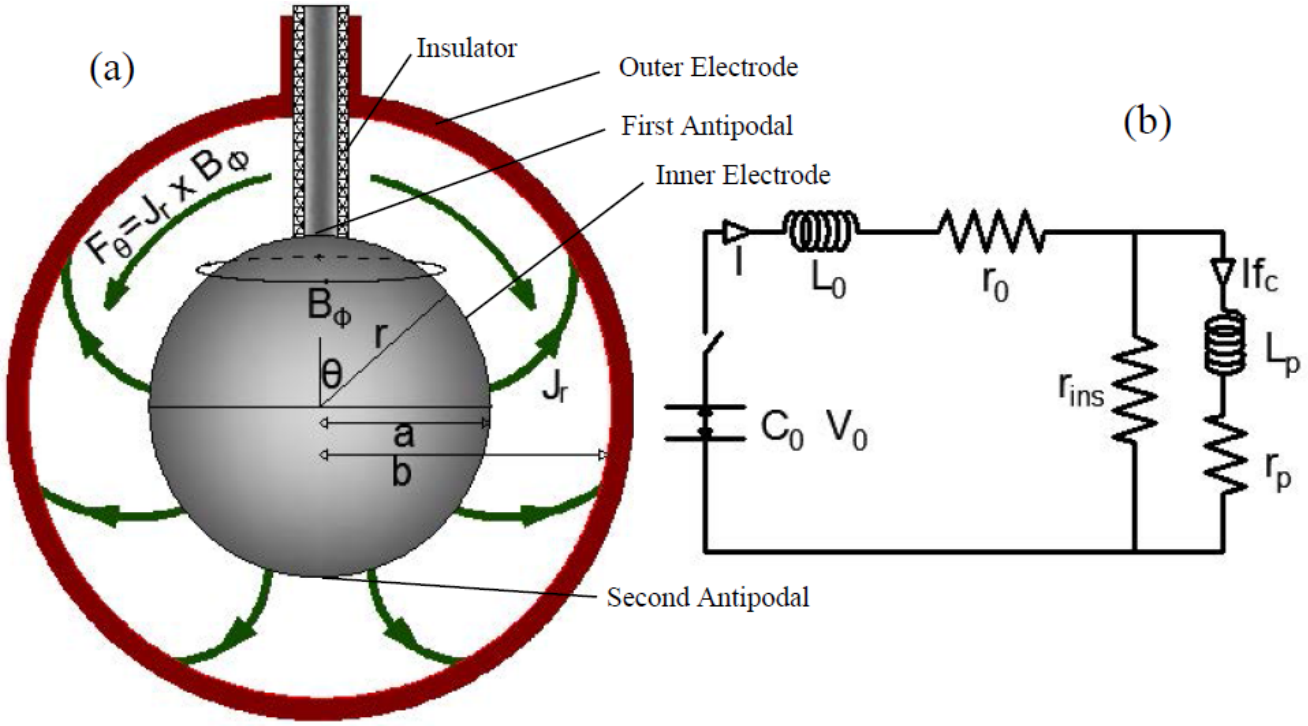

Figure 4.1 (a) Spherical plasma focus configuration. (b) Equivalent circuit model of the SPF

4.2.1 Equation of Motion

In the rundown phase I, II and the reflected shock phase, the momentum change rate F_1 is due to the magnetic force F_2 on the current sheath (CS). Therefore, F_1 is set equal to F_2 and solved for the equation of the motion for these phases.
F_1 and F_2 are given as follows:

$$F_1 = \frac{d(m v_\theta)}{d t} \tag{4.1}$$

where v_θ is tangential velocity, and m is the mass of the plasma sheath

$$F_2 = \int_a^b P_B dA = \int_a^b \frac{B^2}{2\mu_0} dA \tag{4.2}$$

where B is the magnetic field at the distance r due to the current I flowing in the CS, P_B is the magnetic pressure, μ_0 is permeability of free space, and $dA = 2\pi r sin\theta dr$ is the small area of the sheath.

Setting F_1 equal to F_2 and solving for $\ddot{\theta}$ in the rundown phase I, II and reflected shock phases gives the following equation of motions for these phases.

Equation of motion for rundown phase I:

$$\ddot{\theta} = \frac{\alpha^2 I^2}{r sin\theta (cos\theta_0 - cos\theta)} - \frac{\dot{\theta}^2 sin\theta}{cos\theta_0 - cos\theta} \tag{4.3}$$

Equation of motion for rundown phase II and reflected shock phase:

$$\ddot{\theta} = \frac{\alpha^2 I^2}{r\,cos(\theta - \pi/2)(cos\theta_0 - cos\theta)} - \frac{\dot{\theta}^2 sin\theta}{cos\theta_0 - cos\theta} \tag{4.4}$$

where α is the scaling parameter which is given by

$$\alpha^2 = \frac{3\mu_0 f_c^2 ln(b/a)}{8\pi^2 \rho f_m (b^3 - a^3)} \tag{4.5}$$

where f_c and f_m are the current fraction that accounts for the current shedding and mass fraction swept up by the sheath motion. a and b are the inner and outer electrode radii. ρ is the initial gas density. θ_0 and θ are the angles corresponding to the insulator volume and the polar angle, respectively.

After the reflected shock front hits the current sheath, the radiation phase starts. Plasma column still continues to compress until the plasma disruption occurs at the maximum compression in this phase [Gri07a]. While the ions flow in one direction, which results in the beam-target neutron production, the electrons flow in the other direction, which results in the hard x-ray production [Cas00; Gri07b; Kub06], due to the generated high voltage from the plasma disruption which causes radiation emissions [Gri07b; Gri07a; TK09].

The main considerable effects on the current sheath due to the radiations are the effect of bremsstrahlung radiation, line radiation and radiative recombination. These radiations which are considered as energy loss terms and Joule heating which is

considered as an energy gain term in terms of the plasma energy may be formulated for hydrogen-like plasmas as follows [Hub09; GR95; Spi62]:

Bremsstrahlung Radiation:

$$P_{BR} = 1.625 \times 10^{-38} N_e N_i Z^2 T_{eV}^{1/2} \tag{4.6}$$

Spectral Line Radiation:

$$P_{LN} = 8 \times 10^{-35} N_e N_i Z^6 T_{keV}^{3/2} \tag{4.7}$$

Radiative Recombination:

$$P_{REC} = 6 \times 10^{-40} N_e N_i Z^4 T_{keV}^{1/2} \tag{4.8}$$

Joule Heating:

$$P_J = R I^2 f_c^2 \tag{4.9}$$

where P_{BR}, P_{LN} and P_{REC} are power densities in W/m^3 for bremsstrahlung radiation, line radiation, and radiative recombination. P_J is joule heating. N_e and N_i are electron and ion densities in m^{-3}. T_{eV} is electron temperature in eV, T_{keV} is electron temperature in keV, and Z is charge state which is also equal to atomic number for fully ionized hydrogen-like gases. R is the plasma resistance in Ω, which is calculated from Spitzer resistivity ρ_{res} [Spi62; Hub09] as follows:

$$R = \frac{\rho_{res} \times L_{col}}{A_{col}} \tag{4.10}$$

$$\rho_{res} = 1.03 \times 10^{-2} Z \, ln\Lambda T_{eV}^{-3/2} \tag{4.11}$$

where L_{col} is the plasma column length, $A_{col} = 2\pi a^2(1 - cos\theta)$ is the cross sectional area of the plasma column, and $ln\Lambda$ is Coulomb logarithm [Hub09].

The curved current sheath in the figure 4.1a was assumed to be straight. Therefore, the plasma resistance is

$$R = 1290 \frac{Z}{T^{3/2}} \frac{(b-a)/ab}{2\pi[1 - cos(\pi - \theta)]} \tag{4.12}$$

where T is the plasma temperature in Kelvin using Bennett equilibrium as calculated in the previous chapter.

Total power density and energy density of the plasma column during radiative phase can be calculated as follows:

$$P = P_J - P_{BR} - P_{LN} - P_{REC} \tag{4.13}$$

$$Q = Pt \tag{4.14}$$

where P is the total plasma power density, Q is the total plasma energy density during radiative phase, and t is pinch duration.

There are three main forces which affect the motion of the plasma sheath in the plasma focus device. These are as follows:

Force due to the momentum change:

$$F_1 = \rho f_m \frac{2\pi}{3}(b^3 - a^3) r[sin\theta\dot{\theta}^2 + (cos\theta_0 - cos\theta)\ddot{\theta}] \tag{4.15}$$

Force due to the magnetic pressure:

$$F_2 = \frac{\mu_0 I^2 f_c^2}{4\pi cos(\theta - \pi/2)} ln(\frac{b}{a}) \tag{4.16}$$

Force due to Joule heating and radiation emissions:

$$F_3 = QA \tag{4.17}$$

$$A = 2\pi b^2[1 - sin(\theta - \pi/2)] + (\pi b^2 - \pi a^2)cos(\theta - \pi/2) - \pi a^2 \tag{4.18}$$

where A is the surface area of the plasma column in the pinch phase. The current sheath is assumed to be straight in the pinch phase as in the other phases.

Since the joule heating are the energy gain term, and radiation terms are the energy loss terms for the plasma, the change rate of momentum F_1 is equal to the difference between the force due to the magnetic pressure F_2 and the force due to the joule

heating and radiation emission F_3 as follows:

$$F_1 = F_2 - F_3 \tag{4.19}$$

Therefore, the equation of motion $\ddot{\theta}$ for the radiative phase of the plasma focus device can be calculated as follows:

$$\ddot{\theta} = \frac{\alpha^2 I^2}{r\,cos(\theta - \pi/2)C} - \frac{sin\theta\dot{\theta}^2}{C} - \frac{3QA}{2\pi\rho f_m(b^3 - a^3)rC} \tag{4.20}$$

where

$$C = cos\theta_0 - cos\theta \tag{4.21}$$

and

$$\alpha^2 = \frac{3\mu_0 f_c^2\ ln(b/a)}{8\pi^2\rho f_m(b^3 - a^3)} \tag{4.22}$$

The first two terms in eq. 4.20 are the same as in the previous chapter for the equation of motion but the third term, which is coming from the Q value, is taking into account the joule heating and radiation terms.

4.2.2 Neutron Yield

The main neutron production mechanism is the beam - target neutron yield in the spherical plasma focus device with deuterium - tritium mixture (1:1) filling gas. Diode voltage, which results from the plasma disruption, accelerates the beam of ions which is produced by diode action in the radiative phase of the plasma focus device [Gri07a]. The ions interact with the hot plasma column to produce neutrons from the fusion reactions.

The neutron yield from fusion reaction is given as:

$$Y = n_b n_i V_{col} \sigma v_b \tag{4.23}$$

where n_b is the beam ion number density per m^3, n_i is the plasma ion number density per m^3, V_{col} is the volume for the plasma focus pinch column, σ is the cross section for deuterium - tritium reactions, and v_b is the effective speed of the beam ions in m/s.

The beam ion number density, n_b, is calculated as the total number of beam ions N_b divided by the volume of the plasma focus pinch column V_{col}.

$$n_b = \frac{N_b}{V_{col}} \tag{4.24}$$

The beam ion number density can also be calculated by considering the kinetic energy of the beam ions (E_{kb}) and pinch inductive energy (E_{ip}). Pinch inductive energy is converted by a fraction of f_e to the total beam kinetic energy which is the

collection of kinetic energies from each beam ion in the plasma focus.

Since each beam ion has a mass $M m_p$ and speed v_b, the total beam kinetic energy can be calculated as follows [LS13]:

$$E_{kb} = \frac{1}{2} N_b M m_p v_b^2 \tag{4.25}$$

where N_b is the total number of beam ions, M is the mass number of the ion, and m_p is the mass of the proton in kg.

Beam-ion energy in Joule:

$$E_{ion} = \frac{1}{2} M m_p v_b^2 \tag{4.26}$$

Pinch inductive energy can be calculated as [LS13]:

$$E_{ip} = \frac{1}{2} L I_{pinch}^2 \tag{4.27}$$

$$E_{ip} = \frac{1}{2} L I^2 f_c^2 \tag{4.28}$$

where L is the inductance of the focus pinch and $I_{pinch} = I f_c$ is the current flowing through the pinch.

Since pinch inductive energy is converted to the beam kinetic energy by the fraction of f_e, it can be written as follows:

$$E_{kb} = f_e \times E_{ip} \tag{4.29}$$

$$\frac{1}{2} N_b M m_p v_b^2 = f_e \frac{1}{2} L I^2 f_c^2 \tag{4.30}$$

Then

$$N_b = \frac{f_e L I^2 f_c^2}{M m_p v_b^2} \tag{4.31}$$

Therefore, beam ion number density n_b is

$$n_b = \frac{N_b}{V_{col}} = \frac{f_e L I^2 f_c^2}{M m_p v_b^2 V_{col}} \tag{4.32}$$

Since the diode voltage U accelerates the ions, the effective velocity of the beam ions v_b can be calculated under this accelerating voltage. The kinetic energy of the each ion due to this accelerating voltage provided by the diode voltage is $(1/2) M m_p v_b^2$. Therefore,

$$\frac{1}{2} M m_p v_b^2 = Z_{eff} e U \tag{4.33}$$

where Z_{eff} is the effective charge of the ion and e is the elementary or unit charge in Coulomb.

Therefore, ion beam velocity in m/s:

$$v_b^2 = \frac{2eUZ_{eff}}{Mm_p} \tag{4.34}$$

Then, the beam ion number density per m^3

$$n_b = \frac{f_e L I^2 f_c^2}{2eUZ_{eff}V_{col}} \tag{4.35}$$

where $f_e = 0.1$ (or 10 %) is the fraction of pinch inductive energy converted into beam kinetic energy [LS13].

Diode voltage in Volt is given as follows:

$$U = I f_c \frac{dL}{dt} + L\frac{dI}{dt} f_c + I f_c R \tag{4.36}$$

Discharge current in Ampere:

$$\frac{dI}{dt} = \frac{V_0 - \int \frac{I dt}{C_0} - r_0 I - I f_c \frac{dL}{dt}}{L_0 + L f_c} \tag{4.37}$$

where V_0 is charging voltage, C_0 is capacitor bank, r_0 is circuit resistance, L_0 is circuit inductance, and L is plasma inductance.

Plasma-ion number density per m^3 can be calculated as follows:

$$n_i V_{col} = n_0 V_0 \tag{4.38}$$

where n_i and n_0 are the ion number density and the ambient gas number density per m^3. V_0 is the total volume that the plasma sheath moves.

$$V_0 = \frac{4}{3}\pi(b^3 - a^3) \tag{4.39}$$

$$V_{col} = \frac{2\pi}{3}(b^3 - a^3)(1 + cos\theta) \tag{4.40}$$

Then, the plasma-ion number density is:

$$n_i = n_0 f_m \frac{2}{1 + cos\theta} \tag{4.41}$$

4.3 Results and Discussion

In the present work, we are comparing our simulation model results with a ready built experiment of the spherical plasma focus [Zav13]. The details of this experiment are given in the previous chapter.

The maximum beam-target neutron yield for the SPF with DT mixture gas (1:1) under the given parameters is 1.13×10^{13} as in the figure 4.2 , which is very close to the experimental neutron yield for the SPF [Zav13], which is also another validation

point for the developed spherical plasma focus model in addition to the discharge current and discharge current derivative given in the previous chapter.

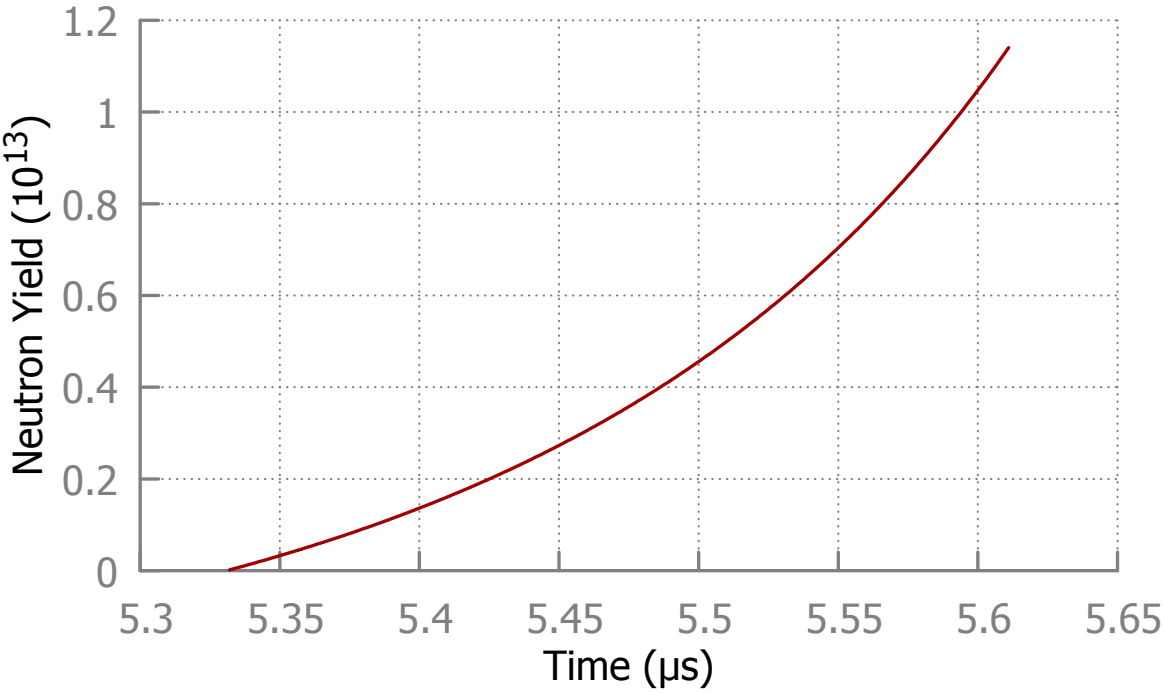

Figure 4.2 Neutron Yield

The figure 4.3 shows the total discharge current and discharge voltage for DT plasma mixture. The sharper voltage spike and deeper discharge current are good indicators of the better focus action in the plasma focus devices as explained in the previous chapter. As in figure 4.3, the sharpest discharge voltage and the deepest discharge current dip occur at the same time, which is 5.6 μs in this case.

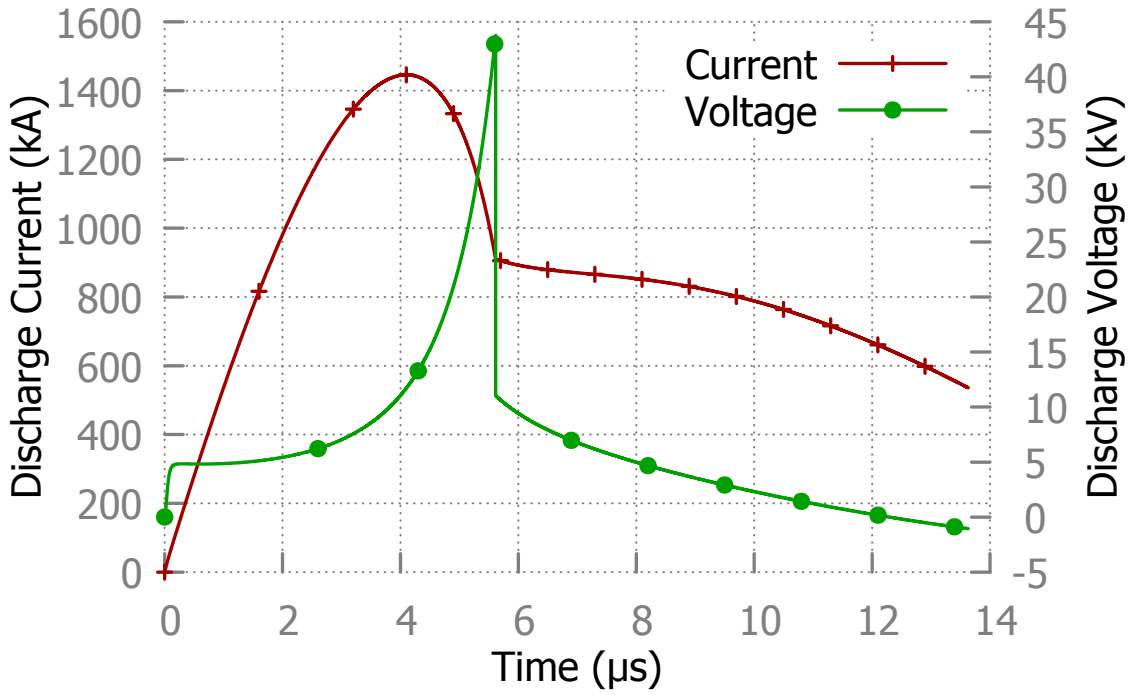

Figure 4.3 Plasma Discharge Current and Voltage

Fig. 4.4 and Fig. 4.5 show the plasma column-ion density and the beam-ion density. Fig. 4.6 shows the ratio of the beam-ion density to the plasma column-ion density. While the maximum plasma column-ion density is $1.61 \times 10^{24} m^{-3}$, the maximum beam-ion density is $6.84 \times 10^{20} m^{-3}$. The ratio of the maximum beam-ion density to the maximum plasma column-ion density is 4.2×10^{-4} as in Fig. 4.6, which shows the variation of this density ratio with respect to time for the radiative phase of the SPF.

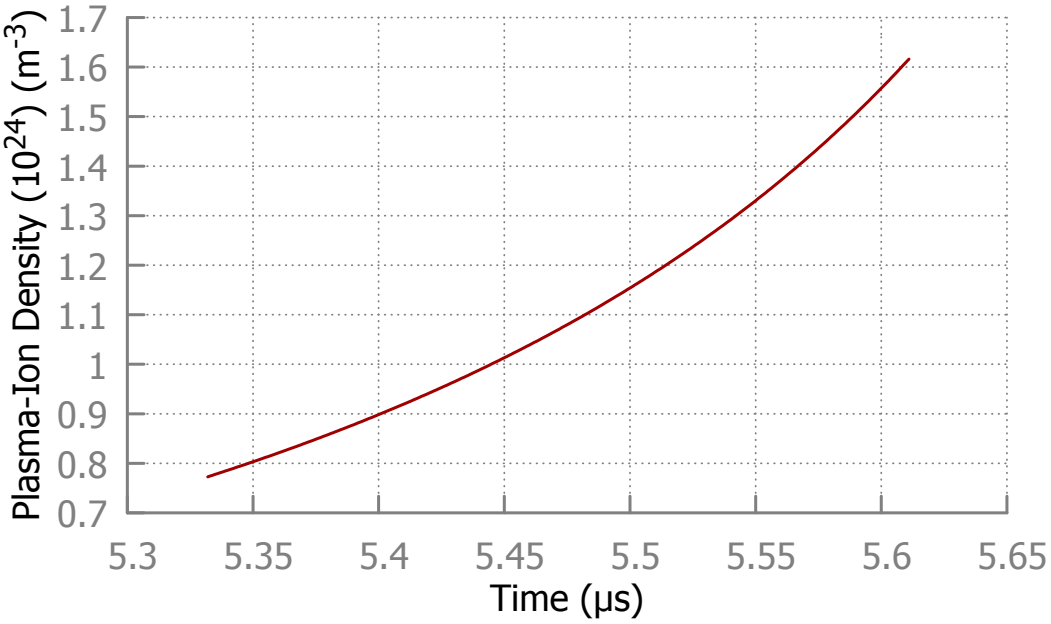

Figure 4.4 Plasma-Ion Density

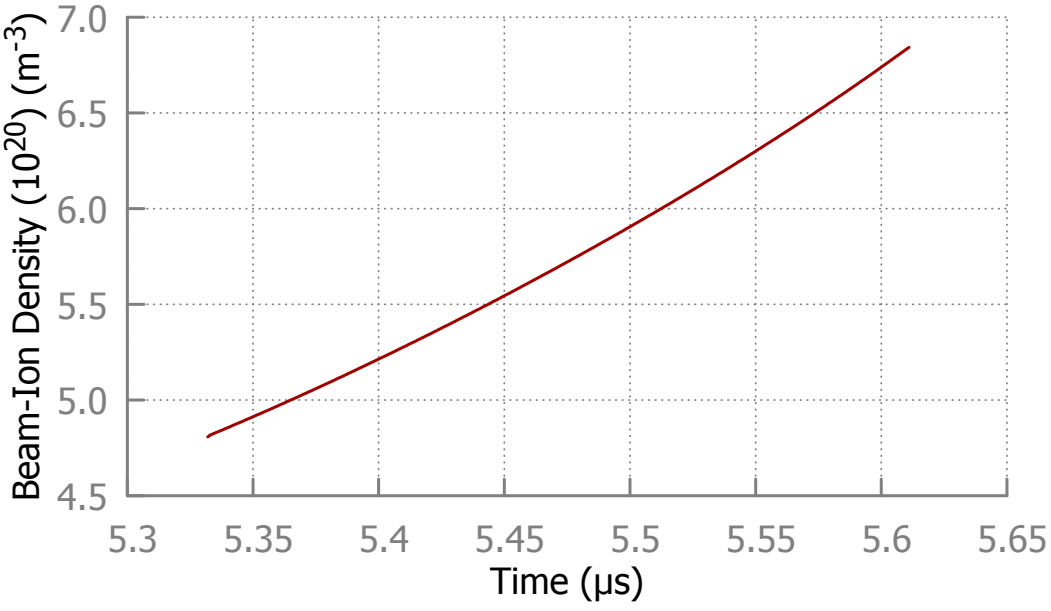

Figure 4.5 Beam-Ion Density

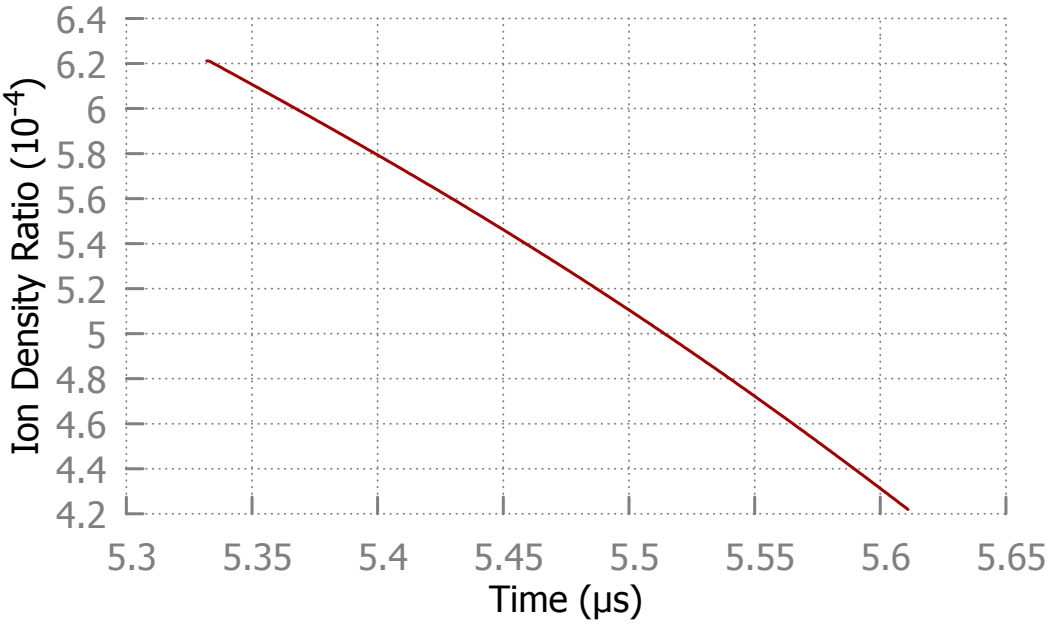

Figure 4.6 Ion Density Ratio for Beam-Ion and Plasma-Ion

While Fig. 4.7 shows the diode voltage of the SPF for radiative phase, Fig. 4.8 shows the beam-ion speed under this diode voltage. Since the diode voltage accelerates the beam-ions, beam-ion speed has the same trajectory as diode voltage. While the diode voltage reaches the maximum of 45.37 kV, the beam-ion speed reaches 208.44 $cm/\mu s$.

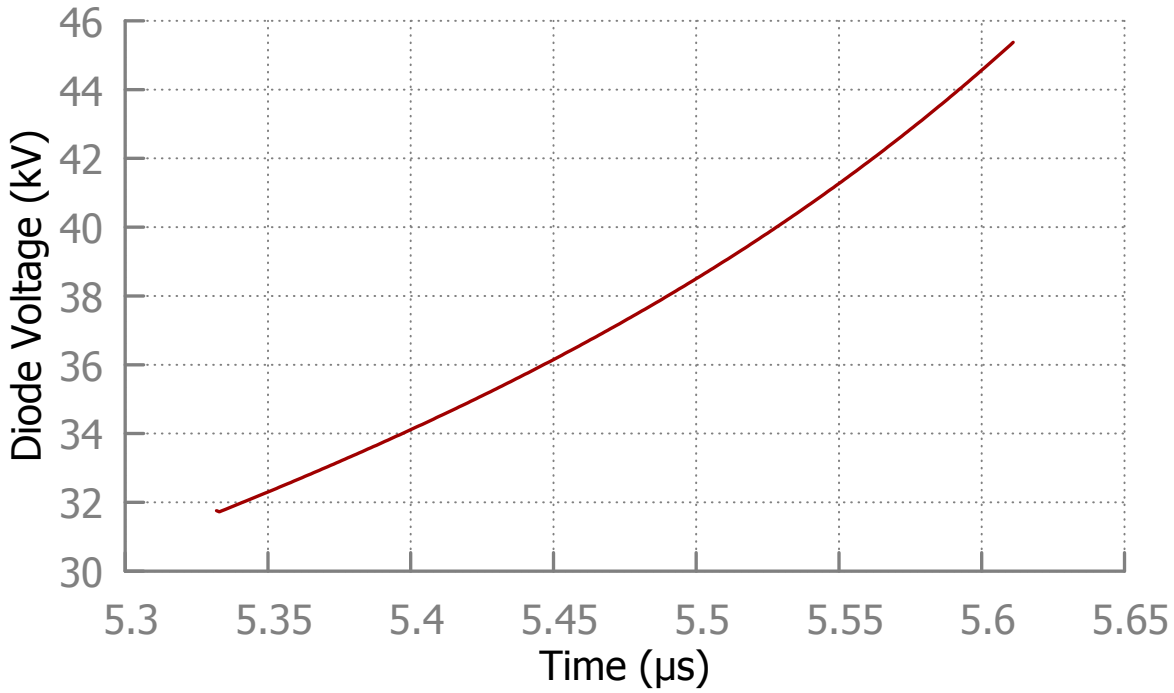

Figure 4.7 Diode Voltage

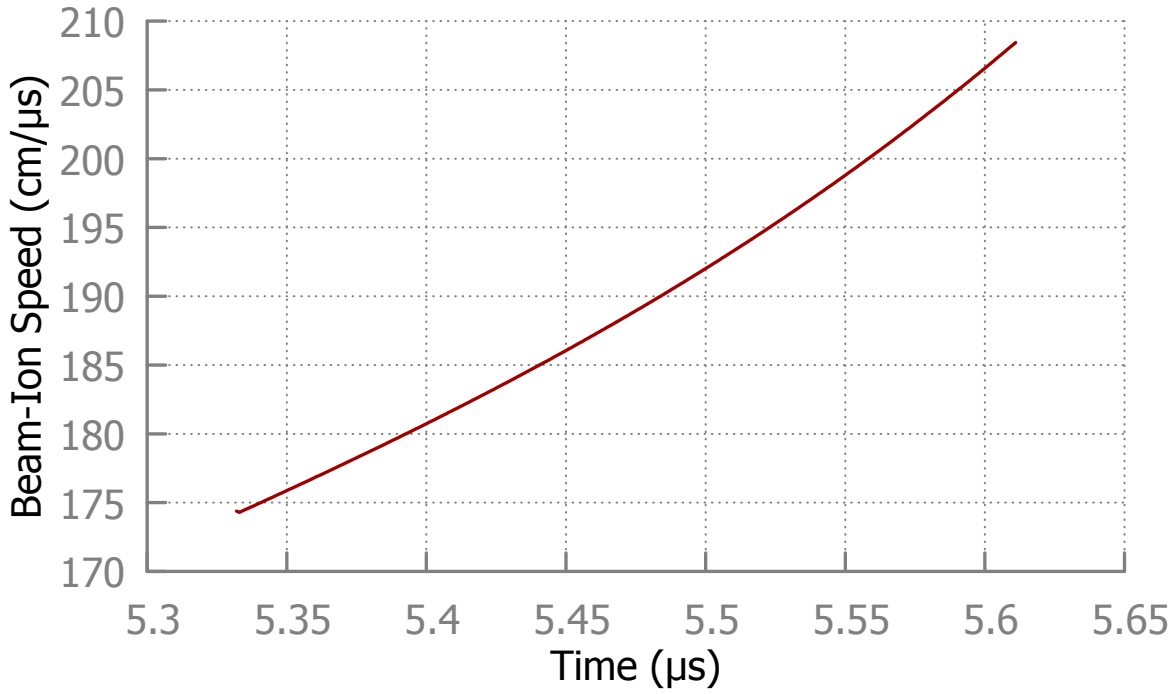

Figure 4.8 Beam-Ion Speed

Figure 4.9 shows the radiation power densities of the spherical plasma focus device for the line radiation P_{LN}, bremsstrahlung radiation P_{BR}, and radiative recombination P_{REC}, which are the main radiations emitted from the plasma column in the radiative phase. Line radiation has more effect on the plasma column than bremsstrahlung radiation and radiative recombination in this study with DT gas mixture. While line radiation reaches the maximum of 3.32×10^{11} W/m^3, bremsstrahlung radiation and radiative recombination reach the maximum of 1.57×10^{11} W/m^3 and 1.82×10^{8} W/m^3, respectively.

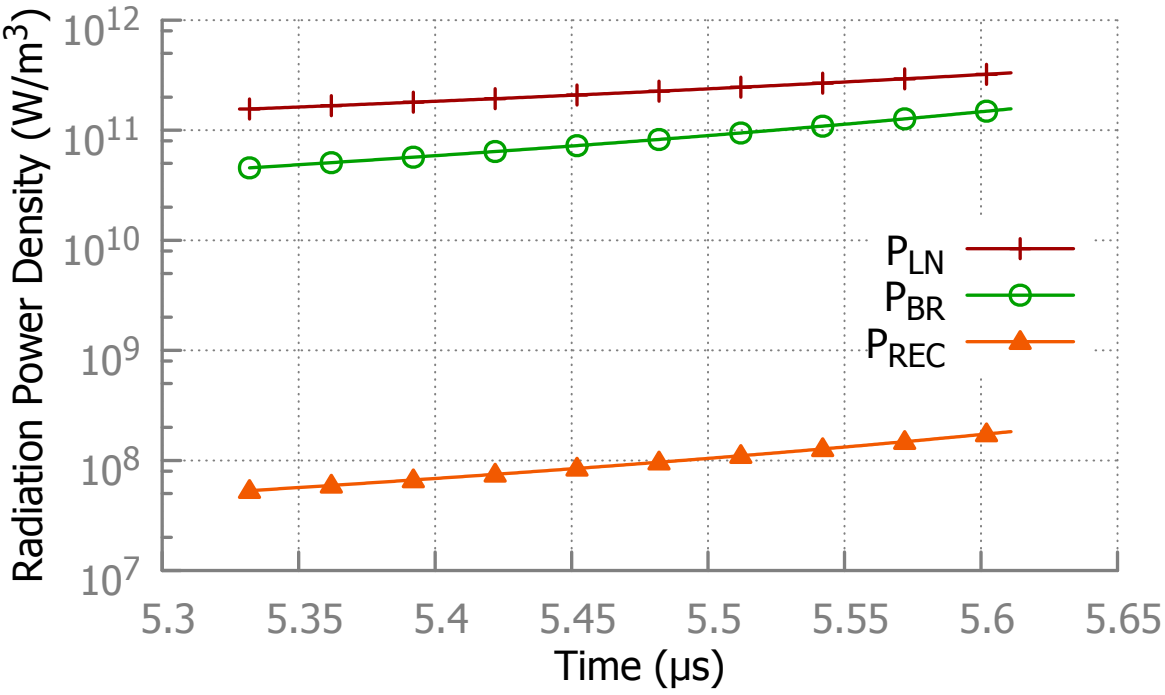

Figure 4.9 Plasma Radiation Emissions

Fig 4.10 shows the joule heating, total radiation and the difference between joule heating and total radiations. P_J represents the joule heating. P_{JRad} represents the difference between the total radiations emitted and joule heating. P_{Rad} represents the total radiations including line radiation, bremsstrahlung radiation and radiative recombination. While radiations emitted is considered as loss terms, the joule heating is considered as gain term for the plasma column in terms of the plasma energy. Even though joule heating, which is due to the increased plasma resistance as seen in Fig. 4.11, as the energy gain term for the plasma column increases from 4.6×10^{10} to 2.69×10^{11}, the total radiation emitted as the energy loss terms for the plasma column increases from 2.02×10^{11} to 4.88×10^{11}.

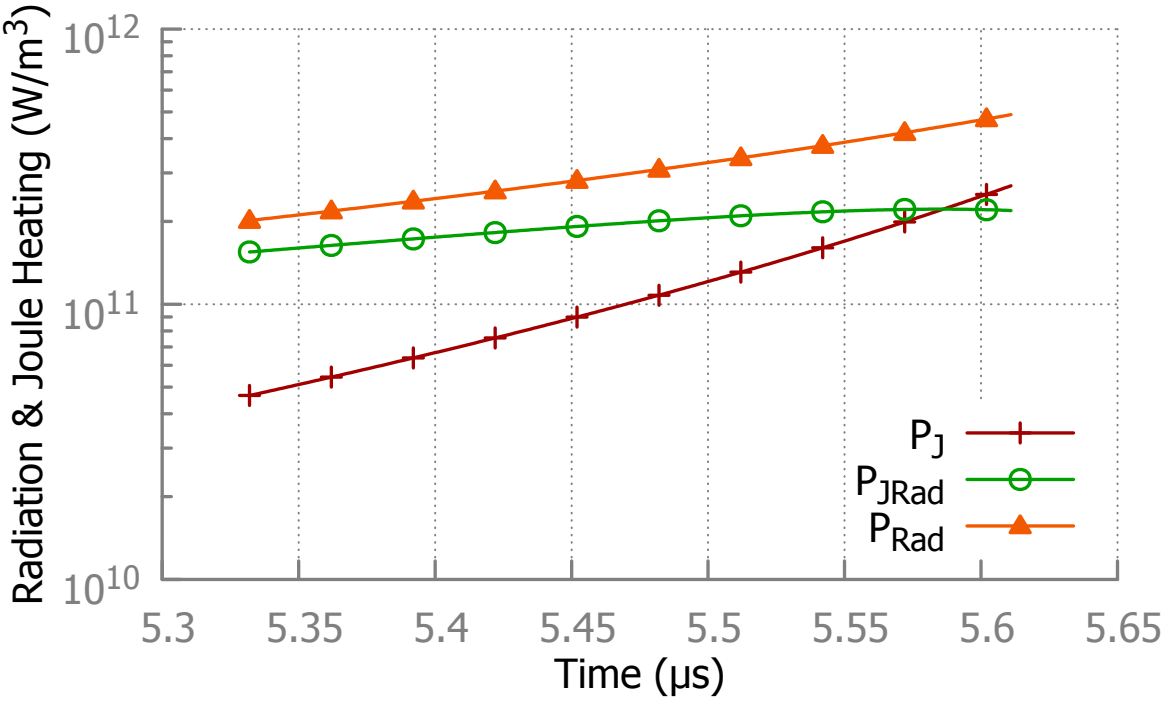

Figure 4.10 Joule Heating and Radiations

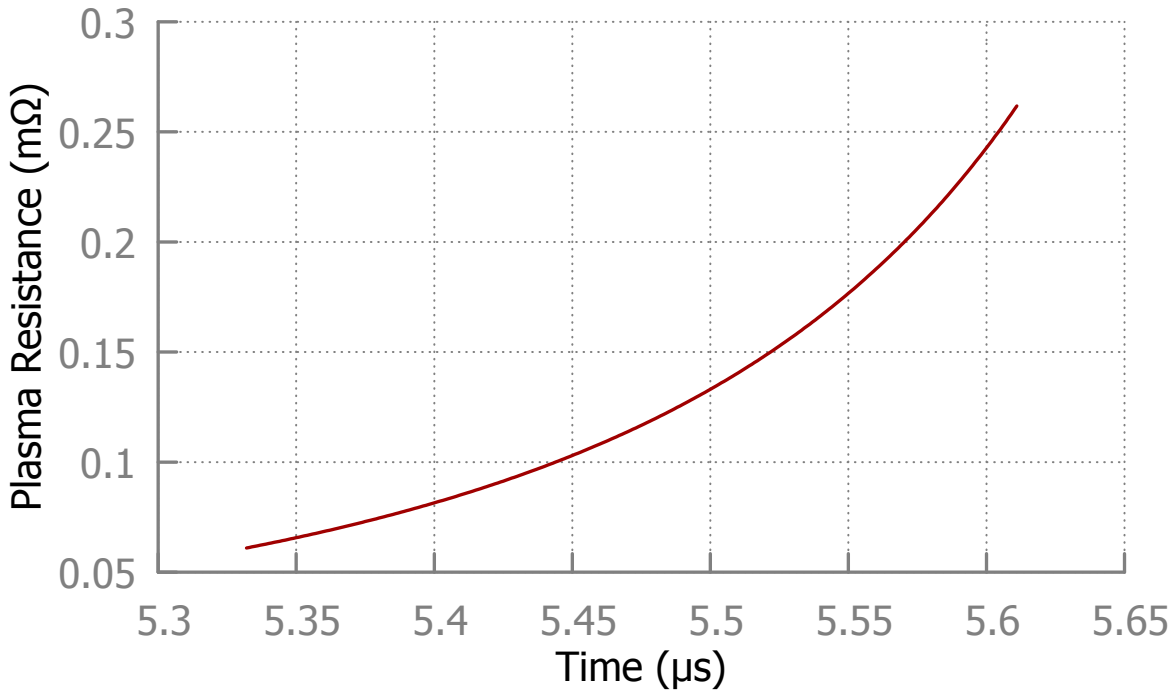

Figure 4.11 Plasma Resistance

Since the joule heating as the gain term is less than the total radiations as loss terms, the plasma column loses energy in the radiative phase of the SPF. The difference between the radiation emitted and joule heating has an increasing trend over time which is changing from 1.54×10^{11} to 2.19×10^{11}. Therefore, the plasma column could lose more energy with the longer radiative phase. The plasma resistance in Fig. 4.11 was increased from 0.06 $m\Omega$ to 0.26 $m\Omega$ which is a factor of 4.3 higher resulting in higher joule heating as plasma energy gain mechanism.

4.4 Conclusion

In this work, the focus is on the neutron yield, the emitted radiations and the ion properties, such as ion number densities and ion speed. The neutron yield with the given machine and operational parameters is 1.13×10^{13}, which is close enough to the experimental results which is 1.30×10^{13} [Zav13]. Therefore, the neutron yield can be considered another validation mechanism for the developed spherical plasma focus model after using the discharge current and discharge current derivative wave forms.

Two different ion densities are investigated. These are the plasma column-ion density and beam-ion density. The achieved maximum ion densities are 1.61×10^{24} for plasma column and 6.84×10^{20} for the ion beam. Under the maximum diode voltage of 45.37 kV, the calculated beam-ion speed is 208.44 $cm/\mu s$.

The main radiation mechanisms, which are bremsstrahlung, radiative recombination and line radiation as plasma energy loss terms, and joule heating as plasma energy gain term show that spherical plasma focus in this configuration is losing more energy than gaining energy in the radiative phase. Since the difference between energy gain term and energy loss terms are increasing over time, while the longer radiative phase could lead to higher radiation emissions, the shorter radiative phase with higher plasma resistance could result in gaining more plasma energy in this phase.

CHAPTER

5

SUMMARY, RESULTS AND DISCUSSION

In this work, a spherical plasma focus model was developed in order to study the plasma sheath dynamics, radiation emissions (bremsstrahlung, line radiation, and radiative recombination), and the ion properties in the spherical plasma focus device. Rundown phase I, rundown phase II, reflected shock phase, and radiative phase are the main phases of the developed spherical plasma focus model.

The developed model was validated and compared with the experimental data of a spherical plasma focus chamber. The discharge current and its derivative are used in order to validate the plasma focus model. A good agreement between the theoretical calculations and the experimental results is achieved and provided a proof of the model accuracy. The achieved accurate neutron yield prediction between the spherical plasma focus model and the experiment with the spherical plasma focus chamber can also be considered as another model validation.

In this study, the spherical plasma focus device consists of two concentric electrodes. While the inner electrode has 8 cm radius, the radius of the outer electrode is 14.5 cm. While the capacitor bank is 432 μF, the charging voltage and external inductance are 25 kV and 36 nH, respectively. The equal amount of DT mixture is used with 14.5 Torr gas pressure.

While the current sheath is expanded in the rundown phase I during the acceleration of the current sheath in this phase, it is compressed during the rundown phase II and the reflected shock phase in both axial and radial directions. The current sheath motion is assumed to be perpendicular to the direction of the acceleration for all the phases of the model.

The model considers the total energy distribution into the system and the total power from the capacitor bank in the calculations, and predicted the energy deposited into the the plasma sheath and the power deposited into the tube.

The rundown phase I starts immediately after the gas breakdown is completed, and it ends when the current sheath reaches the equator point of the spherical shape. The snowplow model and the shock wave equations constitute the main frame of

this phase to calculate the plasma and shock wave features in the spherical plasma focus device by using the calculated momentum, magnetic force, inductance and the circuit equations.

The time when the rundown phase II starts corresponds to the time when the current sheath reaches the equator point, and this phase ends when the shock front hits the axis of the spherical shape. In this phase, the calculation for the magnetic field is different than that of the rundown phase I. Therefore, the snowplow model and shock wave equations are used with the necessary magnetic field modification in the rundown phase II, and this modification applies to the momentum, magnetic force, and inductance equations as well in order to predict the plasma and the shock wave properties correctly.

When the shock front hits the axis, it is the end of the rundown phase II and the beginning of the reflected shock phase. After this point, the shock front reflects back towards the current sheath with the assumed constant shock front velocity, and the reflected shock phase ends when the shock front meets the incoming current sheath.

While the current sheath and the shock front move in the same direction (towards the axis) in the rundown phase I and the rundown phase II which results in an increase in the distance between the current sheath and the shock front, the current sheath (towards the axis) and the reflected shock front (towards the current sheath) move in the opposite direction in the reflected shock phase which gives rise to a decrease in the distance between the current sheath and the reflected shock front.

The modification of this phase for calculation of the plasma and the shock wave properties is the assumed constant reflected shock front velocity which applies to the

all the governing equations in this phase.

Radial phase starts when the current sheath and the reflected shock front meet, and then the current sheath continues to move radially inward by compressing the generated plasma column until it reaches the axis. Neutron production, radiation effect (bremsstrahlung radiation, spectral line radiation, and radiative recombination), joule heating, and the ion properties in the spherical plasma focus device are the main interests in this phase. While bremsstrahlung radiation, line radiation, and radiative recombination are considered as energy loss terms, joule heating is considered as an energy gain term in this phase of the spherical plasma focus device.

In addition to the momentum equation and magnetic pressure equation with snow plow model, shock wave theory, and circuit equations, the effect of the radiation emissions and joule heating with plasma resistance are also included in the radiative phase calculations.

In the radiative phase, the temporal changes of the pinch column plasma inductance and of the discharge current, and a large induced electric field occur due to the change in the current sheath dynamics. The induced electric field leads to the plasma disruption at the maximum compression which gives rise to several phenomena in the focus region in this phase such as the emission of electromagnetic radiation, the emission of electrons and ions, and the generated high voltage in the pinch which results in a beam of fast ions due to the diode action in a thin layer close to the anode in the spherical plasma focus.

While the generated high voltage in the radial phase accelerates the electrons towards the anode which causes the hard x-ray production when the accelerated

electrons hit the anode, it accelerates the ion in the opposite direction which leads to the beam-target neutron production when the accelerated ions interact both with the pinch and the plasma outside the pinch in the plasma focus device.

In this study, the snow plow model, shock wave equations including the planar shock-jump equations, and the circuit equations are used to calculate the plasma and shock wave parameters in the spherical plasma focus model. The developed spherical plasma focus model is used to predict both the plasma and the shock wave properties with the help of the linear approximation method which is used to solve the equations.

The main calculations from the spherical plasma focus model for hydrogen, deuterium, tritium, and deuterium-tritium mixture are temporal evolution of the current, inter-electrode voltage, current sheath temperature and density, shock velocity and displacement, current sheath velocity and displacement, plasma inductance, induced magnetic field, neutron yield, radiation emissions (Bremsstrahlung radiation, spectral line radiation, and radiative recombination), joule heating, plasma resistance, beam-ion number density and energy, beam-ion velocity, plasma-ion number density, diode voltage, energy deposition in the plasma sheath and power deposited into the tube.

The model is also used to find the correlation of the filling gas pressure and the discharge voltage with the plasma temperature and the pinch start time for hydrogen, deuterium, and tritium.

The sharp voltage spike and the deep in the discharge current are indications of the good focus actions in the plasma focus devices, and they occur at the same time. The sharp voltage spike with the maximum discharge voltage of 43.7 kV and the deep in the discharge current from the maximum of 1446 kA to 919 kA is achieved in this

study.

Since the shock front ionizes the gases in front of the plasma slug, increasing the shock front velocity increases the plasma temperature during the plasma motion. While the shock front and the current sheath velocity reach the values of around 8 cm/μs and 5 cm/μs, the plasma temperature reaches around 16 eV in the spherical plasma focus device.

The predicted total energy and total power are 135 kJ and 68.46 GW. While 54 kJ (40% of the total energy) is deposited into the plasma sheath, 39.84 GW and 27 GW are deposited into the tube and the plasma, respectively, at the end of the motion.

A good match between the spherical plasma focus model and the results from the experiment of the spherical plasma focus chamber is achieved in terms of the neutron yield. The maximum neutron yield with equal amount of deuterium-tritium gas mixture is 1.13×10^{13} from the model, which is close enough to the experimentally measured neutron yield of 1.30×10^{13}.

Two different ion densities are investigated in the spherical plasma focus model. These two ion densities are the plasma column-ion density and the beam-ion density. While the plasma column-ion density reaches the value of 1.61×10^{24} m^{-3}, the maximum beam-ion density is 6.84×10^{20} m^{-3}.

Beam-ion speed and diode voltage which accelerates the beam-ions in the radiative phase are also important factors to be considered. The calculations show that the diode voltage is predicted as the maximum of 45.37 kV, and the beam-ion speed reaches the value of 208.44 cm/μs in the spherical plasma focus device.

As the main radiations emitted from the plasma column in the radiative phase,

bremsstrahlung radiation, line radiation, and radiative recombination power densities are calculated with deuterium-tritium gas mixture in the model. The calculations indicates that line radiation has more effect on the plasma column compared to bremsstrahlung radiation and radiative recombination in the spherical plasma focus in that line radiation reaches the maximum value of 3.32 $\times 10^{11}$ W/m^3 but the maximum bremsstrahlung radiation and radiative recombination are 1.57 10^{11} W/m^3 and 1.82 10^8 W/m^3, respectively.

Joule heating due to the increased plasma resistance is calculated as the energy gain term for the plasma column in the model. It is found that joule heating is increasing from 4.6 $\times 10^{10}$ W/m^3 to 2.96 $\times 10^{11}$ W/m^3 but the total emitted radiation from the plasma column as the energy loss term is increasing from 1.54 $\times 10^{11}$ W/m^3 to 2.19 $\times 10^{11}$ W/m^3. Therefore, the plasma column loses energy in the radiative phase of the spherical plasma focus device.

The difference between joule heating and the total emitted radiations indicated that the plasma column could lose more energy with the longer radiative phase. The plasma resistance is increasing from 0.06 Ω to 0.26 Ω which gives rise to higher joule heating as the plasma energy gain mechanism. Therefore, it could be possible for the plasma column to gain more energy and to lose less energy with the shorter radiative phase and higher plasma resistance.

The developed simulation is run to study the effect of the filling gas pressure, discharge voltage, and the molecular mass of the gas on the maximum plasma temperature and pinch start time for hydrogen, deuterium, and tritium in the spherical plasma focus device. While the gas pressure is incremented by 1 Torr from 1 Torr to

25 Torr in addition to 0.5 Torr gas pressure, the discharge voltage has a range from 10 kV to 100 kV. It is found that the maximum plasma temperature can be achieved with a relatively shorter pinch start time using a relatively heavier gas with lower gas pressure and higher discharge voltage.

Another study is conducted to investigate the plasma parameters for hydrogen, deuterium, and tritium separately with the charging voltage of 25 kV. For the discharge currents and voltages, while the peak discharge voltages are 55 kV for hydrogen, 46.85 kV for deuterium, and 41 kV for tritium, the peak discharge currents and the dip in the discharge currents are 1.232 MA and 809 kA for hydrogen, 1.394 MA and 890 kA for deuterium, and 1.487 MA and 923 kA for tritium, respectively. Since the deepest discharge current dip and the highest discharge voltage spike can be achieved with hydrogen, hydrogen is a better candidate for a better focus action in the spherical plasma focus device compared to deuterium and tritium for the same conditions.

CHAPTER

6

CONCLUSION AND FUTURE WORK

Developed spherical plasma focus model shows that while the snow plow model with the help of the shock wave equations can simulate the plasma focus sheath dynamics and radiation emissions accurately, coupling these equations with the circuit equations allows to obtain electrical parameters from the model.

In general, the plasma focus models are validated by using current wave form from the experiments because the discharge current has significant effect on the plasma dynamic, electrodynamic, thermodynamic, and radiations emitted from the plasma

focus devices. Since the current wave form and the derivative of the current wave form are used to validate this model, the accurate simulation in this work supports the idea of the current wave form validation technique.

In order to match the discharge current from the spherical plasma focus model with the discharge current of the spherical plasma focus experiment, the current fraction factor f_c and the mass fraction factor f_m are used. The used mass fraction factor f_m is 0.11, and the current fraction factor f_c is 0.68. After the current fraction factor is calculated as 0.66, it is adjusted to 0.68 in order to achieve a better match between the calculated discharge current and the experimentally measured discharge current.

The current fraction factor is calculated as follows:

$$I_{peak} = \frac{2\pi C_0 V_0}{\tau} \tag{6.1}$$

$$f_c = \frac{I_{exp}}{I_{peak}} \tag{6.2}$$

where I_{peak} and I_{exp} are the theoretical and experimental peak discharge current, and τ is the discharge time period [Saw10].

Even though a good enough match is achieved between the calculations from the spherical plasma focus model and the results from the spherical plasma focus experiment in terms of the discharge current and the derivative of the discharge current, there is still a small difference between theoretical calculations and the measured

results. The possible reason for that is as follows:

In the model, mass fraction factor f_m and the current fraction factor f_c are used as two constant value for all the phases of the model but it could be variable in the experiment for each small time interval. Gas breakdown, which occurs before the current sheath starts moving, could be another possible reason for this small difference because the gas breakdown has a strong effect on the discharge current. While the current sheath motion begins after the gas breakdown is completed in the experiment, the model does not take into account the time requirement for the gas breakdown, and the current sheath motion starts with the rundown phase I (which is an acceleration phase) in the model. Therefore, this time delay in the current sheath motion could be another reason for the slight difference between the model and the experimental results.

The developed model also shows that the compact spherical plasma focus device can produce high discharge current, high neutron yield, and high plasma column-ion density. While the achieved discharge current is around 1.5 MA, the neutron yield is on the order of 10^{13} which is a good neutron yield for the compact plasma focus device that has 8 cm inner electrode radius and 14.5 cm outer electrode radius. The achieved plasma column-ion density is on the order of 10^{24} m^{-3} in the spherical plasma focus device.

Based on the radiation emissions and joule heating with the plasma resistance, it is also found that while longer radiative phase results in more energy loss from the plasma column, the higher plasma resistance lead to more energy gain. Therefore, a shorter radiative phase with a higher plasma resistance can be a solution to gain energy

into the plasma column for producing higher energy electrons and ions, intense X-ray and neutron sources, and future application.

The spherical plasma focus model can be used for more investigations of the plasma focus phenomena, and there are some points that should be considered for more complete plasma focus model. The future work that should be taken into account are as follows:

1. Hydrogen, deuterium, and tritium are used in the spherical plasma focus model. The admixture of the other gases such as argon, neon, and Xenon with different ratio can be investigated to see the effect of the admixture gases on the plasma parameters.

2. Since the breakdown has a strong effect on the discharge current, it can be included in the model for more accurate results.

3. Instead of using the generally assumed mass fraction factor and approximate calculation of the current fraction factor, necessary equations can be implemented into the model to eliminate these factors.

4. The impurity both in the beginning of the current sheath motion from the insulator surface and in the radiative phase from the anode can be included for more realistic results.

5. Anomalous resistivity and instabilities occur during the radiative phase of the plasma focus. Therefore, inclusion of these effects can be helpful to predict better results from the spherical plasma focus model.

6. The prediction of the soft X-ray and hard X-ray production can guide to further investigate the possible application of the plasma focus device as X-ray source. Therefore, soft X-ray and hard X-ray production can be added into the model.

7. The possible application areas of the electrons and ions emitted by the spherical plasma focus device can be investigated using the more complete model for scientific and industrial applications.

BIBLIOGRAPHY

[AK10] Abdollahzadeh, M & Kiai, S. S. "Time dependent behavior of neutron emission in dena plasma focus". *Journal of Fusion Energy* **29**.3 (2010), pp. 218–222.

[Abl10] Ablesimov, V. et al. "Correlation of the neutron yield anisotropy with the electrical characteristics of a plasma focus discharge". *Plasma Physics Reports* **36**.5 (2010), pp. 403–406.

[Abl12] Ablesimov, V. et al. "Correlation between the neutron yield from a plasma focus device and the jump in the discharge current". *Plasma physics reports* **38**.10 (2012), pp. 820–823.

[AB14] Aghamir, F. M. & Behbahani, R. A. "Energy spectrum of multi-radiation of X-rays in a low energy Mather-type plasma focus device". *Chinese Physics B* **23**.6 (2014), p. 065203.

[Ahm06a] Ahmad, S et al. "Catalytic action of {beta} source on x-ray emission from plasma focus". *Review of scientific instruments* **77**.1 (2006).

[Ahm06b] Ahmad, S et al. "Enhanced and reproducible neutron emission from a plasma focus with pre-ionization induced by depleted uranium (U238)". *Plasma physics and controlled fusion* **48**.6 (2006), p. 745.

[Ahm14] Ahmad, S et al. "Correlation of Neutron and X-ray Emission from Plasma Focus with Pre-ionization". *Journal of Fusion Energy* **33**.6 (2014), pp. 720–725.

[Ake13a] Akel, M. "Numerical Experiments on Oxygen Plasma Focus: Scaling Laws of Soft X-Ray Yields". *Journal of Fusion Energy* **32**.4 (2013), pp. 464–470.

[AL13] Akel, M & Lee, S. "Scaling Laws of Nitrogen Soft X-ray Yields from 1 to 200 kJ Plasma Focus". *Journal of Fusion Energy* **32**.1 (2013), pp. 107–110.

[Ake13b] Akel, M et al. "Computational Study of Emitted Spectra from the Neon Plasma Focus". *Journal of Fusion Energy* **32**.4 (2013), pp. 503–508.

[Ake14a] Akel, M et al. "Properties of ion beams generated by nitrogen plasma focus". *Journal of Fusion Energy* **33**.2 (2014), pp. 189–197.

[Ake13c] Akel, M. “Soft X-ray Emission Optimization Studies with Krypton and Xenon Gases in Plasma Focus Using Lee Model”. *Journal of Fusion Energy* **32**.5 (2013), pp. 523–530.

[Ake14b] Akel, M. et al. “Characterization of oxygen ion beams emitted from plasma focus”. *Vacuum* **110** (2014), pp. 54–57.

[AH10] Al-Hawat, S. et al. “Using Mather-type plasma focus device for surface modification of AISI304 Steel”. *Vacuum* **84**.7 (2010), pp. 907–912.

[AH15] Al-Hawat, S. et al. “X-ray Intensity Measurements in 2.8 kJ Plasma Focus Device Operated with Argon Using a Five Channel Diode Spectrometer”. *Journal of Fusion Energy* **34**.1 (2015), pp. 163–171.

[ARC98] Aliaga-Rossel, R & Choi, P. “Experimental observations of the spatial anisotropy of the neutron emission in a medium energy plasma focus”. *Plasma Science, IEEE Transactions on* **26**.4 (1998), pp. 1138–1145.

[Ang05] Angeli, E et al. “Preliminary results on the production of short-lived radioisotopes with a Plasma Focus device”. *Applied radiation and isotopes* **63**.5 (2005), pp. 545–551.

[AC14] Appelbe, B. & Chittenden, J. “Understanding neutron production in the deuterium dense plasma focus”. *9TH INTERNATIONAL CONFERENCE ON DENSE Z PINCHES*. Vol. 1639. 2014, pp. 9–14.

[AV04] Atzeni, S. & Vehn, J. Meyer-ter. *The Physics of Inertial Fusion: BeamPlasma Interaction, Hydrodynamics, Hot Dense Matter: BeamPlasma Interaction, Hydrodynamics, Hot Dense Matter*. Vol. 125. Oxford University Press, 2004.

[Bag11a] Baghdadi, R et al. “Characterization of the Soft X-Ray Emission from the APF Plasma Focus Device Operated in Neon”. *Journal of Fusion Energy* **30**.2 (2011), pp. 137–143.

[Bag11b] Baghdadi, R et al. “Investigation of the neutron angular distribution and neutron yield on the APF plasma focus device”. *Journal of Fusion Energy* **30**.1 (2011), pp. 72–77.

[Bah14] Baharani, M. et al. “Three Dimensional Angular Distributions of X-Rays in a 4 kJ Plasma Focus Device for Different Anode Tips Using TLD-100 Dosimeters”. *Contributions to Plasma Physics* **54**.9 (2014), pp. 749–755.

[Beg00] Beg, F. et al. “Study of x-ray emission from a table top plasma focus and its application as an x-ray backlighter”. *Journal of Applied Physics* **88**.6 (2000), pp. 3225–3230.

[BA11] Behbahani, R. & Aghamir, F. “Anomalous resistivity effect on multiple ion beam emission and hard x-ray generation in a Mather type plasma focus device”. *Physics of Plasmas (1994-present)* **18**.10 (2011), p. 103302.

[BA12] Behbahani, R. & Aghamir, F. “Correlation of current drop, filling gas pressure, and ion beam emission in a low energy Mather-type plasma focus device”. *Journal of Applied Physics* **111**.4 (2012), p. 043304.

[BA13] Behbahani, R. & Aghamir, F. “Post-pinch generation of electron beam in a low energy Mather-type plasma focus device”. *Journal of Plasma Physics* **79**.05 (2013), pp. 777–782.

[Ber98] Bernard, . et al. “Scientific status of plasma focus research”. *J. Moscow Phys. Soc* **8** (1998), pp. 93–170.

[Bhu04] Bhuyan, H et al. “Comparative study of soft x-ray emission characteristics in a low energy dense plasma focus device”. *Journal of applied physics* **95**.6 (2004), pp. 2975–2981.

[Bhu11] Bhuyan, M et al. “Temporal and spatial study of neon ion emission from a plasma focus device”. *Physics of Plasmas (1994-present)* **18**.3 (2011), p. 033101.

[Bob14] Bobin, J.-L. *Controlled thermonuclear fusion*. World Scientific, 2014.

[Bos93] Bostick, W. et al. “Time resolved energy spectrum of the axial ion beam generated in plasma focus discharges”. *Nuclear fusion* **33**.3 (1993), p. 413.

[Bur10] Bures, B. L. et al. “Enhancing neutron emission from a 500-J plasma focus by altering the anode geometry and gas composition”. *Plasma Science, IEEE Transactions on* **38**.4 (2010), pp. 667–671.

[Cas14] Casanova, F et al. “Numerical simulation of current sheet instabilities in a small plasma focus”. *Journal of Physics: Conference Series*. Vol. 511. 1. 2014, p. 012031.

[Cas00] Castillo, F et al. “Evidence of thermal and non-thermal mechanisms co-existing in dense plasma focus D-D nuclear reactions”. *J. Phys. D Appl. Phys.* **33**.2 (2000), 141–147.

[CM14] Castillo-Mejía, F et al. “Neutron emission characterisation at the FN-II Dense Plasma Focus”. *Journal of Physics: Conference Series*. Vol. 511. 1. 2014, p. 012021.

[CM01] Castillo-Mejía, F. et al. “Small plasma focus studied as a source of hard X-ray”. *Plasma Science, IEEE Transactions on* **29**.6 (2001), pp. 921–926.

[Cec12] Ceccolini, E et al. “EBT2 dosimetry of x-rays produced by the electron beam from a Plasma Focus for medical applications”. *Journal of Applied Physics* **112**.5 (2012), p. 054901.

[Cho90] Choi, P et al. “Characterization of self-generated intense electron beams in a plasma focus”. *Laser and Particle Beams* **8**.03 (1990), pp. 469–476.

[Cla15] Clausse, A. et al. “Feasibility study of a hybrid subcritical fission system driven by Plasma-Focus fusion neutrons”. *Annals of Nuclear Energy* **78** (2015), pp. 10–14.

[DL07] Di Lorenzo, F et al. “Hard x-ray source for flash radiography based on a 2.5 kJ plasma focus”. *Journal of Applied Physics* **102**.3 (2007), p. 033304.

[Dol82] Dolan, T. J. *Fusion research*. 1982.

[Dul14] Dulatov, A. et al. “Generation of hard X-ray emission by the electron beam in plasma focus facilities”. *Plasma Physics Reports* **40**.11 (2014), pp. 902–909.

[Eta11] Etaati, G. et al. “Angular Distribution of Argon Ions and X-Ray Emissions in the Apf Plasma Focus Device”. *Journal of Fusion Energy* **30**.2 (2011), pp. 121–125.

[FS12] Fani, N. & Savaloni, H. "* Investigation on the formation of titanium nitride thin films on 304 type stainless steel using plasma focus device". *Journal of Theoretical and Applied Physics* **6**.1 (2012), pp. 1–7.

[Far11] Farahani, N. D. et al. "X-Ray measurement and enhancement of SBUPF1 plasma focus device in different Ar pressures and operating voltages". *Journal of fusion energy* **30**.6 (2011), pp. 466–472.

[Fav92] Favre, M et al. "X-ray emission in a small plasma focus operating with H2-Ar mixtures". *Plasma Sources Science and Technology* **1**.2 (1992), p. 122.

[Fil62] Filippov, N. V. et al. "High temperature dense plasma in a non-cylindrical z-pinch". *Nucl. Fusion Suppl.* **2** (1962), p. 577.

[Fog14] Fogliatto, E et al. "A model of hard X-rays emission from free expanding Plasma-Focus discharges". *Journal of Physics: Conference Series*. Vol. 511. 1. 2014, p. 012036.

[GM08] Garanin, S. & Mamyshev, V. "Two-dimensional MHD simulations of a plasma focus with allowance for the acceleration mechanism for neutron generation". *Plasma Physics Reports* **34**.8 (2008), pp. 639–649.

[GM12] Ghareshabani, E & Mohammadi, M. "Measurement of the Energy of Nitrogen Ions Produced in Filippov Type Plasma Focus Used for the Nitriding of Titanium". *Journal of fusion energy* **31**.6 (2012), pp. 595–602.

[GL60] Glasstone, S. & Lovberg, R. H. *Controlled thermonuclear reactions: an introduction to theory and experiment*. van Nostrand, 1960.

[GR95] Goldston, R. J. & Rutherford, P. H. *Introduction to plasma physics*. CRC Press, 1995.

[Gon09] Gonzalez, J. et al. "A lumped parameter model of free expanding Plasma Focus". *Braz. J. Phys.* **39**.4 (2009), pp. 633–637.

[Gon04] Gonzalez, J. et al. "A lumped parameter model of plasma focus". *IEEE T. Plasma Sci.* **32**.3, 2 (2004), pp. 1383–1391.

[Gou07] Goudarzi, S et al. "Experimental study of the variation of neutron emission anisotropy in a Filippov-type plasma focus facility". *Journal of Fusion Energy* **26**.4 (2007), pp. 343–347.

[Gou08] Goudarzi, S. et al. “A Model Based on Lumped Parameters for Filippov-type Plasma Focus Devices”. *J. Fusion Energ.* **27**.3 (2008), pp. 195–199.

[Gri07a] Gribkov, V. A. et al. “Plasma dynamics in the PF-1000 device under full-scale energy storage: II. Fast electron and ion characteristics versus neutron emission parameters and gun optimization perspectives”. *J. Phys. D Appl. Phys.* **40**.12 (2007), 3592–3607.

[Gri15] Gribkov, V. “Physical processes taking place in dense plasma focus devices at the interaction of hot plasma and fast ion streams with materials under test”. *Plasma Physics and Controlled Fusion* **57**.6 (2015), p. 065010.

[Gri07b] Gribkov, V. et al. “Plasma dynamics in PF-1000 device under full-scale energy storage: I. Pinch dynamics, shock-wave diffraction, and inertial electrode”. *J. Phys. D Appl. Phys* **40**.7 (2007), p. 1977.

[Gri64] Griem, H. R. *Plasma spectroscopy*. Vol. 1. 1964.

[GS78] Gullickson, R. & Sahlin, H. “Measurements of high-energy deuterons in the plasma-focus device”. *Journal of Applied Physics* **49**.3 (1978), pp. 1099–1105.

[GS04] Gupta, R. & Srivastava, M. “Carbon ion implantation on titanium for TiC formation using a dense plasma focus device”. *Plasma Sources Science and Technology* **13**.3 (2004), p. 371.

[Hab12a] Habibi, M. “Study of the electrode material and insulator length effect on high-energy X-rays emitted by a 4-kJ plasma focus device”. *Plasma physics reports* **38**.7 (2012), pp. 566–573.

[HA10] Habibi, M & Amrollahi, R. “Anisotropic investigation of hard X-ray emission with flat anode tips in APF plasma focus device”. *Journal of fusion energy* **29**.2 (2010), pp. 119–123.

[Hab10] Habibi, M et al. “Experimental study of hard X-ray emission with different anode tips in APF plasma focus device”. *Journal of fusion energy* **29**.1 (2010), pp. 49–54.

[Hab13] Habibi, M et al. “Study of Pyrex and quartz insulators contamination effect on the X-ray intensity in a 4-kJ plasma focus device”. *Plasma Physics Reports* **39**.12 (2013), pp. 999–1003.

[Hab12b] Habibi, M. “Influence of Pyrex Insulator Thickness and itâĂŹs Length on Hard X-Ray Intensity in APF Plasma Focus Device”. *Journal of fusion energy* **31**.2 (2012), pp. 130–133.

[Hay13] Hayati, M et al. “An optimized design of anode shape based on artificial neural network for achieving highest X-ray yield in plasma focus device”. *Journal of Fusion Energy* **32**.6 (2013), pp. 615–621.

[Hos11] Hosseinnejad, M. et al. “Preparation of titanium carbide thin film using plasma focus device”. *Journal of fusion energy* **30**.6 (2011), pp. 516–522.

[Hub09] Huba, J. *NRL Plasma Formulary 2009*. Tech. rep. DTIC Document, 2009.

[HL65] Huddlestone, R. H. & Leonard, S. L. “Plasma diagnostic techniques”. *Plasma Diagnostic Techniques*. Vol. 1. 1965.

[HZ07] Hussain, S & Zakaullah, M. “Study of plasma focus as a hard X-ray source for non-destructive testing”. *Modern Physics Letters B* **21**.24 (2007), pp. 1643–1650.

[Hus06] Hussain, S et al. “Comparative studies of X-ray emission from a plasma focus with different metal inserts at the anode tip”. *Physics Letters A* **349**.1 (2006), pp. 236–244.

[Hus10] Hussain, S et al. “Tailoring a plasma focus as hard x-ray source for imaging”. *Applied Physics Letters* **96**.3 (2010), p. 031501.

[Hus09] Hussain, S. et al. “Effect of anode shape on correlation of neutron emission with pinch energy for a 2.7 kJ Mather-type plasma focus device”. *Journal of Applied Physics* **106**.2 (2009).

[Hut87] Hutchinson, I. H. *Principles of plasma diagnostics*. Cambridge university press, 1987.

[Jak91] Jakubowski, L et al. “High energy electron beam emission characteristics of the plasma focus POSEIDON”. *Proc. Intern. Workshop on Physics of Alternative Magnetic Confinement Schemes, October*. 1991, pp. 15–24.

[Jak04] Jakubowski, L et al. “Temporal characteristics of electron beams from plasma-focus and their correlation with highly-ionized Ar-lines”. *Czechoslovak Journal of Physics* **54**.3 (2004), pp. C291–C297.

[Kal13] Kalaiselvi, S. et al. “Optimization of neon soft X-rays emission from 200 J fast miniature dense plasma focus device: A potential source for soft X-ray lithography”. *Physics letters A* **377**.18 (2013), pp. 1290–1296.

[Kal14a] Kalaiselvi, S. et al. “Influence of Kr doping on neon soft X-rays emission in fast miniature plasma focus device”. *Physics letters A* **378**.10 (2014), pp. 804–809.

[Kal14b] Kalaiselvi, S. et al. “Low-energy repetitive plasma focus based neon soft x-ray lithography source”. *SPIE Optical Engineering+ Applications*. 2014, 92070P–92070P.

[Kan14] Kanani, A et al. “Assessment of image quality in x-ray radiography imaging using a small plasma focus device”. *Radiation Physics and Chemistry* **101** (2014), pp. 59–65.

[Kan97] Kant, C. R. et al. “Thin carbon film deposition using energetic ions of a dense plasma focus”. *Physics Letters A* **226**.3 (1997), pp. 212–216.

[Kat88] Kato, Y. et al. “Plasma focus x-ray source for lithography”. *Journal of Vacuum Science & Technology B* **6**.1 (1988), pp. 195–198.

[Kha10] Khan, H. et al. “Effect of preionization on soft x-ray emission and plasma dynamics in a small plasma focus system”. *Journal of Applied Physics* **107**.7 (2010), pp. 073301–073301.

[Kha14] Khan, M. Z. et al. “Low-Energy Plasma Focus Device as an Electron Beam Source”. *The Scientific World Journal* **2014** (2014).

[Kli12] Klir, D et al. “Search for thermonuclear neutrons in a mega-ampere plasma focus”. *Plasma Physics and Controlled Fusion* **54**.1 (2012), p. 015001.

[Kne06] Knecht, S. et al. “Propulsion and power generation capabilities of a dense plasma focus (DPF) fusion system for future military aerospace vehicles”. *Space Technology and Applications International Forum - STAIF 2006*. Vol. 813. AIP Conference Proceedings. 2006, pp. 1232–1239.

[Kno08] Knoblauch, P et al. “Design, hard x-ray source characterization and applications of a plasma focus tailored for flash hard x-ray imaging”. *Physica Scripta* **2008**.T131 (2008), p. 014033.

[Koh05a] Koh, J. et al. “Optimization of the high pressure operation regime for enhanced neutron yield in a plasma focus device”. *Plasma Sources Science & Technology* **14**.1 (2005), pp. 12–18.

[Koh05b] Koh, J. et al. “Optimization of the high pressure operation regime for enhanced neutron yield in a plasma focus device”. *Plasma Sources Science and Technology* **14**.1 (2005), p. 12.

[Koo13] Koohestani, S. et al. “Study of the effect of pyrex and quartz insulators on X-ray intensity in a 4 kJ plasma focus device”. *The European Physical Journal D* **67**.6 (2013), pp. 1–6.

[Kri12] Krishnan, M. “The dense plasma focus: A versatile dense pinch for diverse applications”. *Plasma Science, IEEE Transactions on* **40**.12 (2012), pp. 3189–3221.

[Kub06] Kubes, P. et al. “Time of Neutron Production on Z Pinch and Plasma Focus Devices”. *AIP Conf. Proc.* **875**.1 (2006), pp. 15–18.

[Kub13] Kubes, P et al. “Correlation of x-ray emission with interferometry and neutron diagnostics at tungsten anode face and deuterium filling in plasma-focus discharge”. *Plasma Physics and Controlled Fusion* **55**.11 (2013), p. 115005.

[Kub09] Kubes, P. et al. “Determination of deuteron energy distribution from neutron diagnostics in a plasma-focus device”. *Plasma Science, IEEE Transactions on* **37**.1 (2009), pp. 83–87.

[Kub12a] Kubes, P. et al. “Energy Transformations in Column of Plasma-Focus Discharges With Megaampere Currents”. *IEEE T. Plasma Sci.* **40**.2, 2 (2012), 481–486.

[Kub12b] Kubes, P. et al. “Neutron production from a small modified plasma focus device”. *Plasma Science, IEEE Transactions on* **40**.12 (2012), pp. 3298–3302.

[LS96] Lee, P. & Serban, A. “Dimensions and lifetime of the plasma focus pinch”. *IEEE T. Plasma Sci.* **24**.3 (1996), pp. 1101–1105.

[Lee83] Lee, S. “A new theory for the fast compressional pinch”. *Proc. College Plasma Phys*. Trieste, Italy, 1983, pp. 967–977.

[Lee85a] Lee, S. “Plasma Focus Experiment”. *Proc. of the first Tropical College on Applied Physics: "Laser and Plasma Technology*. Kuala Lumpur, Malaysia, 1985, pp. 37–62.

[Lee85b] Lee, S. “Technology of the Plasma Focus”. *Proc. of the first Tropical College on Applied Physics: "Laser and Plasma Technology*. Kuala Lumpur, Malaysia, 1985, pp. 379–386.

[Lee09] Lee, S. “Neutron yield saturation in plasma focus: A fundamental cause”. *Applied Physics Letters* **95**.15 (2009), p. 151503.

[Lee14] Lee, S. “Plasma Focus Radiative Model: Review of the Lee Model Code”. *J. Fusion Energ.* **33**.4 (2014), pp. 319–335.

[LS08a] Lee, S. & Saw, S. H. “Neutron Scaling Laws from Numerical Experiments”. *Journal of Fusion Energy* **27**.4 (2008), pp. 292–295.

[LS08b] Lee, S. & Saw, S. H. “Pinch current limitation effect in plasma focus”. *Applied Physics Letters* **92**.2 (2008).

[LS13] Lee, S. & Saw, S. H. “Plasma focus ion beam fluence and flux- For various gases”. *Phys. Plasmas* **20**.6 (2013).

[LS12] Lee, S & Saw, S. “Plasma focus ion beam fluence and fluxâĂŤscaling with stored energy”. *Physics of Plasmas (1994-present)* **19**.11 (2012), p. 112703.

[Lee85c] Lee, S. et al. “Computation of Dynamics of Pulsed Plasmas”. *Proc. of the first Tropical College on Applied Physics: "Laser and Plasma Technology*. Kuala Lumpur, Malaysia, 1985, pp. 63–90.

[Lee08] Lee, S. et al. “Numerical experiments on plasma focus pinch current limitation”. *Plasma Physics and Controlled Fusion* **50**.6 (2008), p. 065012.

[LY14] Lerner, E. J. & Yousefi, H. R. “Runaway electrons as a source of impurity and reduced fusion yield in the dense plasma focus”. *Physics of Plasmas (1994-present)* **21**.10 (2014), p. 102706.

[Ler12] Lerner, E. J. et al. “Fusion reactions from> 150 keV ions in a dense plasma focus plasmoid”. *Physics of Plasmas (1994-present)* **19**.3 (2012), p. 032704.

[Lim11] Lim, L. et al. “Energetic Ion Beam Production by a Low-Pressure Plasma Focus Discharge”. *AIP Conference Proceedings-American Institute of Physics*. Vol. 1328. 1. 2011, p. 155.

[Lim14] Lim, L. et al. “Diagnostics of ion beam generated from a Mather type plasma focus device”. *American Institute of Physics Conference Series*. Vol. 1588. 2014, pp. 181–184.

[Lin14] Link, A et al. “Particle-in-cell modeling for MJ scale dense plasma focus with varied anode shape”. *9TH INTERNATIONAL CONFERENCE ON DENSE Z PINCHES*. Vol. 1639. 2014, pp. 23–26.

[M. 10] M. A. Abd Al-Halim. “Simulation of Plasma Focus Devices with Hemisphere Electrodes”. *J Fusion Energ* **29**.2 (2010), pp. 134–140.

[M. 07] M. M. Masoud and H. A. El-Gamal and H. A. El-Tayeb and A. A. Hassouba and M. A. Abd Al-Halim. “Magnetohydrodynamic simulation for plasma focus devices”. *Plasma Devices Oper* **15**.4 (2007), pp. 263–281.

[MT07] Mahabadi, T. D. & Tafreshi, M. A. “An investigation of the plasma behaviour in a Filippov type plasma focus device”. *Plasma Phys. Cont. F* **49**.9 (2007), p. 1447.

[MH13] Mahtab, M & Habibi, M. “Nitrogen soft and hard X-ray emissions using different shapes of anodes in a 4-kJ plasma focus device”. *Plasma Physics Reports* **39**.12 (2013), pp. 993–998.

[Mat64] Mather, J. W. “Investigation of the High-Energy Acceleration Mode in the Coaxial Gun”. *Physics of Fluids (1958-1988)* **7**.11 (1964), S28–S34.

[Mat65] Mather, J. W. “Formation of a High Density Deuterium Plasma Focus”. *Physics of Fluids (1958-1988)* **8**.2 (1965), pp. 366–377.

[Mat97] Mathuthu, M. et al. “The three-phase theory for plasma focus devices”. *IEEE T Plasma Sci* **25**.6 (1997), pp. 1382–1388.

[MS12] McCracken, G. & Stott, P. *Fusion: the Energy of the Universe*. Academic Press, 2012.

[MB93] Michette, A. G. & Buckley, C. J. *X-ray Science and Technology*. 1993.

[Mik04] Miklaszewski, R. “Neutron yield scaling for Plasma-Focus based on Gyrating Particle Model (GPM)”. *Czechoslovak Journal of Physics* **54**.3 (2004), pp. C198–C203.

[Mil13] Milanese, M et al. “Small plasma focus as neutron pulsed source for nuclides identification”. *Review of Scientific Instruments* **84**.10 (2013), p. 103501.

[Moh07a] Mohammadi, M. et al. “Neon soft x-ray emission studies from the UNU-ICTP plasma focus operated with longer than optimal anode length”. *Plasma Sources Science and Technology* **16**.4 (2007), p. 785.

[Moh09] Mohammadi, M. et al. “The effect of anode shape on neon soft X-ray emissions and current sheath configuration in plasma focus device”. *Journal of Physics D: Applied Physics* **42**.4 (2009), p. 045203.

[Moh11] Mohammadi, M. et al. “Neutron production with mixture of deuterium and krypton in Sahand Filippov type plasma focus facility”. *Physics Letters A* **375**.33 (2011), pp. 3002–3006.

[Moh13] Mohammadnejad, M et al. “Energy spectrum of argon ions emitted from Filippov type Sahand plasma focus”. *Review of Scientific Instruments* **84**.7 (2013), p. 073505.

[Moh07b] Mohanty, S. R. et al. “Effect of anode designs on ion emission characteristics of a plasma focus device”. *Japanese journal of applied physics* **46**.5R (2007), p. 3039.

[Mor15] Moreno, J. et al. “Neutron energy distribution and temporal correlations with hard x-ray emission from a hundreds of joules plasma focus device”. *Plasma Physics and Controlled Fusion* **57**.3 (2015), p. 035008.

[Mur11] Murtaza, G. et al. “Carburizing of zirconium using a low energy Mather type plasma focus”. *Surface and Coatings Technology* **205**.8 (2011), pp. 3012–3019.

[NM07] Neog, N. & Mohanty, S. “Study on electron beam emission from a low energy plasma focus device”. *Physics Letters A* **361**.4 (2007), pp. 377–381.

[Neo06] Neog, N. et al. “Anode length optimization in a modified plasma focus device for optimal x-ray yields”. *Journal of applied Physics* **99**.1 (2006), p. 013302.

[Nir11] Niranjan, R. et al. “Note: A portable pulsed neutron source based on the smallest sealed-type plasma focus device”. *Review of Scientific Instruments* **82**.2 (2011), p. 026104.

[Pat05] Patran, A et al. “Spectral study of the electron beam emitted from a 3 kJ plasma focus”. *Plasma Sources Science and Technology* **14**.3 (2005), p. 549.

[Pav14] Pavez, C. et al. “Potentiality of a table top plasma focus as X-ray source: Radiographic applications”. *Journal of Physics: Conference Series*. Vol. 511. 1. 2014, p. 012028.

[PM15] Pestehe, S. & Mohammadnejad, M. “Angular distribution of energetic argon ions emitted by a 90 kJ Filippov-type plasma focus”. *Physics of Plasmas (1994-present)* **22**.2 (2015), p. 022712.

[Pes14] Pestehe, S. et al. “Dynamic Faraday cup signal analysis and the measurement of energetic ions emitted by plasma focus”. *Physics of Plasmas (1994-present)* **21**.3 (2014), p. 033504.

[Pot78] Potter, D. “The formation of high-density z-pinches”. *Nucl Fusion* **18**.6 (1978), p. 813.

[Pot71] Potter, D. E. “Numerical Studies of the Plasma Focus”. *Phys Fluids* **14**.9 (1971), pp. 1911–1924.

[PM03] Pouzo, J. & Milanese, M. “Applications of the dense plasma focus to nuclear fusion and plasma astrophysics”. *IEEE Transactions on Plasma Science* **31**.6, 1 (2003), pp. 1237–1242.

[Qi98] Qi, N. et al. “Space and time resolved electron density and current measurements in a dense plasma focus Z-pinch”. *Plasma Science, IEEE Transactions on* **26**.4 (1998), pp. 1127–1137.

[Raf00] Rafique, M. S. “Compression dynamics and radiation emission from a deuterium plasma focus”. PhD thesis. 2000.

[Rag06] Ragheb, M. *Magnetic Confinement Fusion*. 2006.

[Ras04] Raspa, V et al. “Plasma focus as a powerful hard X-ray source for ultrafast imaging of moving metallic objects”. *Brazilian Journal of Physics* **34**.4B (2004), pp. 1696–1699.

[Ras07] Raspa, V et al. “Effective hard x-ray spectrum of a tabletop Mather-type plasma focus optimized for flash radiography of metallic objects”. *Journal of Applied Physics* **102**.12 (2007), p. 123303.

[Ras10] Raspa, V et al. “Plasma focus based flash hard X-ray source in the 100 keV region with reproducible spectrum”. *Physics Letters A* **374**.46 (2010), pp. 4675–4677.

[Raw01] Rawat, R. et al. “Room temperature deposition of titanium carbide thin films using dense plasma focus device”. *Surface and Coatings Technology* **138**.2 (2001), pp. 159–165.

[Raw04] Rawat, R. et al. “Soft X-ray imaging using a neon filled plasma focus X-ray source”. *Journal of fusion energy* **23**.1 (2004), pp. 49–53.

[Roo11a] Roomi, A et al. “Modified Reconstruction of Neutron Spectrum Emitted in Dense Plasma Focus Devices by MCNP Code and Monte-Carlo Method”. *Journal of Fusion Energy* **30**.1 (2011), pp. 78–82.

[Roo11b] Roomi, A et al. “The effect of applied voltage and operating pressure on emitted X-ray from nitrogen (N2) gas in APF plasma focus device”. *Journal of fusion energy* **30**.5 (2011), pp. 413–420.

[Rot86] Roth, J. R. *Introduction to fusion energy*. Classworks, 1986.

[S. 85] S. Lee. “Electromagnetic Shock Tube”. *Proc. of the first Tropical College on Applied Physics: "Laser and Plasma Technology*. Kuala Lumpur, Malaysia, 1985, pp. 3–36.

[Saw10] Saw, S. et al. “In situ determination of the static inductance and resistance of a plasma focus capacitor bank”. *Rev. Sci. Instrum.* **81**.5 (2010), p. 053505.

[Sch12a] Schmidt, A et al. “Fully kinetic simulations of dense plasma focus Z-pinch devices”. *Physical review letters* **109**.20 (2012), p. 205003.

[Sch14a] Schmidt, A et al. “Comparisons of dense-plasma-focus kinetic simulations with experimental measurements”. *Physical Review E* **89**.6 (2014), p. 061101.

[Sch14b] Schmidt, A et al. “Fully kinetic simulations of megajoule-scale dense plasma focus”. *Physics of Plasmas (1994-present)* **21**.10 (2014), p. 102703.

[Sch12b] Schmidt, H. et al. “Density distributions during the neutron-producing phase of the plasma focus POSEIDON”. *Plasma Science, IEEE Transactions on* **40**.12 (2012), pp. 3265–3272.

[Sch04] Scholz, M et al. “Correlation between pinch dynamics, neutron and X-ray emission from megajoule plasma focus device”. *Vacuum* **76**.2 (2004), pp. 361–364.

[Sea14] Sears, J et al. “Effect of Driver Impedance on Dense Plasma Focus Z-Pinch Neutron Yield and Beam Acceleration”. *APS Meeting Abstracts*. Vol. 1. 2014, p. 7013.

[Sen14] Seng, Y. et al. “Electromagnetic particle in cell modeling of the plasma focus: Current sheath formation and lift off”. *Physics of Plasmas (1994-present)* **21**.2 (2014), p. 023509.

[Sen15] Seng, Y. et al. “External circuit integration with electromagnetic particle in cell modeling of plasma focus devices”. *Physics of Plasmas (1994-present)* **22**.3 (2015), p. 033514.

[SL98] Serban, A. & Lee, S. “Experiments on speed-enhanced neutron yield from a small plasma focus”. *Journal of Plasma Physics* **60**.1 (1998), pp. 3–15.

[SL99] Serban, A. & Lee, S. “The effect of high axial sheath velocity on neutron yield in plasma focus”. *Fusion Technology* **35**.1 (1999), pp. 54–61.

[Sha03] Shafiq, M et al. “X-ray emission from a plasma focus with high-Z inserts at the anode tip”. *Plasma Sources Science and Technology* **12**.2 (2003), p. 199.

[Sha00] Shan, B. et al. “Improving Energy Efficiency of Plasma Focus”. *Sing. J. Phys* **16**.1 (2000), pp. 25–35.

[Sha06] Sharif, M et al. “X-ray emission scaling law from a plasma focus with different anode tip materials (Cu, Mo, and W)”. *Journal of applied physics* **100**.7 (2006), p. 073301.

[Sia05] Siahpoush, V. et al. “Adaptation of Sing Lee’s model to the Filippov type plasma focus geometry”. *Plasma Phys. Contr. F.* **47**.7 (2005), pp. 1065–1075.

[SSH10] Sing, L. & Sor Heoh, S. “Numerical Experiments Providing New Insights into Plasma Focus Fusion Devices”. *Energies* **3**.4 (2010), pp. 711 –737.

[Soh12] Sohrabi, M et al. “A novel method for observation by unaided eyes of nitrogen ion tracks and angular distribution in a plasma focus device using 50 Hz–HV electrochemically-etched polycarbonate detectors”. *Radiation Measurements* **47**.7 (2012), pp. 530–536.

[Soh14] Sohrabi, M et al. “Helium ion distributions in a 4 kJ plasma focus device by 1 mm-thick large-size polycarbonate detectors”. *Physics Letters A* **378**.48 (2014), pp. 3631–3637.

[Sot05] Soto, L. “New trends and future perspectives on plasma focus research”. *Plasma Physics and Controlled Fusion* **47**.5A (2005), A361.

[Spi62] Spitzer, L. *Physics of Fully Ionized Gases*. 1962.

[Ste04] Stepniewski, W. “MHD numerical modelling of the plasma focus phenomena”. *Vacuum* **76**.1 (2004), pp. 51–55.

[TS06] Tafreshi, M. & Saeedzadeh, E. “Studies of the hard X-ray emission from the Filippov type plasma focus device, Dena”. *Journal of Fusion Energy* **25**.3-4 (2006), pp. 207–211.

[Tak03] Takao, K et al. “Purity of nitrogen ion beams produced in a plasma focus”. *Plasma Sources Science and Technology* **12**.3 (2003), p. 407.

[TK09] Talaei, A. & Kiai, S. M. S. “Study the Influence of the Bank Energy on the Dynamical Pinch in Plasma Focus”. *J.Fusion Energ.* **28**.3 (2009), pp. 304–313.

[TK10] Talaei, A. & Kiai, S. S. “Influence of admixture gas on the enhancement of neutron production in plasma focus devices”. *Journal of fusion energy* **29**.5 (2010), pp. 427–435.

[TSK09] Talaei, A. & Sadat Kiai, S. “Investigation of the High Pressure Regimes Effects on the Neutron Production in Plasma Focus”. *J. Fusion Energ* **28**.3 (2009), pp. 235–239.

[Tal12] Talebitaher, A. “Coded aperture imaging of nuclear fusion in the plasma focus device”. PhD thesis. 2012.

[Tal13] Talukdar, N et al. “Study of X-ray emission from plasma focus device using vacuum photodiode”. *Nuclear Instruments and Methods in Physics Research Section A: Accelerators, Spectrometers, Detectors and Associated Equipment* **726** (2013), pp. 139–144.

[Tal14] Talukdar, N et al. “Study on neutron emission from 2.2 kJ plasma focus device”. *Physics of Plasmas (1994-present)* **21**.6 (2014), p. 062709.

[TSS14] Tarifeño-Saldivia, A. & Soto, L. “Effects of gas chamber geometry and gas flow on the neutron production in a fast plasma focus neutron source”. *Plasma Physics and Controlled Fusion* **56**.12 (2014), pp. 125013–125017.

[Vel12] Veloso, F. et al. “Correlations among neutron yield and dynamical discharge characteristics obtained from electrical signals in a 400 J plasma focus”. *Journal of fusion energy* **31**.1 (2012), pp. 30–37.

[Ver10a] Verma, R. “Construction and optimization of low energy (< 240J) miniature repetitive plasma focus neutron source”. PhD thesis. 2010.

[Ver08] Verma, R. et al. “Order of magnitude enhancement in neutron emission with deuterium-krypton admixture operation in miniature plasma focus device”. *Appl. Phys. Lett* **93**.10 (2008), p. 101501.

[Ver09a] Verma, R. et al. “Effect of cathode structure on neutron yield performance of a miniature plasma focus device”. *Physics letters A* **373**.30 (2009), pp. 2568–2571.

[Ver09b] Verma, R. et al. “Experimental study of neutron emission characteristics in a compact sub-kilojoule range miniature plasma focus device”. *Plasma Physics and Controlled Fusion* **51**.7 (2009), p. 075008.

[Ver10b] Verma, R. et al. “Miniature plasma focus device as a compact hard X-ray source for fast radiography applications”. *Plasma Science, IEEE Transactions on* **38**.4 (2010), pp. 652–657.

[Ver13] Verma, R. et al. “High performance high repetition rate miniature plasma focus device: Record time averaged neutron yield at 200 J with enhanced reproducibility”. *Journal of Fusion Energy* **32**.1 (2013), pp. 2–10.

[Vin14] Vinogradov, V. et al. “Development and study of a portable plasma focus neutron source”. *Plasma Physics Reports* **40**.2 (2014), pp. 146–159.

[Wel09] Welch, D. et al. “Fully kinetic particle-in-cell simulations of a deuterium gas puff Z pinch”. *Physical review letters* **103**.25 (2009), p. 255002.

[Wel11] Welch, D. et al. “Kinetic simulations of a deuterium-tritium Z pinch with> 1016 neutron yielda)”. *Physics of Plasmas (1994-present)* **18**.5 (2011), p. 056303.

[Yam82] Yamamoto, T. et al. “Measurement of Electron-and Ion Beam Energies and Currents in a Plasma Focus Discharge”. *Japanese Journal of Applied Physics* **21**.4R (1982), p. 659.

[Yap05] Yap, S. et al. “Observation of two phases of neutron emission in a low energy plasma focus”. *Japanese journal of applied physics* **44**.11R (2005), p. 8125.

[YM11] Yousefi, H. & Masugata, K. “Effect of Anode Impurity on the Neutron Production in a Dense Plasma Focus”. *Journal of fusion energy* **30**.6 (2011), pp. 490–493.

[You06a] Yousefi, H. et al. “Compression and neutron and ion beams emission mechanisms within a plasma focus device”. *Physics of Plasmas (1994-present)* **13**.11 (2006), p. 114506.

[You06b] Yousefi, H. et al. “Investigation of the neutron production mechanism in a 20 kJ plasma focus device”. *Journal of Fusion Energy* **25**.3-4 (2006), pp. 245–248.

[Zae10] Zaeem, A. A. “Effect of the Drive Parameter on the Differential Fusion Products in Plasma Focus Devices”. *IEEE Transactions on Plasma Science* **38**.8, 3 (2010), pp. 2069–2073.

[Zak96] Zakaullah, M. et al. “Neutron and X-ray emission studies in a low energy plasma focus”. *Physica Scripta* **53**.3 (1996), pp. 360–36.

[Zak97] Zakaullah, M. et al. “Influence of magnetic probe presence on current sheath dynamics in plasma focus operation”. *Fusion Engineering and Design* **36**.4 (1997), pp. 437–446.

[Zak03] Zakaullah, M et al. “Study of neutron emission in a low-energy plasma focus with β-source-assisted breakdown”. *Plasma Sources Science and Technology* **12**.3 (2003), p. 443.

[Zav13] Zavyalov, N. V. et al. “A source with a 10^{13} DT neutron yield on the basis of a spherical plasma focus chamber”. *Plasma Phys Rep* **39**.3 (2013), pp. 243–247.